UNIVERSITY OF COPENHAGEN
FACULTY OF SCIENCE

Ph.D. Thesis

Marcella Cabrera Berg

NANO-SCIENCE CENTRE
NIELS BHOR INSTITUTE

Dynamics of Liquids Confined in Porous Materials: A Quasi-Elastic Study

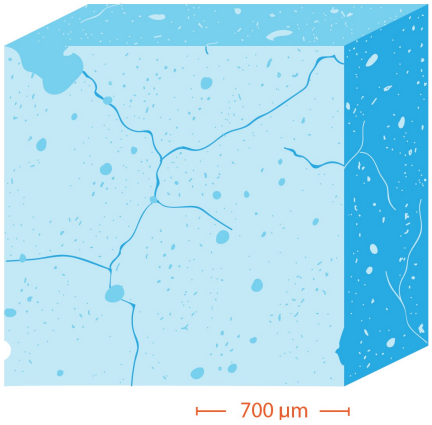

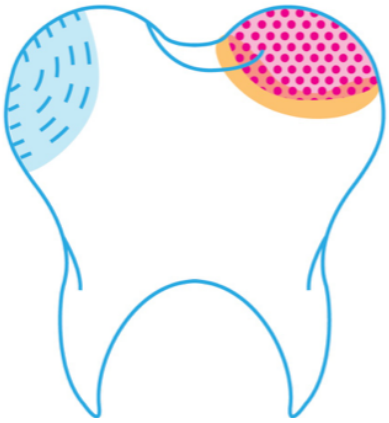

Supervisors:

Heloisa Nunes Bordallo[1] and Ana Raquel Benetti[2]

[1] Nano-Science Centre, The Niels Bohr Institute, University of Copenhagen
[2] Department of Odontology, Faculty of Health and Medical Sciences, University of Copenhagen

Dynamics of Liquids Confined in Porous Materials: A Quasi-Elastic Study

Submitted to:

The Graduate School of Science
Faculty of Science
Niels Bohr Institute
University of Copenhagen
Denmark

For the Ph.D. degree

By

Marcella Cabrera Berg
Nano-Science Centre
Niels Bohr Institute
University of Copenhagen
Universitetsparken 5
2100 Copenhagen
Denmark

November 2017

Acknowledgements

First and foremost, I would like to thank my two supervisors, Heloisa Nunes Bordallo and Ana Raquel Benetti for guiding me and providing counsel and support.

A big thanks goes to Mark T. F. Telling for the time he dedicated teaching me the basics of quasi-elastic neutron scattering in the beginning of my Ph.D. and to Jose Borreguero for his guidance and help during my exchange of environment at Oak Ridge National Laboratory.

The data collected for this work is largely from big scale facilities. I have been lucky to be part of a skilled team and would like to acknowledge all my colleagues involved, and in particular: Johan Jacobsen, Niels C. R. Momsen, Kim N. Dalby, Nikolaos Tsapatsaris, Henning O. Sørensen. A special thanks to Kim N. Dalby for preforming SEM measurements, Susan L. S. Stipp for useful scientific discussions and Suzy Mikkelsen for artistic improvement of illustrations. I would also like to thank my local contacts Mark T. F. Telling, Tilo Seydel, Dehong Yu and Luke Daemen.

I am especially grateful for my colleagues and friends: Éverton dos Santos, Murillo Longo Martins, José E. M. Pereira and Henrik Jacobsen for their scientific input and help during this work.

Finally I would like to thank the European Spallation Neutron Source, the Danish Agency for Science, Technology and Innovation through DANSCATT and the Niels Bohr Institute for financial support.

Abstract

Oral health is an integrated part of the public wellbeing, and does not only affect the quality of life, but also the healthcare system through related economic costs. Despite great global progress in oral health related issues, dental caries is still a major problem that affects both children and adults. Indeed, dental restorative work in industrialized countries is very costly, thus developing and improving restorative materials can beneficially impact the public health system. Among dental restorative materials glass ionomer cements (GIC) are of great interest, since they have the ability to bond to the tooth structure without the need for preconditioning the surface with an acid or unnecessary removal of tooth substance. Furthermore, fluoride is slowly released during setting adding to the anticariogenic benefits of the material. GIC's poor mechanical strength is however a disadvantage, and improved knowledge on this subject can bring potential development. One possibility is to advance our understanding of the dynamics of the aqueous solution used to prepare the GIC.

Under these lines, in this work I have combined neutron spectroscopy and calorimetric analysis to understand the nanoscale mobility of the hydrogen atoms, mostly from water, present in conventional GIC. Water plays a big part in the setting process in GIC. It is the reaction medium in which the cations leach to crosslink. Furthermore, water also hydrates the siliceous hydrogel and the metal polyacrylate salts. In matured GIC, water occupies coordination sites around cations in a hydration shell of the cation-polyacrylate, hydration regions around the polymer chain or still remains unbound in its bulk state. Neutron spectroscopy was chosen since the high incoherent scattering cross section of the hydrogen atom makes this technique ideal for assessing the dynamics of water in the material. Water is furthermore also easily detected by thermogravimetric analysis coupled to Fourier transform infrared spectroscopy and differential scanning calorimetric methods, which were also employed in this thesis. However understanding water dynamics in such complex hierarchical structure, where different motions occur in a broad range of time scales and simultaneously, can be difficult. So in this Ph.D. thesis, the experimental data was combined with preliminary classical molecular dynamics simulations (MD), aiming to investigate the different nanoscale water dynamics in the GIC. This unique approach opens new possibilities to better explore all the information contained in the neutron spectroscopy data.

Selected materials were investigated by first understanding the molecular motions of the different aqueous polyacrylic acid solutions (PAA) that are used in preparing the cements. These results are reported in Paper 1 and Paper 2. These findings were afterwards superimposed to the GICs themselves, in order to separate distinct molecular motions. This approach shows that the structure of the PAA solutions influences the overall properties of the GIC. The investigation of the dynamics of the confined liquid, the main body of this thesis, is reported in Paper 2. The results

show that water is confined differently in the polymer chain depending on the GIC. Two sub projects involving GIC that are not yet in a manuscript form are also briefly described in Chapter 3. These results further confirm that how the water is confined in the polymer chain determines its behavior in the GIC and to a certain extent controls hydrogen binding to the GIC structure. Therefore, the knowledge acquired during this Ph.D. thesis contributes to the understanding of the nature of the hydration in the GIC and can be applied towards the development and improvement of dental restorative materials.

Furthermore, two manuscripts regarding water and protein dynamics in confinement probed by quasi-elastic neutron scattering are also included in the thesis, Paper 3 and Paper 4. In Paper 3 we investigated why two chalk samples display vastly different water uptake, despite the fact that they are known to have similar pore volumes. In Paper 4 we investigated the dynamics of encapsulated Hepatitis B surface antigen in mesoporous silica SBA-15. My knowledge of liquids in confinement was extended by the analysis of the neutron data on these new and challenging systems.

Resume

Odontologi er en integreret del af den almene velvære, og påvirker både livskvaliteten hos befolkningen såvel som sundhedsvæsenet via relaterede omkostninger. På trods af de globale fremskridt inden for tandsundhed, er caries stadigvæk et stort problem, der påvirker børn så vel som voksne. Derfor er forskning i tandfyldnings materialer stadigvæk vigtig, hvor i særdeleshed materialet glasionomercementer (GIC) er interessant, da de binder til tandstrukturen og frigiver anticariogenisk fluor imens det herder. GIC har dog den ulempe at materialet har dårlig mekaniske styrke, hvilket mere viden potentielt kan afklare. En mulighed for at udvikle materialet er, at fremme forståelsen af dynamikken i den vandige opløsning, der anvendes i præparationen of GIC. Jeg vil ligeledes forstå hvordan denne dynamik ændres, når den vandige opløsning inkorporeres i materialet.

Med henblik på forståelse af dynamik i GIC, har jeg kombineret neutronspektroskopi og kalorimetrisk analyse. Mere specifikt vil jeg forstå hydrogenatomernes mobilitet på nanoskala, der hovedsagelig kommer fra vand. Neutronspektroskopi blev anvendt i dette studie, på grund af hydrogenatomets høje inkohærente spredningstværsnit, der gør teknikken ideel til at måle dynamik i vandholdige materialer. I GICs komplekse hierarkiske struktur kan forståelsen af vanddynamikken dog være vanskelig. Derfor har jeg i denne Ph.D. afhandling kombineret de eksperimentelle data fra neutronspektroskopi med indledende klassiske molekylær dynamik simuleringer (MD). Denne unikke tilgang til neutronspektroskopi, giver nye muligheder for bedre forståelse og udforskning af data. Den tilegnet viden under denne Ph.D. afhandling bidrager til forståelsen af hydrering i GIC, og kan anvendes til at udvikle og forbedre tandfyldnings materialet.

Curriculum Vitae

Marcella Cabrera Berg

Matthæusgade 48B, 112 | 1666 København V, Denmark | +45 28 55 83 88 | marcellac.berg@gmail.com | 20 Jan 1987

EDUCATION

RESEARCH ASSISTANT IN PHYSICS | UNIVERSITY OF COPENHAGEN|

COPENHAGEN, DENMARK | 2017- |

Working at the X-ray and Neutron Scattering group at the Niels Bohr Institute under the Interreg Cross Border Science and Society EU-program

PhD STUDENT IN PHYSICS | UNIVERSITY OF COPENHAGEN | COPENHAGEN, DENMARK | 2014-2017|

Working at the X-ray and Neutron Scattering group at the Niels Bohr Institute, with specialization in use neutron spectroscopy and Molecular Dynamics

DATA MANAGEMENT AND VISUALIZATION | OAK RIDGE NATIONAL LABORATORY | TENNESSEE, USA |2017 |

Working on molecular dynamics simulations of aqueous polyacrylic acid solutions.

CAND. SCIENT. IN PHYSICS | UNIVERSITY OF COPENHAGEN | COPENHAGEN, DENMARK |2011-2014|

Master Thesis: Theoretical studies of the magnetic and superconducting properties of super-oxygenated LSCO.

PHYSICS | UNIVERSITY OF SÃO PAULO | SÃO CARLOS - SÃO PAULO, BRAZIL |2012-2013|

BSc IN PHYSICS | UNIVERSITY OF COPENHAGEN | COPENHAGEN, DENMARK |2007-2011|

Final project: Perturbation theory in Einstein gravitation.

CONFERENCES & SEMINARS

Participant at:

Atomistic Modeling for Neutron Scattering, Oak Ridge, USA, 7-9 June, 2017, organized by Oak Ridge National Laboratory.
Woman in Science, Copenhagen, Denmark, 2 December 2016, organized by the University of

Copenhagen
Scientific writing, Copenhagen, Denmark, 14 November - 12 December, 2016, organized by the University of Copenhagen
Responsible Conduct of Research, Copenhagen, Denmark, 22 November, 2016, organized by the University of Copenhagen.
PhD Day, Copenhagen, Denmark, 18 November, 2016, organized by the University of Copenhagen
Computer programing with Mantid, Dicot, 2015, organized by the Rutherford Appleton Laboratory.
Oxford School 2015, Oxford, UK, 16-19 February, 2015, organized by the Rutherford Appleton Laboratory and Oxford University.
Geilo School 2015, Geilo, Norway, 16-26 March, 2015, organized by the Institute for Energy Technology.
Fourth Annual Niels Bohr International Academy Workshop - School on ESS Science, 10-14 November, 2014, Denmark.
MDANSE School 2014: Molecular Dynamics to Analyse Neutron Scattering. Grenoble, France, 9-10 May 2014, organized by ILL

Presented talks at**:**

Brazil-MRS (2016): Quasi-elastic and inelastic neutron scattering: revealing confined liquid dynamics in dental cements, Campinas, Brazil.
International Conference on Quasielastic Neutron Scattering QENS (2016**):** Quasi-elastic neutron scattering: liquid dynamics in dental cements, Potsdam, Germany.
13th Nordic workshop on Scattering from Soft Matter (2016): Quasi-elastic neutron scattering and dental cements, Uppsala Sweden.
European Conference on Neutron Scattering (2015): Quasi-elastic neutron scattering on dental cement: can we do better?, Zaragoza, Spain.
ESS Science day (2015): Quasi-elastic neutron scattering on dental cement, Lund, Sweden.
ESS workshop for PhD students (2015): Neutron scattering, a powerful tool to study water in confinement, Lund, Sweden.
Denmark - Brazil Cooperation on Materials and Energy (2014): Academic studies in Brazil and Denmark, Campinas, Brazil.

Presented Poster at**:**

International Conference on Neutron Scattering (2017): Understanding the dynamics of aqueous solutions in dental cements, Daejeon, Republic of Korea.
50 Years of Neutron Backscattering Spectroscopy (2016): Water dynamics in glass ionomer cements, Munich, Germany.
Geilo School (2015): Using neutron scattering to study water dynamics in different confined geometries, Geilo, Norway.
Fourth Annual Niels Bohr International Academy Workshop-School on ESS Science (2014): Introducing intermediate oxygen in cuprates, Copenhagen, Denmark.

TEACHING

Teaching Assistant:

Responsible for practical lessons and correcting assignments. Approximate 150 of hours dedicated per year.

Thermodynamics (2017)
Thermodynamics (2016)
PhD International Workshop-School NBIA (2015)
Classical Mechanics (2015)

LANGUAGE AND COMPUTER SKILLS

Language skills:

Danish (native)
English (professional)
Portuguese (professional)
Norwegian & Swedish (good understanding)

Programming skills:

DAVE (excellent understanding)
LAMP (excellent understanding)
Mantid (good understanding)
LAMMPS (good understanding)
Material Studio (good understanding)
Mathematica (good understanding)
MatLab (good understanding)
Maple (good understanding)
McStas (good understanding)

PUBLICATIONS

- Berg, M. C.; Jacobsen, J.; Momsen, N. C. R.; Benetti, A. R.; Telling, M. T. F.; Seydel, T.; Bordallo, H. N. Water Dynamics in Glass Ionomer Cements. *Eur. Phys. J. Spec. Top.* **2016**, *225* (4), 773–777.

- Berg, M. C.; Dalby, K. N.; Tsapatsaris N.; Okhrimenko, D. V.; Sørensen, H. O.; Jha, D.; Embs, J. P.; Stipp, S. L. S.; Bordallo, H. N. Water Mobility in Chalk: A Neutron Scattering Study. J. Phys. Chem. C. **2017**, *121* (26), 14088-14095.

- Berg, M. C.; Benetti, A. R.; Telling, M. T. F.; Seydel, T.; Yu, D.; Daemen, L.; Bordallo, H. N. Nanoscale Mobility of Aqueous Polyacrylic Acid in Dental Restorative Cements. *Under Review*

- Rasmussen, M. K.; Pereira, J. E. M.; Berg, M.C.; Iles N. G; Jalarvo N. H; Botosso V. F; Sant'Anna, O. A; Fantini, M. C. A.; Bordallo, H. N. Dynamics of encapsulated Hepatitis B surface Antigen: A combined neutron spectroscopy and study. *Under Review*

Publications and Author Contributions

In this thesis 4 manuscripts are presented. Paper 1 and Paper 2 will constitute the main body of the thesis, while Paper 3 and Paper 4 are additional work regarding the dynamics of liquids in confinement.

Main body of the thesis:

1. Berg, M. C.; Jacobsen, J.; Momsen, N. C. R.; Benetti, A. R.; Telling, M. T. F.; Seydel, T.; Bordallo, H. N. Water Dynamics in Glass Ionomer Cements. *Eur. Phys. J. Spec. Top.* **2016**, *225* (4), 773–777.

A. R. Benetti and H. N. Bordallo conceived the project. M. C. Berg, A. R. Benetti and H. N. Bordallo wrote the manuscript. J. Jacobsen, N. C. R. Momsen, A. R. Benetti, M. T. F Telling, T. Seydel and H. N. Bordallo performed the neutron experiments M. C. Berg performed the thermoanalysis experiments, analyzed and interpreted the data as well as made the final figures. All authors participated in reviewing the manuscript.

2. Berg, M. C.; Benetti, A. R.; Telling, M. T. F.; Seydel, T.; Yu, D.; Daemen, L.; Bordallo, H. N. Nanoscale Mobility of Aqueous Polyacrylic Acid in Dental Restorative Cements. *Under Review*

M. C. Berg, A. R. Benetti and H.N. Bordallo conceived the project and wrote the manuscript. All authors contributed to the neutron experiments. M. C. Berg prepared the samples and, in particular, performed the neutron experiments using PELICAN and IN16B, analyzed and interpreted the data as well as made the final figures. All authors participated in reviewing the manuscript. M.C. Berg administrated the submission and is handling the review process.

Additional work on water and protein dynamics in confinement:

3. Berg, M. C.; Dalby, K. N.; Tsapatsaris N.; Okhrimenko, D. V.; Sørensen, H. O.; Jha, D.; Embs, J. P.; Stipp, S. L. S.; Bordallo, H. N. Water Mobility in Chalk: A Quasielastic Neutron Scattering Study. J. Phys. Chem. C. **2017**, *121* (26), 14088-14095.

N. Tsapatsaris and H. N. Bordallo conceived the neutron experiments with input from K. N. Dalby, H. O. Sørensen and S. L. S. Stipp. K. N. Dalby, N. Tsapatsaris, H. O. Sørensen, D. Jha and J. P. Embs performed the neutron experiments. D .V. Okhrimenko collected the BET data. M. C. Berg analyzed the neutron spectroscopy data and made the final figures. M. C. Berg, K. N. Dalby and H.N. Bordallo interpreted the data and wrote the manuscript with input from D. V. Okhrimenko, H. O. Sørensen and S. L. S. Stipp. All authors participated in reviewing the manuscript.

4. Rasmussen, M. K.; Pereira, J. E. M.; Berg, M.C.; Iles N. G; Jalarvo N. H; Botosso V. F; Sant'Anna, O. A; Fantini, M. C. A.; Bordallo, N. H. Dynamics of encapsulated Hepatitis B surface Antigen: A combined neutron spectroscopy and thermo-analysis study. *Under Review*

M. K. Rasmussen and H. N. Bordallo conceived the project, planned the neutron experiments and wrote the manuscript. M. K. Rasmussen, J. E. Pereira, G. N. Iles and N. Jalarvo performed the experiments. M. C. Berg analyzed and interpreted the quasi-elastic neutron data and made the final figures related to this analysis. All authors participated in reviewing the manuscript.

Contents

Chapter 1 Introduction

1.1 Motivation

Oral health does not only affect the quality of life for both children and adults, but also the healthcare system through related economic costs. Despite great global progress in oral health related issues, dental caries is still a major problem and one of the most costly. Thus developing and improving restorative materials is urgent. Controlling the hydration process during the preparation of dental cements would be of great interest in developing a better material. A sensible choice is the Glass Ionomer Cements (GIC) as it possesses very interesting biocompatible properties[1–4]. The properties of GIC are largely determind by liquid mobility, and thus we must have a better understanding of how the liquid mobility evolves during the cement setting process under confinement in the material's pore structure.

Similar to all GIC are the content of glass-silicate-aluminum base powder, which is mixed with an aqueous polyacrylic acid solution (PAA), so that the cement hardens through an acid base reaction. The GIC used for dental restorations can either be mixed by hand or mechanically, the latter being done by packing pre-dosed powder and liquid in capsules. One of the positive aspects of GIC, is the release of fluoride while setting in the tooth[2,4–7]. However the strength of these GIC could be improved[2,6]. Under these lines, this study focused on the hydration process and how this knowledge can be used for further material development. This was achieved by a better understanding of how the hydrogen bond network develops during setting and maturation, as well as how the dynamics of different solutions used in preparing GIC behaves under confinement.

In this thesis, different restorative GIC were investigated. These materials were chosen based on their physical and mechanical properties that are to a certain extent controlled by the glass particle size and the aqueous PAA composition[1–3,5,6,8]. Here the aim was to correlate the different setting processes of the materials with the diffusivity of the liquid used to mix the GIC. By combining quasi-elastic neutron scattering (QENS) with inelastic neutron scattering (INS), we achieved insight on the dynamics of the free and confined liquids and how their dynamics is modified as the density of the material changes with setting. Furthermore, from the thermo analysis invaluable information on the different hydrogen bond networks were obtained. As the hydrogen mobility in PAA occurs over a broad time range, to cover full dynamical range of these processes the neutron spectroscopy data was collected on several different spectrometers. These results form the main body of this thesis and help in further understanding how the overall dynamical properties of the confined liquid in the GIC influence the material properties. These results also give insight on how chemical modifications to the liquid, and consequently to the GIC, can influence the properties of dental restorative cements. Understanding the hydration process in these materials certainly provides unique information for future development.

Defining the proton dynamics in such complex hierarchical structures, where important motions related to the different states of the hydrogen atoms evolve in a confined porous structure, can be difficult only by the means of experimental techniques. So in this study, the QENS data was also combined with preliminary molecular dynamics simulations, aiming to investigate the structure factor, $S(\mathbf{Q},\omega)$, of the free and confined aqueous PAA solution. Future studies centered on the confinement of the aqueous solution of PAA in the GIC are now envisaged. This unique approach opens new possibilities to better explore all the information contained in INS and QENS data. This idea is discussed as perspectives for this Ph.D. work.

1.2 Glass ionomer cements: History and Materials Properties

Dental restorative glass ionomer cements (GIC) were first introduced and patented in the late 1960s, and then further developed by Wilson and Kent in the early 1970s[9]. Developments of GIC were mostly based on the modification of pre-existing silicate cements[4], which back then had been the best available restorative material for anterior teeth[10]. The most important alteration was the introduction of the polyacrylic acid aqueous solution (PAA). By adding PAA, the cement now consisted of a powder-liquid system consisting of aluminum-silicate-glass and polycarboxylic acid.

GIC have since then been of great interest, as they have the ability to bond to the tooth structure without the need for preconditioning the surface with an acid. Additionally, they do not require unnecessary removal of tooth substance and have a thermal expansion coefficient similar to the hard dental tissues. Furthermore, the incorporation of fluoride[11], which is slowly released over weeks during setting, added a new depth to its anticariogenic benefits. The potential for GIC was recognized and the material was industrialized for commercial use either as a luting agent and liner or for dental restoration in the early 1970s[4,12].

In the 1990s, the mechanical properties and strength of the conventional GIC was improved with the incorporation of a light polymerizable resin component. The new resin-modified glass ionomer cements (RMGIC) have a longer working time and an improved aesthetics. Furthermore, they also have a quicker initial setting and enhanced initial strength when compared to conventional GIC[13–15]. However, the presence of the resin component makes the setting reaction more complex, since not only the acid-base reaction between the glass particles and the polyacid solution occurs, but also a photo initiated polymerization reaction of the resin monomers takes place. The initial setting in the RMGIC is caused by the polymer chain propagation resulting from the polymerization reaction[13] and, therefore a significant improvement in the strength during the critical first hours of setting can be achieved[14]. During the initial setting process of the RMGIC, the acid-base and polymerization reactions compete, inhibiting each other[16–18]. Consequently a suitable polymerization of the resin component is fundamental to avoid a weaker material.

Both conventional GIC and RMGIC continue to be of great interest to the dental community; however further improvement in material strength is desirable if the GIC are to be used as long-term dental fillings in high load bearing areas. In contrast to the dynamical characteristics of the confined liquid within the material, other subjects such as structure, mechanical properties and setting have been widely studied[2,4,7,19–22]. To elaborate on this missing knowledge, this thesis focuses on the proton dynamics of the GIC. This means the study of the liquid in several forms of

confinement, for which the combination of neutron spectroscopy and thermal analysis, supported by molecular dynamics calculations, was deemed the best approach.

In contrast to other silica glasses, the glass used in GIC is soluble in acid, which makes the setting reaction possible. The glass powders' ability to be dissolved in the acid comes from the structure of the glass, which has fused silica with incorporated negatively charged regions from the aluminum, that partially have replaced the silica (see Figure 1:1).

The main components in the powder are silicon dioxide (SiO_2), alumina (Al_2O_3) and calcium (or strontium) fluoride (Ca/SrF_2), fused by heating up to 1100-1500 °C and then cooled abruptly. The glass is subsequently ground into particles ranging from nm to 15-50 μm in size. The composition of the glass powder controls the setting rate of the cement, largely determined by the silicate-aluminum ratio (Al_2O_3:SiO_2)[23,24]. The negatively charged regions are attacked by the acid's positive hydrogen ions, and therefore the ratio of Al_2O_3:SiO_2 controls both the solubility and the time it takes to dissolve the glass. Furthermore, an increase in Al_2O_3 concentration results in increased strength[10]. On the other hand, the particle size plays an important role in the setting time, where the smaller the particle (i.e. bigger the specific surface area) the shorter the setting time[10].

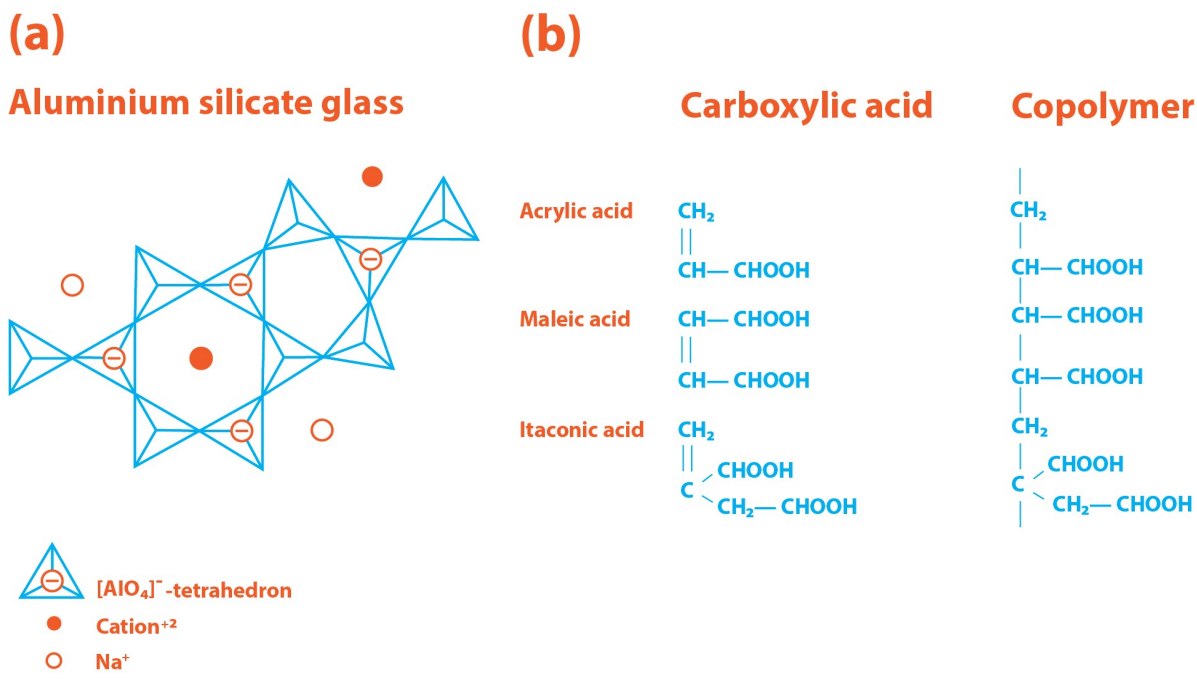

Figure 1:1 (a) Structure of the aluminium silica glass with an electrical charged grid. The glass has incorporated negatively charged regions from the aluminium that partially replace the silica, allowing the glass to react with the acidic aqueous solution. The negatively charged regions in the glass are attacked by the positive hydrogen ions in the polyacrylic acid solution. (b) Structure of the most common carboxylic acids (left) and its corresponding co-polymeric structures (right) used in GIC preparation. Adapted from [10].

The liquid consists of a high molecular link between polymers (typically an unsaturated carboxylic acid) and electrolytes in an aqueous solution[10]. Over time, in a pure single type polymer PAA aqueous solution, the liquid becomes gel-like as a result of the formation of hydrogen bonds. This can be upheld by adding a co-polymer of acrylic, itaconic and maleic acid to the solution (see Figure 1:1), for example. However, adding the co-polymer makes the GIC more vulnerable to acid attacks and inhibits the binding to the enamel and dentin[10,14,20]. Nevertheless, a greater number of carboxylic acid groups in the copolymer produce a matrix with more crosslinking, which makes the GIC stronger. Furthermore, the molecular weight and the polymer concentration also influence the properties of the GIC[5] . Increasing the molecular weight in the polymer concentration causes a faster reaction and increase in strength. However, it also makes the liquid more viscous and the cement more difficult to mix.

The setting reaction starts as soon as the powder comes in contact with the liquid, and goes through the following five stages[10]:

i) Degradation of the glass powder and the release of the metal ions.

ii) Migration of the released metal ions into the aqueous segment in the GIC.

iii) Formation of the silica gel.

iv) Hardening of the cement.

v) Maturation of the cement

In the first two stages, the relatively weak aqueous PAA dissolves the finely powdered glass. The acid attacks the surface layer of the glass resulting in the release of cations into the aqueous segment (see Figure 1:2). As the reaction progresses, the PAA converts into polysalts, and as a result of the increased concentration of ions, the viscosity and the pH increase.

In stages (iii) and (iv), the cement paste reaches a specific pH value and the precipitation of the polysalt begins. The released cations form salt bridges between the polyacid chains, resulting in the formation of silica hydrogel at the interface between the glass particle and the cement matrix (see Figure 1:2). The subsequent hardening process is dominated by a much slower formation of aluminum polysalts (see Figure 1:3), which is the governing phase of the GIC matrix. The glass powder core remains intact, acting as filler in the cement network[2].

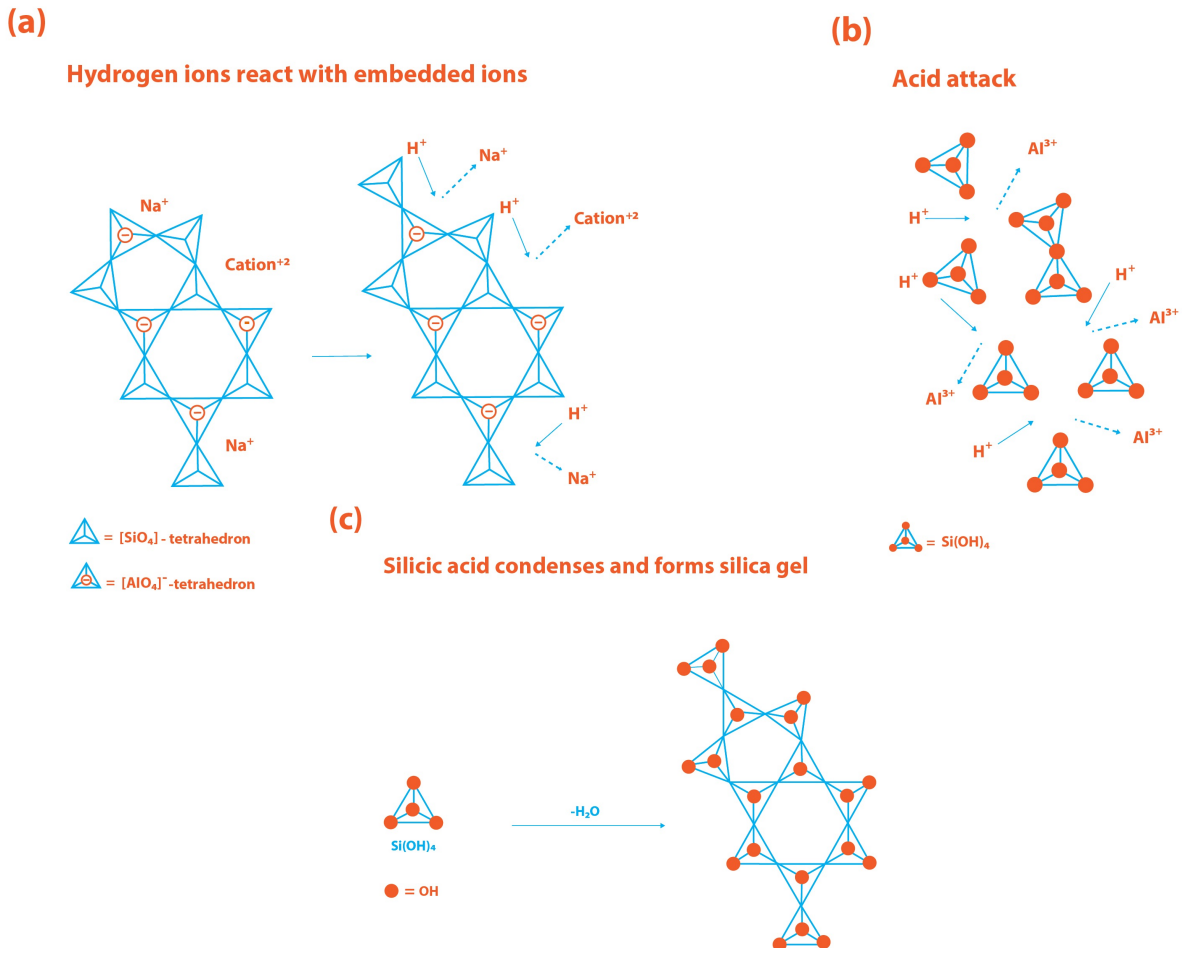

Figure 1:2 Degradation of the base aluminum (-cation) silicate glass powder caused by the acid-base reaction. (a) The hydrogen ions attack the interstitially embedded calcium and sodium ions. (b) The hydrogen ions attack the charged aluminum silicate glass, thereafter the crystalline structure decomposes and the aluminum ions are released. (c) The created silica acid condensates and forms the silica gel. The figure describes the first 3 stages in the setting process. Adapted from [10].

In the last stage of the setting process, the cement matures. This stage can last up to a year, where the cement is still liable to change, i.e. forming hydrogen bond and crosslinking. Therefore, the strength may increase and the cement may become harder, see Figure 1:4. In this study the investigated GIC were within the last stage of the setting, and the studied cement samples were between 5 and 28 days old.

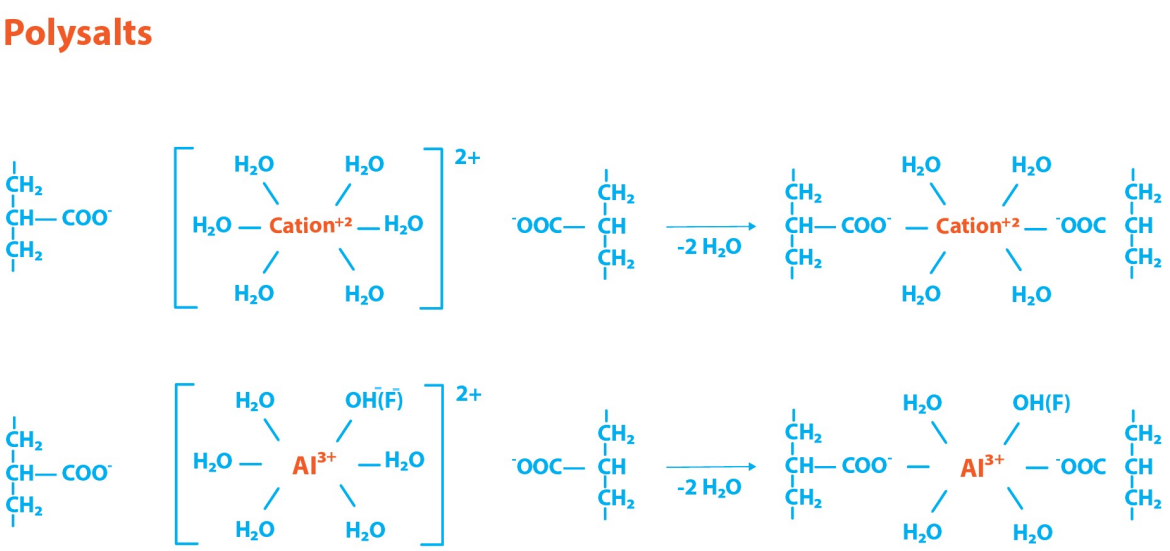

Figure 1:3 Formation of the polysalts, also called polyelectrolytes. The top figure depicts the formation of calcium (cation) polysalts mostly present in stage ii of the setting, while the bottom figure shows the slower formation of aluminum salt mostly present in stages iii and iv of the setting. Adapted from [10].

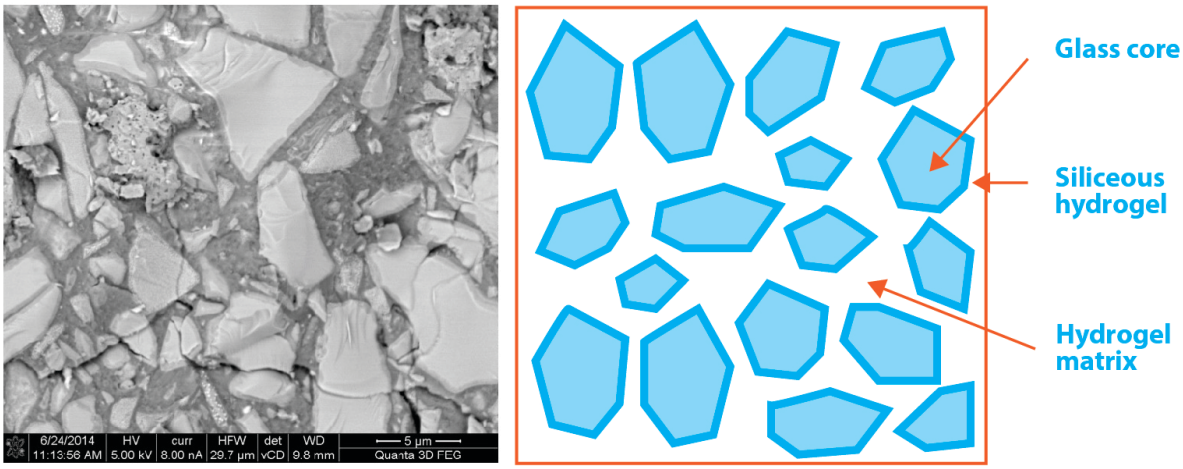

Figure 1:4 (left) Scanning electron microscopy (SEM) picture of one of the studied GIC after 28 days. (right) Schematic of the GIC in the mature cement, the filler are bound together by a hydrogel of cations and aluminum polyacrylates, containing fluoride. The filler particles contain a glass core surrounded by the siliceous hydrogel.

1.3 Probing Water in Glass Ionomer Cements

Water is essential to the setting process of the cement. In the first steps of the setting, water acts as the reaction medium in which the leached cations crosslink with the liquid, forming the polyacrylate matrix. The conformation of the polyelectrolyte chain and its flexibility will in turn govern the degree of crosslinking in the polyacrylate matrix, thus influencing the cement properties. Furthermore, water also hydrates the siliceous hydrogel and the metal polyacrylate salts, becoming an essential part of the cement and being found in various forms within the cement structure[23].

If water is lost from the cement by desiccation in the beginning of the setting, the reaction will stop or be retarded. On the other hand, in the first 3 to 6 minutes of the cement's hydration, the early contact with water can be damaging, thus the surface of the restoration must be protected[5,25]. During maturation and in the completely set cement, water can then occupy coordination sites around cations in a hydration shell of the cation-polyacrylate[26] or hydration regions around the polymer chain, generally classified as tightly bound water. Tightly bound water cannot be easily removed. Water can also remain unbound, commonly referred to as loosely bound water, which is liable to change, unless the cement is at about 80% relative humidity. The unbound water is believed to cause the GIC to crack over time[27], as it will easily diffuse through the material. With ageing, it is also observed that in some GIC the ratio of tightly bound to loosely bound water increases, as the loosely bound water forms new chemical bonds and becomes part of the cement matrix. In addition, with ageing, it is observed in some cement samples, that the pore structure changes[28] and that the compressive strength of the GIC increases.

In this investigation, neutron spectroscopy was appropriate since the neutron is not only able to penetrate deeply into the material without perturbing its composition, but also the high incoherent scattering cross section of the hydrogen atom makes the technique ideal for assessing the dynamics of hydrogenous materials[29–34]. Water is furthermore also easily detected by the thermogravimetric analysis coupled to Fourier transform infrared spectroscopy (TGA/FTIR)[35,36] and differential scanning calorimetry (DSC)[17,37,38] methods employed in this thesis.

Chapter 2 Methods and Theory

2.1 Sample preparation

In this study 6 different GIC were investigated from 3 different companies. From “Voco GmbH, Germany” we investigated: Encapsuled Poly Ionofil Molar AC (hereafter named Poly), Aqua Ionofil Plus (hereafter named Aqua), and Ionloux (hereafter named Hema). From “GC America Inc.”: Encapsulated Equia Forte Fil (hereafter named Equia) and encapsuled Fuji IX GP (hereafter named Fuji). From “3M, United States” we investigated encapsuled Ketac Molar Aplicap (hereafter named Ketac). The composition of the GIC used in this study as stated by the manufacturers is given in Table 2:1

Poly, Fuji, Ketac and Equia cements were prepared by mixing the powders with their respective liquids in accordance with the manufacturer's recommendation, using a mechanical agitator (CapMix Capsule Mixing Device, 3M ESPE AG, Germany) for 10 seconds, or for 10 seconds mixing and 5 seconds centrifugation (RotoMix Capsule Mixing Device, 3M ESPE AG, Germany). Aqua and Hema cements were hand mixed by using a powder-to-liquid ratio of 5.6:1 and 3.2:1 by weight, respectively. Furthermore, Hema was light activated according to the manufacture’s recommendation using a lamp (bluephase, Ivoclar Vivadent) emitting 950 mW/cm^2.

The GIC samples were prepared for two purposes: firstly, for the analysis of the proton dynamics using neutron spectroscopy, and secondly, for calorimetric examination and characterization. Preparation was carried out at room temperature (approximately 20 ºC). For the neutron experiments, approximately 1 g (equivalent of 3 capsules) of sample was mixed and uniformly distributed as a thin film inside a flat sample holder, while for the calorimetric examination, although the amount of sample was the same, the samples were distributed in separate rows (see Figure 2:1) to be used in triplicates. Subsequently, immediately after mixing, the samples were wrapped in aluminum foil and placed inside a flat aluminum sample holder sealed with indium wire (see Figure 2:1). All samples were stored for 7 or 28 days at 37 ºC, corresponding to body temperature. In the case of the hydration measurements of the cements, the sample holders were placed in the beam approximately 15 minutes after the start of the mixture and measured for 24 hours. Both the liquid and powder samples were not in contact with air before the measurements.

Poly, Aqua and Hema and their respective liquids and powders were studied in Paper 1 and Paper 2. The Fuji, Ketac and Equia samples and their respective liquids and powders were investigated, but not yet fully analyzed, although mentioned in Chapter 3. Therefore the main body of this thesis consists of a discussion on the GIC Aqua and Poly samples and the RMGIC Hema.

Table 2:1 Composition and contribution in percentage from the investigated samples for the liquid and powder components, as reported by the manufacturers MSDS. All GIC contain aluminum silicate glass powder and a polyacrylic acid (PAA) in an aqueous solution. The composition of the glass powder and the polyacid to glass-powder ratio varies among the samples. The samples Poly, Aqua and Hema constitute the main body of the thesis and are discussed in Paper 1 and Paper 2. The samples Fuji, Ketac and Equia are not yet fully analyzed but mentioned in Chapter 3.

GIC	Powder Composition	% by weight	Liquid composition	% by weight
Poly (Ionofil Molar AC)	Fluoroaluminosilicate glass	50 - 100%	Polyacrylic acid	25 - 50%
	Polyacrylic acid	5 - 10%	Water	50-75%
	(+)- Tartaric acid	2.5 - 5 %		
Aqua (Aqua Ionofil Plus)	Fluoroaluminosilicate glass	50 - 100%	Water	100%
	Polyacrylic acid	10 - 25%		
	(+)- Tartaric acid	2.5 - 5 %		
Hema (Ionolux)	Fluoroaluminosilicate glass	50 - 100%	2-hydroxyethyl methacrylate	25-50%
	Polyacrylic acid	5 - 10%	Polyacrylic acid solution	10-25%
			Glycerin dimethacrylate	10-25%
			Urethane dimethacrylate	10-25%
Fuji (Fuji IX GP)	Fluoroaluminosilicate glass	95%	Polyacrylic acid	40-30%
	Polyacrylic acid	5%	Tartaric acid	5 - 10%
			Polybasic carboxylic acid	5-10%
			Water	50%
Equia (Equia Forte Fil)	Fluoroaluminosilicate glass	<99.5%	Polyacrylic acid	5-10%
	Iron(III) oxide	< 0.5%	Polybasic carboxylic acid	5-10%
			Tartaric acid	12%
			Water	78%
Ketac (Ketac Molar Aplicap)	Nuc-oxide glass chemicals (non-fibrous)	85 - 95%	Copolymer of acrylic acid-maleic	35 - 55%
	Copolymer of acrylic acid-maleic acid	1 - 6 %	Water	40 - 55%

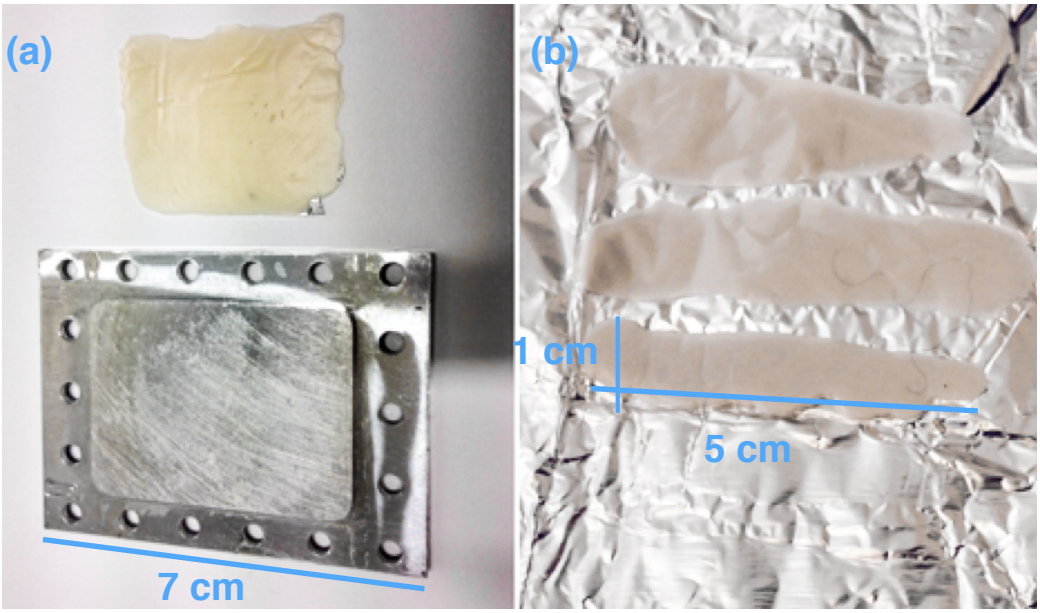

Figure 2:1 Pictures of GIC samples after ageing. (a) The sample as a thin film for the neutron scattering experiments, placed next to a sample holder. (b) Three rows of the same GIC as prepared for colorimetric studies.

2.2 Thermogravimetric analysis and Fourier transform infrared spectroscopy: Decomposition analysis

In thermogravimetric analysis (TGA) we measure the changes in mass of materials as a function of increasing temperature. When coupled to a Fourier transformed infrared (FTIR) spectrometer, which measures the infrared absorption spectrum of the heated sample, the decomposing components of the material can be identified.

In Paper 2 this approach was used to, not only identify the composition of the GIC (Poly and Aqua), but also to characterize the different states or populations of the proton in the matured cements. By comparing the decomposition temperatures with the absorption spectrum, we differentiate water in its bulk-like state from water confined in the polymeric network. By measuring GIC at different maturation periods (7 or 28 days), we can obtain how progressive the water binding is over time for the different samples. This information is crucial for the neutron spectroscopy analysis, as it helps to separate the proton populations in the QENS spectrum and to identify vibrations in the IINS data. Moreover, by combining TGA-FTIR with neutron spectroscopy, we can investigate if and how the progressive water binding is influencing the liquid dynamics of the GIC.

All samples were measured using a TG 209 F1 Libra from Netzsch coupled to a Fourier transform infrared spectrometer PERSEUS from Brucker. The experimental conditions were: N_2-atmosphere (20 ml/min), heating rate of 10 K/min. The measurements were performed between 20 °C (293 K) and 900 °C (1173 K) in a standard Al_2O_3 crucible. An empty crucible was also

measured for instrument correction. The data was processed using the software provided by Netzsch. A new FTIR spectrum of the evolved gases is recorded for every 3 degrees of data collection, thus allowing for selecting spectrum at temperatures of interest based on the TGA data.

On the day of the measurement, the flat aluminium sample holder sealed with Indium wire was opened; one of the triplicates was gently ground using a mortar and pestle, while the 2 other samples were resealed. All triplicates were measured on the same day. Due to the reproducibility of the measurements in the 5 day-old samples, the 28 day-old samples were only measured once. All samples weighted approx. 40 mg.

2.3 Differential scanning calorimetry: Transition temperature analysis

Differential scanning calorimetric (DSC) is a thermoanalytical technique that measures the difference in amount of heat required to increase or decrease the temperature of a sample, compared to a reference, as a function of temperature. When a sample undergoes a physical transformation such as structural phase transitions or glass transitions, more heat (endotherm) or less heat (exotherm) will be needed to maintain the same temperature. By monitoring the difference in heat flow between the sample and the reference during such transitions, we measure the amount of heat absorbed or released.

In this study the technique was used to identify the water populations in the PAA liquids (Paper 1). By measuring the phase transitions in the liquids, we can identify transitions caused by different populations such as bulk-water and water within the polymer network. This understanding facilitates the QENS analysis. Secondly, DSC was also used to investigate the heat capacity and phase transitions of the different component in the matured GIC (data not shown in this thesis, but mentioned in Chapter 3). By measuring under the same physical conditions as in the TGA, we can pinpoint the phase transition of the specific component.

All samples were measured using a DSC 214 Polyma from Netzsch. The experimental conditions were: N_2-atmosphere (40 mL/min), heating/cooling rates of 2, 5 and 10 K/min. The samples weights were approximately 20 mg. The measurements on the liquids were performed on cooling between 40 ºC (313 K) and −180 ºC (93 K). After the first cooling at 10 K/min, the sample was kept at the lowest temperature for 5 minutes and then heated up to 40 ºC. Reproducibility of the process was verified after having kept the sample at 40 ºC for 5 minutes and then cooling it again using the same rate. For each different heating/cooling rate, the same procedure was followed. The measurements where performed in an aluminum-closed crucible. The measurements on the matured GIC were performed on heating between 20 ºC (293 K) and 600 ºC (873 K) in an aluminum-pierced crucible, for direct comparison with the TGA measurements. An empty crucible was also measured and used for instrument correction. The data was processed using the software provided by Netzsch.

2.4 Neutron spectroscopy: Dynamics of the different states of the proton

Neutron scattering is ideal for studying the structure and dynamics of materials, since the characteristic wavelength of thermal neutrons is of the order of the interatomic spacing in a crystal, and the energy matches that of elementary excitations at molecular levels[39]. Additionally, the scattering from neutrons is from the nucleus, rather than from the electron cloud in an atom, which means that there is no correlation between the neutron scattering cross-section and the atomic number of the scatterer. In contrast with X-rays, neutron scattering makes the study of lighter elements possible. Furthermore, as the neutron scattering cross section is different for different isotopes, isotopic contributions can be distinguished experimentally. These unique properties make neutrons ideal for probing the structure and dynamics in hydrogenous solids and liquids and make this technique extremely useful for analyzing the dynamics of liquids in confinement.

Depending on the finite energy transfer between the neutrons and the sample, the neutron scattering response can be inelastic, quasi-elastic or elastic Figure 2:2. The inelastic signal probes the periodic motions of the molecules in the sample with a finite energy transfer. Quasi-elastic neutron scattering (QENS) is well suited to gather quantitative information about the correlation times and length scales of the diffuse motion occurring in hydrogenous materials in confined geometries. In the particular case of broadening of the elastic scattering line we can probe the random diffusive motions of the molecules on a time scale of nanoseconds to picoseconds, and acquire qualitative information relating to the geometrical mechanism of the motion as well.

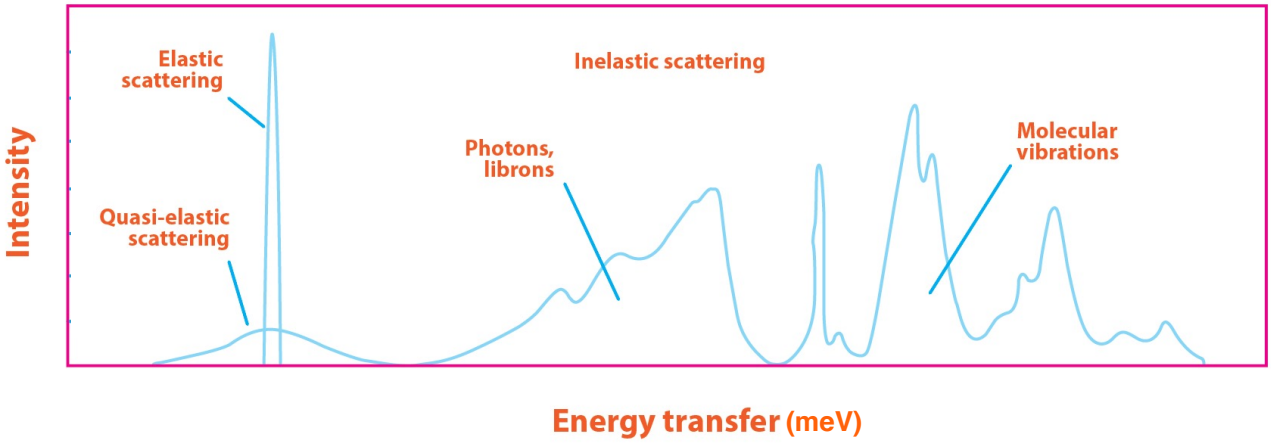

Figure 2:2 Schematic of the neutron scattering spectrum from samples dominated by hydrogen atoms. The spectrum can be separated in elastic, quasi-elastic and inelastic responses.

2.4.1 Basic Neutron Spectroscopy Theory

This chapter briefly describes molecular motion probed using neutron spectroscopy. During a neutron scattering experiment, the measured quantity is called the double differential cross section, $\frac{d^2\sigma}{d\Omega dE'}$. It is defined as the number of neutrons that are scattered per second into a small solid angle, $d\Omega$, around a given direction, having the final energy between E' and $E'+dE'$ divided by the incoming neutron flux[39].

Under the assumption that the system contains a large number of nuclei, the double differential cross-section, averaged over a large number of scattering systems, takes the following form[39]:

$$\frac{d^2\sigma}{d\Omega dE'} = \frac{k_f}{k_i}\frac{1}{2\pi\hbar}\sum_{i,j}\langle b_i b_j\rangle \int_{-\infty}^{\infty}\langle e^{-i\mathbf{Q}\cdot\mathbf{r_i}(0)}e^{-i\mathbf{Q}\cdot\mathbf{r_j}(t)}\rangle \cdot e^{-i\omega t}dt \tag{1}$$

where k_f and k_i are the final and initial wave vectors and $\mathbf{Q}$ the scattering vector. b_j is the scattering length of a nucleus, j, and $\mathbf{r_j}(t)$ is the position of that nuclei at the time t. The equation above can be separated into two parts, one governing the time correlations between N different scatters $(i \neq j)$, and the other describing the self-correlations $(i = j)$. If separated, the equation takes the following form:

$$\begin{aligned}\frac{d^2\sigma}{d\Omega dE'} = {} & \frac{k_f}{k_i}\frac{1}{2\pi\hbar}\sum_{i\neq j}\langle b\rangle^2 \int_{-\infty}^{\infty}\langle e^{-i\boldsymbol{Q}\cdot\boldsymbol{r}_i(0)}e^{-i\boldsymbol{Q}\cdot\boldsymbol{r}_j(t)}\rangle \cdot e^{-i\omega t}dt \; + \\ & \frac{k_f}{k_i}\frac{1}{2\pi\hbar}\sum_{i}\langle b^2\rangle \int_{-\infty}^{\infty}\langle e^{-i\boldsymbol{Q}\cdot\boldsymbol{r}_i(0)}e^{-i\boldsymbol{Q}\cdot\boldsymbol{r}_i(t)}\rangle \cdot e^{-i\omega t}dt.\end{aligned} \tag{2}$$

With the coherent (σ_{coh}) and incoherent cross-sections (σ_{inc}) defined as follows:

$$\sigma_{coh} = 4\pi\langle b\rangle^2 = 4\pi b_{coh}^2 \tag{3}$$

and

$$\sigma_{inc} = 4\pi(\langle b^2\rangle - \langle b\rangle^2) = 4\pi b_{inc}^2 \tag{4}$$

where $\langle \quad \rangle$ represents am average value. Using the definition above we can then define the double differential cross section (for purely nuclear scattering) as:

$$\frac{d^2\sigma}{d\Omega dE'} = \frac{1}{4\pi}N\frac{k_f}{k_i}\left(\sigma_{coh}S_{coh}(\boldsymbol{Q},\omega) + \sigma_{inc}S_{inc}(\boldsymbol{Q},\omega)\right) \tag{5}$$

where $S(\mathbf{Q},\omega)$ is the dynamic scattering function. In equation 5, it is important to note that we can mathematically separate the coherent part from the incoherent one. Consequently, we can define the coherent and incoherent dynamic scattering functions, $S_{coh}(\mathbf{Q},\omega)$ and $S_{inc}(\mathbf{Q},\omega)$, as:

$$S_{coh}(\mathbf{Q},\omega) = \frac{1}{N}\frac{1}{2\pi\hbar}\sum_{i,j}\int_{-\infty}^{\infty}\langle e^{-i\mathbf{Q}\cdot\mathbf{r_i}(0)}e^{-i\mathbf{Q}\cdot\mathbf{r_j}(t)}\rangle \cdot e^{-i\omega t}dt \tag{6}$$

$$S_{inc}(\mathbf{Q},\omega) = \frac{1}{N}\frac{1}{2\pi\hbar}\sum_i \int_{-\infty}^{\infty} \langle e^{-i\mathbf{Q}\cdot\mathbf{r_i}(0)} e^{-i\mathbf{Q}\cdot\mathbf{r_i}(t)}\rangle \cdot e^{-i\omega t} dt \tag{7}$$

Incoherent scattering occurs from the deviation of the mean value of the scattering length from the random distribution. Since, as mentioned earlier, different elements have different isotopes and spin-states, the scattering length will also vary. The incoherent scattering is the part of the neutron wave that interacts independently with each nucleus in the sample. This means that the scattering wave from different nuclei has random relative phases and therefore cannot interfere constructively with each other. Thus, incoherent scattering only depends on the time evolution of the position of the same nuclei without giving information on the static structure.

The coherent scattering, on the other hand, corresponds to the scattering of a system containing the same nuclei. This means that all nuclei have the same average scattering length, $<b>$, so the incident wave interacts with all the nuclei in the sample in a coordinated way. This means that the scattered wave has a definite relative phase, and therefore can interfere with each other. Consequently, the coherent scattering holds information on the correlation of the positions of different nuclei at different times. Hence the coherent scattering reflects interference effects and contains the time dependent structural information about the sample.

In practice, when performing a neutron scattering experiment, one always measures a combination of both coherent and incoherent scattering. However the weight of both contributions is sample dependent. If the interest of the investigation is structural information, it is necessary to try to minimize the incoherent contribution to the differential cross section. If, on the other hand, the interest is to measure the dynamics of protons, the dominating weight from the mobile protons should be incoherent scattering.

The scattering functions can also be represented in momentum and time by Fourier transforming $S(\boldsymbol{Q},\omega)$, which gives the intermediate scattering functions:

$$I_{coh}(\boldsymbol{Q},t) = \frac{1}{N}\sum_{i,j} \langle e^{-i\boldsymbol{Q}\cdot\boldsymbol{r}_i(0)} e^{-i\boldsymbol{Q}\cdot\boldsymbol{r}_j(t)}\rangle, \tag{8}$$

$$I_{inc}(\boldsymbol{Q},t) = \frac{1}{N}\sum_{i} \langle e^{-i\boldsymbol{Q}\cdot\boldsymbol{r}_i(0)} e^{-i\boldsymbol{Q}\cdot\boldsymbol{r}_i(t)}\rangle. \tag{9}$$

We can furthermore Fourier transform the intermediate scattering functions, $I(\boldsymbol{Q},t)$, to space, which provides the real space self-correlation functions, $G(\boldsymbol{r},t)$ and $G_s(\boldsymbol{r},t)$

$$G(\boldsymbol{r},t) = \frac{1}{(2\pi)^3}\int I_{coh}(\boldsymbol{Q},t)\, e^{-i\boldsymbol{Q}\cdot\boldsymbol{r}} d\boldsymbol{Q}, \tag{10}$$

$$G_s(\boldsymbol{r},t) = \frac{1}{(2\pi)^3}\int I_{inc}(\boldsymbol{Q},t)\, e^{-i\boldsymbol{Q}\cdot\boldsymbol{r}} d\boldsymbol{Q}. \tag{11}$$

Given that a particle is at the origin at $t=0$ the probability that any particle (including the origin particle) is in the volume $d\boldsymbol{r}$ at position $\boldsymbol{r}$ at time t is $G(\boldsymbol{r},t)$. Whereas $G_s(\boldsymbol{r},t)$ gives the probability that, given that a particle is at the origin at $t=0$, the same particle is in a volume $d\boldsymbol{r}$ at position $\boldsymbol{r}$ at

time t[39]. It is worth noting that $G(\boldsymbol{r},t)$ has the dimension [volume]$^{-1}$ whereas $S(\boldsymbol{Q},\omega)$ has the dimension [energy]$^{-1}$. The relation between the $S(\boldsymbol{Q},\omega)$ and $G(\boldsymbol{r},t)$ is illustrated in Figure 2:3

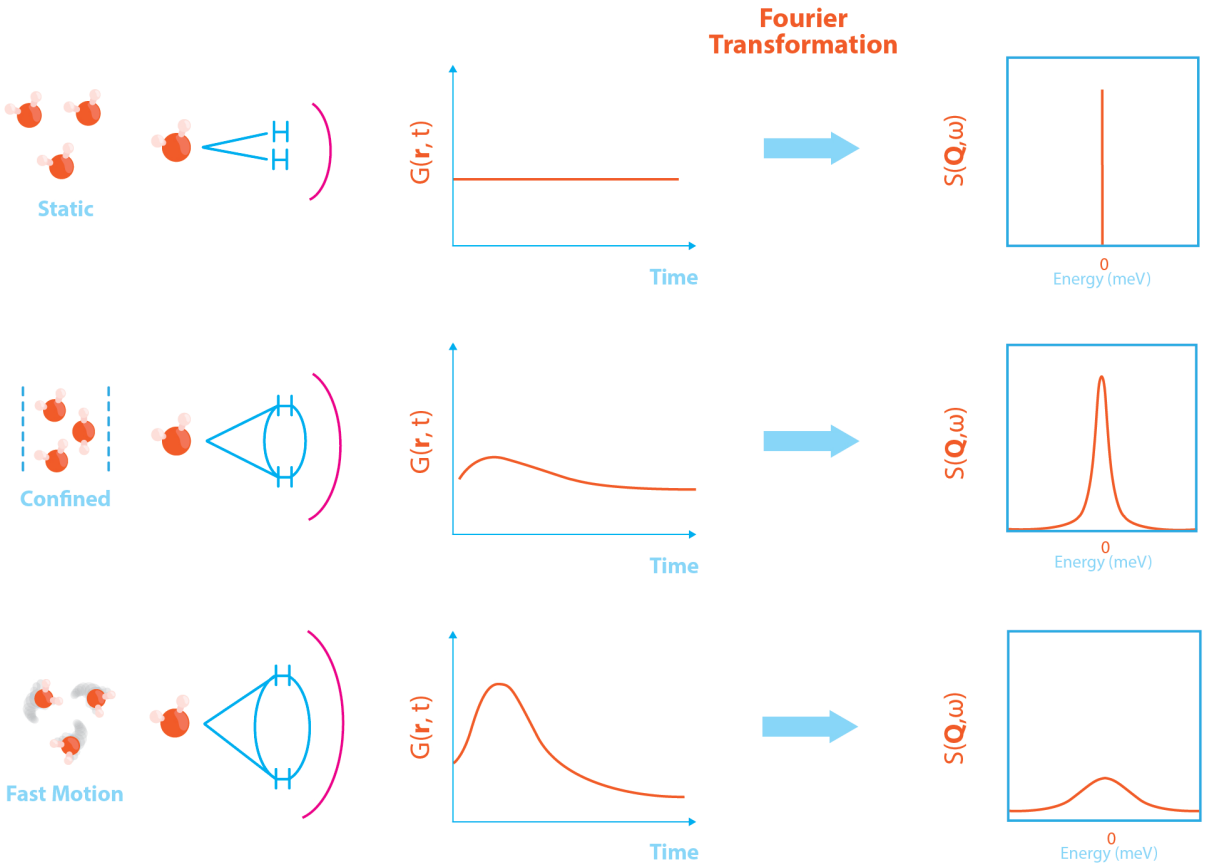

Figure 2:3 Schematic of the relation between $S(\boldsymbol{Q},\omega)$ and $G(\boldsymbol{r},t)$, where a static motion will correspond to the probability of finding the particle at a position $\boldsymbol{r}$ at time t constant, which would result in a static energy transfer around 0. On the other hand, a dynamical motion will increase the probability of finding the particle at a position $\boldsymbol{r}$ at $t>0$, giving rise to a broadening around 0 energy transfer.

As mentioned above, the measured quantity in neutron spectroscopy is the double differential cross section, however for all intents and purposes the observed quantity is the scattering function, $S(\mathbf{Q},\omega)$, where $\mathbf{Q}$ is the magnitude of the scattering wave vector and ω is the energy transfer. In this study, the scattering function will be dominated by the incoherent scattering due to the high amount of water and hydrogen in the samples. In turn, $S(\boldsymbol{Q},\omega)$ can be divided in three main components: the elastic scattering function, $S_E(\boldsymbol{Q},\omega=0)$, the quasi-elastic signal, $S_{QE}(\boldsymbol{Q},\omega\approx0)$ and the inelastic signal, $S_{IN}(\boldsymbol{Q},\omega>0)$.

The first component, the elastic scattering function, $S_E(\boldsymbol{Q},\omega=0)$, is related to the thermal fluctuations of the atoms around their equilibrium position. Since the scattering from the samples studied in this thesis is mostly incoherent, the evolution of $S_E(\boldsymbol{Q},\omega=0)$ as a function of energy, time and temperature allows probing immobility, and indirectly mobility of the hydrogen atoms. This

will be further discussed in the upcoming section reserved for the elastic fixed window (EFW) approach, section 2.4.2.

The second component of the scattering function is called the quasi-elastic signal (QE), where $S_{QE}(\mathbf{Q},\omega\approx 0)$ is the dynamical scattering function that describes molecular diffusion, such as translational and rotational motions. The analysis of this component allows distinguishing free, confined or chemically bound hydrogen dynamics within the observation time of the selected spectrometer. The analysis of the QE signal is the main the focus of this thesis. This part of the scattering function will be further described in section 2.4.3.

The final component of the scattering function is the inelastic signal, $S_{IN}(\mathbf{Q},\omega>0)$, where we probe phonon and molecular vibrations and material phonon densities. This will be further elaborated in section 2.4.2.

2.4.2 Elastic fixed window approach

The elastic fixed window (EFW) approach provides an overview of the molecular mobility in the sample as a function of temperature or time, and is usually a good starting point of every experiment[28]. Here we assess the evolution of only those neutrons scattered elastically by the sample within the resolution. Since there is conservation of energy, when the width of the dynamic scattering function, $S_{QE}(\mathbf{Q},\omega\approx 0)$, changes with increasing temperature or time, the elastic intensity will also change. In other words, the elastic intensity decreases if the dynamic scattering increases, as is the case when increasing temperature. This is because the characteristic relaxation time becomes of the order of, or larger than, the instrument resolution. Thus it is possible to determine the onset of the proton mobility by noting points of inflexions in the elastic scattering response. In contrast, by evaluating the elastic intensity as a function of time, it is possible to follow the hydration process in the samples, and thus access the hydrogen bond formation rate. A schematic overview of an EFW scan is depicted in Figure 2:4 where we observe the relation between the normalized intensity and the related broadening of the signal.

In this study, EFW scans were performed using IN10 and IRIS (both instruments are described in section 2.4.6) in two distinct ways that were determined by the specific instrumental setup. On IN10, the measurements were performed by keeping the Doppler still, so that $\Delta\omega = 0$, which results in fixed initial and final wave vectors, $k_i = k_f$. On IRIS, on the other hand, the EFW was obtained by integrating over the elastic signal within the instrument resolution. In both cases, we count the elastically scattered neutrons defined as $I_E(\mathbf{Q}) = S_E(\mathbf{Q}, \omega = 0)$.

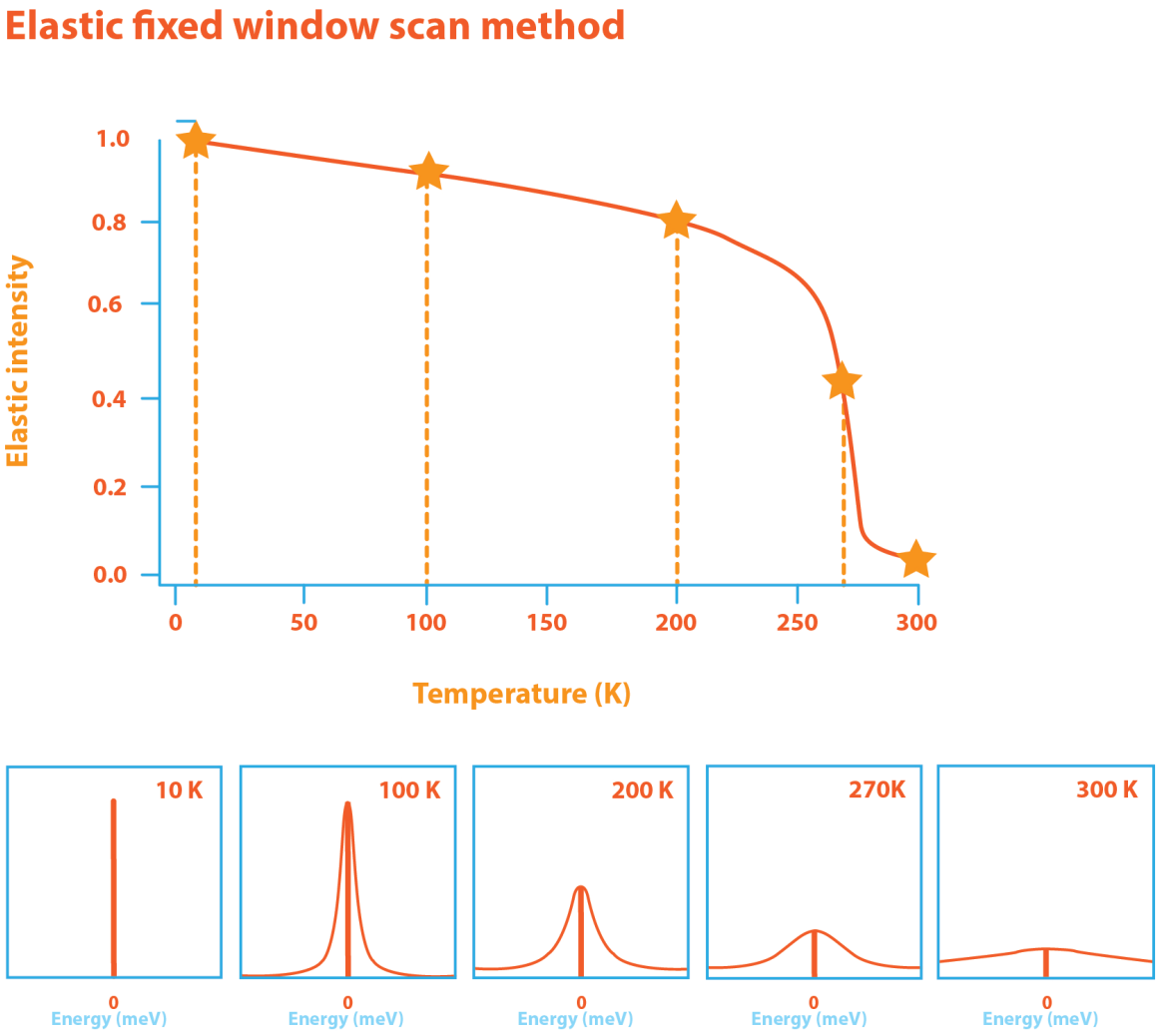

Figure 2:4 Concept of the elastic fixed window (EFW) approach. Each star corresponds to a specific temperature, with the respective scattering from the selected temperatures illustrated at the bottom of the figure. As the amount of scatter is constant, the intensity corresponding to static particles will decrease as the system becomes dynamic. This analysis allows probing the onset mobility of the system.

A typical EFW scan for the Poly and the PAA solution using these two instruments is shown in Figure 2:5. By using two different backscattering spectrometers with different instrument resolutions, we can probe different relaxation times originating from different proton populations in the same sample. In this figure, the EFW is analyzed from the data obtained using IN10, with the instrument resolution of 1.0 μev, corresponding to a time resolution of 4.1 ns, and IRIS, with the instrument resolution of 17.5 μev, corresponding to a time resolution of 240 ps (see section 2.4.5 for details on energy and observation time relations). By monitoring the onset of the proton mobility using the EFW approach from the same sample but using different instruments, we verified that different populations of protons were present. The different proton populations will correspond to different broadenings (see Figure 2:4), which can provide information on the specific diffusion, see 2.4.3. It furthermore gives an indication at which temperature a longer scan should be measured.

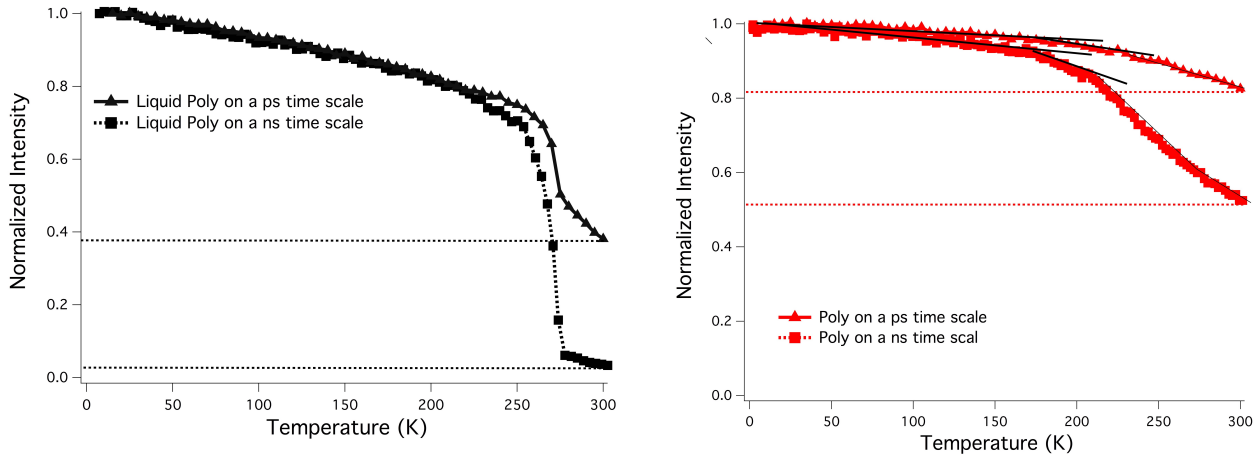

Figure 2:5 EFW scans for Liquid PAA (black) and Poly matured for 28 days (red) using different time windows. Each sample was measured on both IN10 (instrument resolution of 1.0 μev, time resolution of 4.1 ns) and IRIS (instrument resolution of 17.5 μev, time resolution of 240 ps). By monitoring the onset of the proton mobility with different instrument resolutions, we probed different relaxation times originating from different proton populations in the same sample. We note that what might appear less mobile on one resolution is more dynamic on another, as illustrated by the horizontal dotted lines.

In Paper 1, the EFW approach was also used to study the hydration of Poly and Hema, by measuring the first 24 hours of setting for two freshly mixed cements. In this approach, the dynamical scattering function decreases with time as the cement hardens. Since the signal is dominated by the hydrogen, the time evolution of immobile protons that forms during the cements' hydration process was probed using the following equation:

$$\mathrm{IHI} = \frac{\text{elastic intensity of the hydrating cement}}{\text{total intensity of the liquid at 2 K}} \tag{12}$$

Since the protons from the GIC and the RMGIC come mainly from the liquid, we can account for the incoherent response from the hydrogen atoms by normalizing the signal to the total intensity at the lowest temperature.

2.4.3 Quasi-elastic scattering

In contrast to the EFW method, we now consider not only the $S_E(\boldsymbol{Q}, \omega = 0)$ part of the scattering function, but also the surrounding dynamical signal $S_{QE}(\boldsymbol{Q}, \omega \approx 0)$. $S_{QE}(\boldsymbol{Q}, \omega \approx 0)$ from hydrogenous samples results from three types of motion: rotational, translational and vibrational, which can occur at the same time. However, during data analysis this is simplified by assuming that these three types of motions are independent. In the case of the translational and rotational motions

for both confined and bulk molecules, the behavior can be extracted by fitting the QENS signal using a sum of Lorentzian functions $L_n(\Gamma,\omega)$ using the following expression:

$$S(Q,\omega) = DWF\,[(A_0(Q)\delta(\omega) + (1\text{-}A_0(Q)\ \sum_{i=1}^{n} L_n(\Gamma,\omega)) \otimes R(Q,\omega)] + B(Q) \quad (13)$$

In this equation DWF represents the Debye Waller factor describing the attenuation caused by thermal motion. $A_0(Q)$, defined as the elastic incoherent structure factor (EISF), describes the time averaged spatial distribution of all scatters. The term $\sum_{i=1}^{n} L_n(\Gamma,\omega)$ indicates the sum of Lorentzians representing the broadened energy distribution that results from neutron-nucleus collisions, corresponding to the motions describing the distinct relaxation processes. Γ is the Lorentzian width. The extracted molecular diffusion can be modelled based on the obtained half width at half maximum (HWHM) of each Lorentzian as a function of its Q-dependence. $R(Q,\omega)$ denotes the resolution function of the instrument, which will be further elaborated in section 2.4.5. $B(Q)$ represents a background term including the dynamics that are too fast for the instrument resolution. $\delta(\omega)$ is a delta function describing the particles seen as immobile in the time window probed by the instrument.

In the simplest case, Brownian motion, the distance travelled by a proton (or any type of atom) between any two successive collisions is smaller than any other distance of relevance, and thus the motion will appear continuous. However, if we probe smaller distances, the distance between successive collisions becomes comparable, and the motion starts to look more discrete. This means that in Q-space the motion starts to "plateau" at higher Q-value, thus deviating from the simple DQ^2. In this case, the dynamics take the form of jump diffusion. In this study two jump diffusion models were used. The first, commonly used to describe water in confinement (Paper 2, Paper 3 and Paper 4), is the Singwi-Sjölander model[29], which uses a random distribution of jump lengths:

$$\Gamma(Q) = \frac{DQ^2}{1 + DQ^2\tau_0} \quad (14)$$

where τ_0 corresponds to the residence time and D is the translational diffusion constant given in terms of the mean jump length $\langle l \rangle_{AV}$ given as:

$$D = \frac{\langle l \rangle_{AV}}{6\tau_0} \quad (15)$$

However, for describing the variation of the half width at half maximum (HWHM) as a function of Q for the PAA (Paper 2), the Singwi-Sjölander diffusion model could not be satisfactorily applied, instead the Chudley-Elliott[40] model showed good agreement. This model assumes that the molecular motion takes the form of discrete jumps, in which the molecule remains at a given site for a specific time (residence time), before jumping instantly to another site separated from the first by a jump length:

$$D = \Gamma(Q) = \frac{1}{\tau_0}\left(1 - \frac{sin(Ql\ sin\,\theta)}{Ql\ sin\,\theta}\right) \quad (16)$$

where τ_0 is the residence time and l the jump length. This model is commonly used to describe the HWHM vs. Q obtained for caged moleules[41], i.e. an atom or molecule enclosed in cage formed by other atoms or molecules from time to time perform a jump into a neighboring cage.

Further information can be obtained from the QENS response by looking at the EISF, defined as the ratio between the elastic and the total intensity from both the elastic and quasi-elastic signal:

$$\mathrm{A_0(Q)} = \mathrm{EISF} = \frac{S_E(\boldsymbol{Q}, \omega = 0)}{S_{QE}(\boldsymbol{Q}, \omega \approx 0) + S_E(\boldsymbol{Q}, \omega = 0)} \tag{17}$$

The EISF can be interpreted as the probability to find a particle in the same volume after a time interval has passed. This is a unique tool to determine the geometry of the molecular motion. Considering that the type of confinement influences the local geometry of the molecule, the evolution of the EISF can shed light on the specific type of geometrical restrictions. In this study, since most scattering is from water, the evolution of the EISF fits very well with the modified model for confined water, namely diffusion of a point particle inside an sphere[42], given by:

$$A_0(Q) = p + (1-p)\left(\frac{\frac{3\,sin\,Qd}{Qd^2} - \frac{3\,cos\,Qd}{Qd}}{Qd}\right)^2 \tag{18}$$

where d is the radius of the idealized spherical confinement, and p accounts for the immobile fraction of the protons seen within the instrument resolution. This approach was used in Paper 2 to separate and study the type of confinement seen on different time windows.

2.4.4 Neutron Vibrational Spectroscopy

The inelastic response, $S_{IN}(Q,\omega>0)$, covers the energy range corresponding to internal modes and molecular vibrations, which probes the neutron that scatters inelastically from the sample with an exchange of energy equal to the vibrational transition energy.

Neutron vibrational spectroscopy is ideal to study the structure and dynamics of water in confinement, since the translational frequencies will change with the local structure of the water[43–45]. This approach was used in Paper 3. Additionally, we can acquire information on the strength of the H-bond interaction, since the interatomic forces determine a particular phonon mode. Because selection rules are not involved, incoherent inelastic neutron scattering (IINS) measures all the modes simultaneously. By comparing the IINS spectrum obtained for each sample at a different maturation period, it is possible to probe changes on the vibrational response as the sample ages. Such information gives insight on the molecular properties and development of the hydrogen bond network. Furthermore, the inelastic incoherent neutron scattering (IINS) spectrum is directly proportional to the density of states and the scattering lengths of the related atoms, thus in Paper 2 we also used this to identify a density change due to increased crosslinking.

2.4.5 Time and Energy Resolution

Energy resolution, $R(Q,\omega)$, is a measure of the precision of the obtained signal. The energy resolution, usually given in terms of full width at half maximum (FWHM), describes the range at which the signal can be distinguished between two closely lying energies. In the idealized case, the instrument energy resolution would only measure in the frequency domain of the quantity proportional to the double differential cross section, $\frac{d^2\sigma}{d\Omega dE'}$. However, in an experimental setup, the resolution is a peaked function, usually a Gaussian, whose width, $\delta(\omega)$, depends on how well the specific instrumental setup can select ω. Not all molecular motions happen in the same timescale and therefore matching the variation in energy to the specific motion, i.e. vibration, libration, fast diffusion, slow diffusion, etc. is essential. This means that in an experimental setup, a glassy liquid, for example, may show no elastic scattering using one resolution, but give rise to elastic scattering on another. This is depicted in Figure 2:6, where we see the QENS signal from one sample (Poly) at specific Q value obtained using three different spectrometers with different resolutions. The figure shows how the resolution of the instrument can change the measured signal, and how a dynamical signal on one resolution can be seen as static on another. The variation in $\omega, \Delta\omega$, defines the upper time limit of $G(r, t)$. This upper time limit gives information about the type of motion that can be probed in the experimental setup.

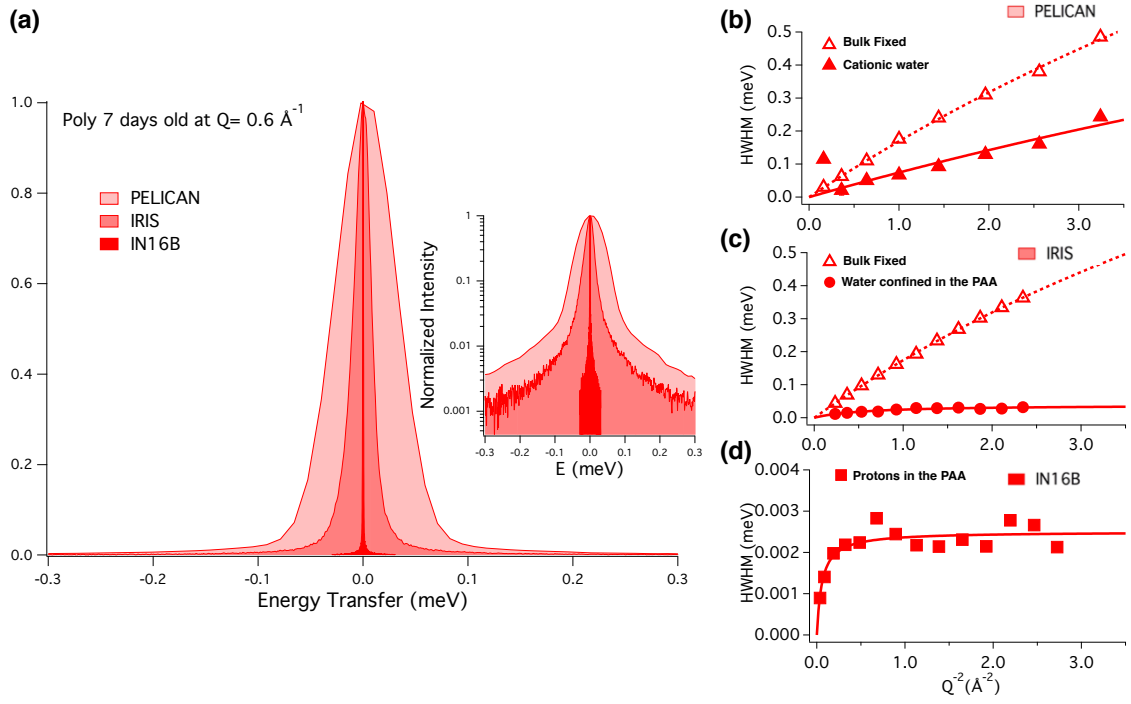

Figure 2:6 Illustration of the effect of the instrument resolution and observed quasi-elastic broadening. On the left side of the figure we see an example of the same sample measured using 3 different spectrometers, namely PELICAN, IRIS and IN16B at Q=0.6 Å^{-1}. If the selected resolution matches particular molecular motions, quasi-elastic signal is detected. Note that the intensity is normalized to better compare the broadening. On the right, we show how the decoupled HWHM can be extracted by combining the different observation times covered by these spectrometers.

Moreover, from the spectrometer energy resolution, we can estimate the time resolution (observation time):

$$T = \frac{h}{FWHM} \tag{19}$$

where T is the observation time, h is Planck constant $h = 2\pi\hbar = 6.626 \times 10^{-34}$ Js and FWHM is the instrument resolution at full width half maximum. This corresponds to a relaxation time of:

$$\tau = \frac{FWHM}{2\omega} \tag{20}$$

In conclusion, when designing an experiment choosing an instrument corresponding to the desired "time window" or energy resolution is key for studying dynamics in hierarchical porous structures, se Figure 2:7. This is especially important when identifying distinct states of the proton in bulk state or in confinement. It is worth remembering that a relation between energy range and energy resolution also exists, i.e. a high-resolution instrument does not cover the same energy range as the one accessible using low-resolution instruments.

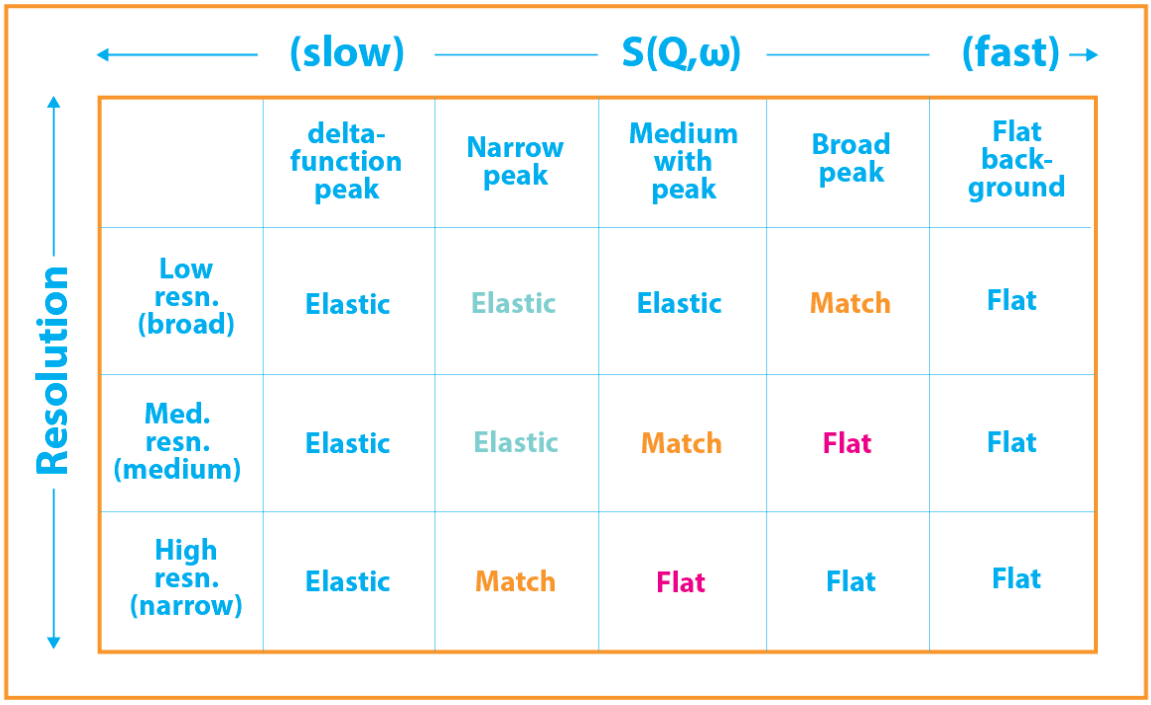

Figure 2:7 Relations between resolution and the observed Quasi-elastic scattering function. If the relaxation time of the motion does not match the energy resolution, the observed signal will appear in the background or as static. Adapted from [46]

2.4.6 Instrumental setup

2.4.6.1 Vibrational spectroscopy

VISION is a vibrational spectrometer located at the Spallation Neutron Source in Oak Ridge, USA. The instrument follows the scattered neutrons with energy loss (Stokes side) by exciting the vibrational modes of the sample. VISION is optimized to characterize molecular

vibrations in a wide range of crystalline and disordered materials over a broad energy range (> 5 to < 600 meV). As the intensity of an Inelastic Neutron Scattering (INS) band is proportional to the Debye–Waller factor, which magnitude is in part determined by the thermal motion of the molecule, measuring the INS spectra at 10 K can reduce this factor. This spectrometer was used in Paper 2 aiming to clarify the ambiguity related to the density change during maturation in the Aqua and Poly cements as well as to better understand the effects of maturation.

2.4.6.2 Direct time of flight spectrometers

Time-of-flight spectrometers can be grouped into two; direct and indirect geometry. In this thesis we have used two direct geometry instruments, which means that the energy of the incoming neutrons is constant. The basic principle is to send a pulsed monochromatic beam on the sample, and then measure the time of arrival. Hence, the measured velocity of the scattered neutrons determines the energy transfer between sample and neutrons. In PELICAN and FOCUS, the monochromatization of the beam is realized with a crystal followed by Fermi-choppers. The beam is divided into short neutron pulses so that the desired wavelength, λ, can be selected by additional Fermi-choppers. The desired wavelength, λ, is selected by the condition $\lambda = \frac{ht_1}{mL_1}$ with t_1 being the time between the opening and L_1 the distance between the choppers. After the monochromatization, the neutrons have a very strong correlation of wavelength and angle. The desired wavelength is selected by a rotating Fermi-chopper, which speed defines the resolution. An additional Fermi-chopper ensures that the slower neutrons first catch up with the faster ones at the detector, so there is no overlap between the pulsed monochromatic beam. The additional chopper sets a time-stamp for the departure time of the neutron pulse to the sample, so that the distance between them, L_2, is precisely known. This means that the scattered neutrons arrive at the detector after a time, t, corresponding to their velocity, and hence their energy. The energy after the scattering is analyzed by measuring the time it takes for the neutron to travel the known distance, L, from the sample to the detector. In this way, we obtain a spectrum of intensity $I(t)$ with energy given by:

$$E_f = \frac{m}{2}\frac{L^2}{t^2} \tag{21}$$

for every detector pixel[47]. The energy resolution is determined by the precision of the measuring flight time and flight path. The width in time Δt of a pulsed beam when arriving at the detector can be derived directly by using geometric arguments. The measured Q-dependence in this setup is related to the difference in magnitude between the initial and final wave vectors, $\mathbf{Q} = \mathbf{k_i} - \mathbf{k_f}$, which consequently means that the energy range will vary for the Q-values.

PELICAN is a direct time-of-flight cold neutron spectrometer located at the Australian Nuclear Science and Technology Organisation (ANSTO)[48]. The spectrometer provides an elastic energy resolution corresponding to an upper experimental observation time of ~ 600 ps covering an angular scattering range of $22° < 2\theta < 119°$. In the study of dental cements, the wavelength λ = 6.0 Å, corresponding to ΔE = 63 μeV at FWHM, was selected in order to probe the fast dynamics, mostly due to the loosely bound water, either in the PAA or confined in the cement structure. In this configuration, the scattering vector, Q, varied from 0.4 $Å^{-1}$ to 1.8 $Å^{-1}$. This spectrometer was used in Paper 2 on the Aqua and Poly samples and their respective liquids, as well as to study Fuji, Ketac

and Equia and their respective liquids. The latter results are briefly mentioned in Chapter 3. The experiments were performed at 310 K corresponding to body temperature. The instrument was used to understand how the free bulk water and the water trapped in the polymer would behave under confinement. With this instrument resolution, it was possible to gain insight on the dynamics of the water confined in hydration shells around the cation in the GIC and the confined water in the PAA.

FOCUS is a cold time-of-flight spectrometer instrument installed at the Swiss spallation neutron source SINQ, which also combines a crystal monochromator with a Fermi Chopper. The instrument uses two interchangeable monochromators (pyrolitic graphite or MICA[49]) and covers a wide incident energy range of 20 meV to 0.25 meV. This spectrometer was used in Paper 3 to understand why two porous materials of similar structure take up different amounts of water. In the study of these chalk samples, the measurement was done using an incident neutron wavelength of 5 Å, resulting in an elastic energy resolution of ~110 μeV, covering relaxation phenomena from 80 ps to 130 fs. The accessible momentum transfer in this setting ranges from 0.4 to 2 $Å^{-1}$, with the corresponding energy transfer ranging from +1.7 to −30 meV. Spectra were collected at six temperatures, ranging between 100 and 300 K.

2.4.6.3 Backscattering spectrometers

Backscattering spectrometers are inverse geometry instruments. This means that the energy transfer between the neutron and the sample are observed by varying the incident neutron energy E_i, while keeping the final energy E_f fixed. The variation in incident neutron energy, E_i, in reactor type instruments (IN10 and IN16B) comes by Doppler shifting the neutron wavelength. In spallation sources (IRIS and BASIS), the backscattering is used only for the energy filtering after the sample. As an energy resolution close to that of the backscattering analyzers is required, it is necessary to use a short pulse in conjunction with a long flight path[47].

If we consider the equation below, we have that a crystal monochromator has its highest resolution for Bragg angles of 90º, that is, in perfect backscattering:

$$\frac{\Delta\lambda}{\lambda} = \cot\theta\Delta\theta + \frac{\Delta d}{d} \tag{22}$$

where $\Delta\theta$ corresponds to the beam divergence and the angular deviation from backscattering, while d is the crystal analyzer lattice spacing. The term $\frac{\Delta d}{d}$ depends on the crystal in use. With this technique we can achieve an energy resolution as high as FWHM ≈ 0.1 μeV – 3.5 μeV for IN10, IN16B, and BASIS by using a Si(111) crystal as analyzer. In the case of IRIS, a FWHM ≈ 17.5 μeV can be reached by using the (002) reflection of pyrolytic graphite crystal analyzer.

The main idea of backscattering spectrometers is based on the fact that the wavelength does not depend on the scattering angle to first order. This means that a Bragg-reflection under an angle of ~ 90 º leads to the decoupling of resolution and divergence to the first order. The backscattering spectrometers measure a quantity proportional to the dynamic scattering function $S(\boldsymbol{Q}, \omega)$ as introduced in section 2.4.1. The 3 different backscattering spectrometers used in this thesis, are described below.

IN10 was located at the cold neutron guide the Institut Laue-Langevin (ILL, France). In this spectrometer Si(111) crystals was used for monochromatizing and analyzing of the neutron beam of λ_i = 6.271 Å corresponding to an incident energy of E_i = 2.08 meV. The scattered neutrons were detected over a *Q*-range of 0.2 $Å^{-1}$ to 2 $Å^{-1}$. The energy transfer, ΔE, between the sample and the neutron covered the range from -15 μeV to 15 μeV with a resolution (FWHM) of ΔE = 1 μeV corresponding to an upper experimental time of ~ 4 ns. This spectrometer was used in Paper 1 for EFW measurements performed between 2 and 310 K on matured Poly and Hema, and as well as to follow the hydration on freshly mixed samples.

IN16B: is a high-energy resolution backscattering spectrometer also located at the ILL[50]. It provides ΔE = 0.75 μeV at FWHM with λ = 6.3 Å, thus allowing an upper experimental observation time similar to IN10. This time window corresponds mostly to the slower polymer-related motion. The instrument resolution is constant over the entire Q-range of 0.190 $Å^{-1}$ to 1.895 $Å^{-1}$, which corresponds to an angular scattering range of 11° < 2θ < 142°. IN16B was used with its standard Si(111) monochromator and analyzer crystal setup[50]. This spectrometer was used in Paper 2 to perform experiments at 310 K on the matured GIC Poly and Aqua. Additionally, measurements were performed on the Liquid PAA, used in preparing the Poly cement, upon temperatures ranging from 260 K to 310 K. This instrument allowed understanding of the proton motions associated with the polymer and the polysalts.

IRIS: located at the ISIS Facility in the UK, provides an elastic energy resolution of 17.5 μeV at FWHM, corresponding to an upper experimental observation time of ~200 ps achieved by neutrons scattered with λ = 6.7 Å. Its resolution is also constant over the entire Q-range of 0.501 to 1.960 $Å^{-1}$ (angular scattering range of 25° < 2θ < 160°). IRIS probes the intermediate dynamics of the loosely and tightly bound water. This spectrometer was used in Paper 2 to carry out measurements at 310 K on matured Poly and Aqua as well as the Liquid PAA used in preparing the Poly cement. This instrument allowed probing water trapped in the polymer chain.

BASIS: is a near-backscattering spectrometer at the neutron spallation source SNS in Oak Ridge, USA[51]. The spectrometer uses Si(111) crystals for analyzing the neutron beam with incident λ_i centered at 6.4 Å. The energy transfer, ΔE, ranges from -150 μeV to +150 μeV with an energy resolution of ΔE = 3.5 μeV at FWHM. The detectors cover an elastic *Q*-range of 0.1 $Å^{-1}$ to 2 $Å^{-1}$**.** The results obtained with this instrument are reported in Paper 4, where we show that the water diffusion in Hepatitis B vaccine in a PBS solution is slowed down when introduced to the mesoporous silica SBA-15.

Chapter 3 Additional Results

In this chapter, I will touch upon two projects, which are important to the understanding of proton dynamics in GIC, which are still ongoing.

The first project (3.1.1) is a preliminary study regarding proton dynamics of the aqueous PAA solutions used to prepare the Ketac, Fuji and Equia GIC cements. The aim of this study is to investigate the dynamics of the liquids and their behavior confined in the GIC by combining DSC, TGA-FTIR and neutron spectroscopy (QENS data collected using PELICAN). Only the DSC data for the different liquids are presented in this section.

The second project (3.1.2) is a preliminary classical molecular dynamics simulation study of the aqueous PAA solution used in the Poly cement, developed during my change of scientific environment. The overall aim is to assess and separate molecular motions of this aqueous PAA solution, specifically the motions of hydrogen, under different conditions and compare the simulated results with data collected at IN16B and IRIS. In this section, only the hydrogen motion related to the water bound to the polymer chain is shown.

3.1.1 Proton dynamics in aqueous PAA solutions

All PAA liquids were investigated using DSC upon cooling, while the matured GIC were studied upon heating. The GIC were also studied using TGA-FTIR and all samples were investigated using QENS. The calorimetric experiments (DSC and TGA-FTIR) were performed as described in sections 2.2 and 2.3, while the QENS technique is described in section 2.4.3 and the instrument setup in 2.4.6

DSC data of the aqueous PAA solutions are shown in Figure 3:1. For all samples, we observe an asymmetric endothermic peak at around 275 K on heating, corresponding to the melting of bulk water. Moreover, we also observe a glass transition at around 250 K for the PAA-Fuji and PAA-Equia, marked by an (*). No glass transition is clearly observed in the PAA-Ketac under these experimental conditions. However, in the latter we observe a double crystallization peak on cooling, indicated by (**) and around 210 K, that occurs at much lower temperature when compared to the other two PAA solutions. This can be attributed to a different water population bound to the PAA. From Paper 1, we know that distinct water populations are present in aqueous PAA solutions, while from Paper 2 we see that these same water populations are accessible using the time-of-flight spectrometer PELICAN. In Paper 2, furthermore, we observe that the water bound to the polymer also remains bound to the polymer in the matured GIC, and that progressive water binding to the polymer chain also occurs. Consequently, from this previous knowledge, the following assumptions can be made to describe this ongoing study:

1. From the DSC data, we observe that the liquids have very distinct water populations.

2. The distinct dynamics of the liquids used in preparing the GIC influence the water binding to the polymer chain in the GIC structure.
3. From literature[52] we know that the selected GIC have different mechanical properties, which might be affected by the nature of the aqueous PAA solution used.

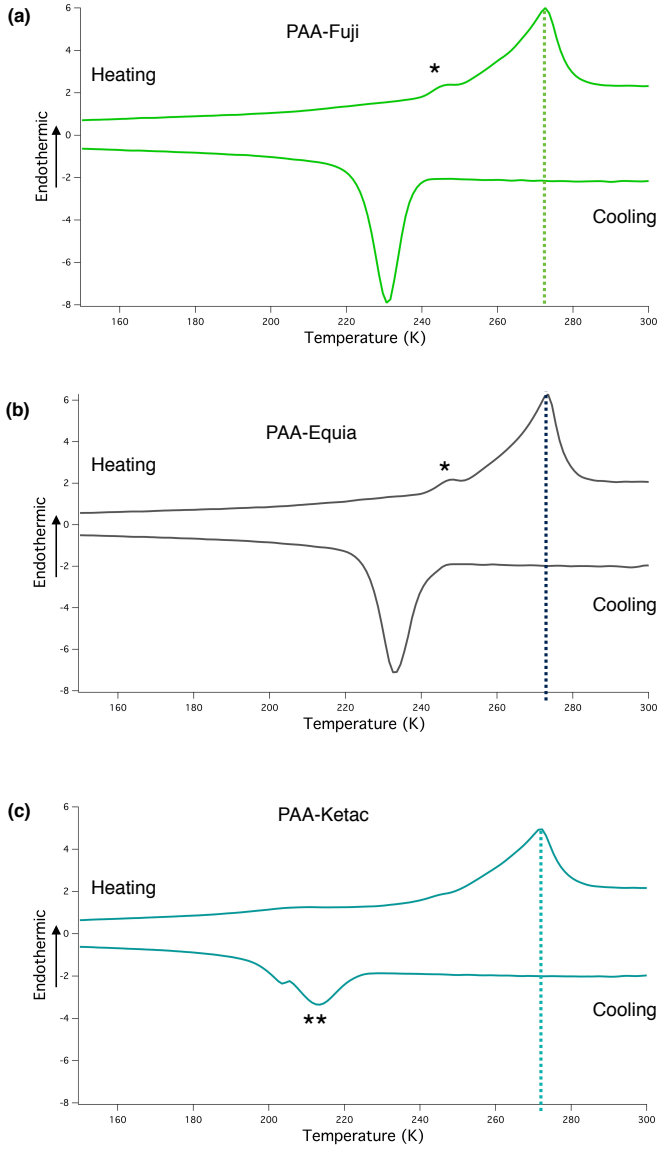

Figure 3:1 Aqueous PAA solutions used in the GIC Fuji (a), Equia (b) and Ketac (c). For all samples the melting temperature upon heating, marked by the vertical line, coincides with that of bulk-like water. In (a) and (b) we observe an asymmetric endothermic peak (glass transition) indicated by (*), which has a markedly different response from that of bulk water. This glass transition temperature shows the presence of a second water population, whose mobility is partially hindered by the interactions with the PAA. In (c) the double crystallization observed on cooling, indicated by (**), can be attributed to a different water population.

3.1.2 Molecular dynamics simulation of the PAA solution

In classical molecular dynamics simulations, the equations of motion are numerically solved, with a given potential, to obtain the trajectories of the individual particles forming the system. Classical molecular dynamics simulations are helpful to gain deeper insight into the molecular processes identified in experimental data. Additionally, in such simulations we can specify many physical factors, which are not always possible in an experimental environment.

To better understand the neutron spectroscopy data collected during this thesis, I used Materials Studio[53] to create an initial conformation for the aqueous PAA solution using "sketch tool". The accurate pH (1.3) was defined in the simulation box by random breaking of double bonds in the PAA molecule. In order to acquire the accurate ionization, the following formula was used:

$$\frac{[COO^{-1}]}{[COOH]} = 10^{pH-pKa} = 10^{pH-4.80}. \quad (23)$$

The PAA polymer chain was built by repeating the PAA molecule 100 times. Then the water molecules were added, in a ratio of 25% PAA and 75% water by weight. The carboxylate anion COO^- was neutralized by adding Na^+ to the simulation box. The simulation box was then repeated to create a super cell of 20 polymer chains. The structure of the entire system was minimized using "Forcite" (PCFF force field) in Materials Studio. The resulting simulation box was saved as LAMMPS[54] input files using a consistent valence force field (cvff)[55].

Prior to collecting data, the simulation box was further minimized before relaxation to room conditions in LAMMPS using constant number of atoms, pressure, and temperature referred to as a NPT integration. The system was then heated up to 600 K and cooled down to the desired temperatures selected based on the DSC experiments (from 260 K to 310 K in steps of 10 K) before running the final relaxations. This step was performed to ensure the correct conditions for the simulation, i.e. to avoid unnatural agglomerations, empty spaces and too low densities. Finally, the data was collected for relaxation times equal to 2 ns and 20 ns.

From the simulations the intermediate incoherent structure factor, *I(Q,t)* (described in section 2.4.1), of the hydrogen atoms were calculated. The hydrogen in the *I(Q,t)* calculations were further separated into the following components:

1. Entire system, containing all the hydrogen in the simulation box;
2. Bulk water;
3. Water bound to the polymer chain (presented in Figure 3:2 in this section);
4. Water transitioning from bulk state (2) to water bound to the polymer chain (3), defined as binding process;
5. Water transitioning from water bound to the polymer chain (3) to bulk water (2), defined as unbinding process;
6. Hydrogen in the polymer chain, which will further be separated in specific bonds i.e. COOH and OH_2 to decouple localized motions within the same energy range.

From the simulated *I(Q,t)*, obtained for Q-values selected based on the experimental data collected at IRIS (0), the structure factor, $S(\boldsymbol{Q},\omega)$, for the water bound to the polymer chain was calculated. This result is shown in Figure 3:2. IRIS was chosen for this comparison because it best probes the associated dynamics of water bound to the polymer chain.

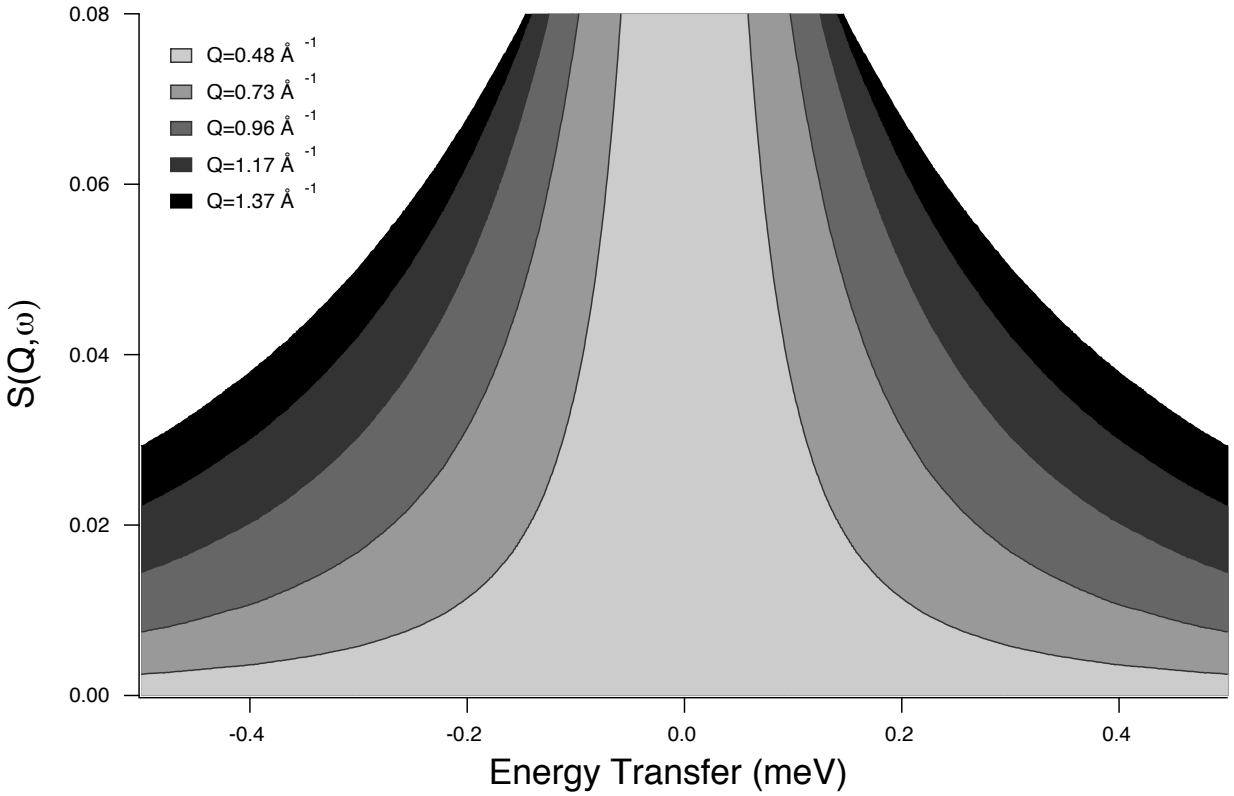

Figure 3:2 Simulated structure factor, $S(Q,\omega)_{sim}$, for the water bound to the polymer chain for selected Q-values corresponding to experimental data collected at IRIS simulated for 2 ns. We see a broadening of the signal as a function of Q. The intensities are normalized in the plot.

The simulated structure factor can then be fitted using the same approach described in section 2.4.3 in the following manner:

$$S(Q,\omega)_{sim} = \left(A_0(Q)\delta(\omega) + \left(1 - A_0(Q) \sum_{i=1}^{n} L_n(\Gamma,\omega) \right) \right) \otimes \mathrm{R}(\mathrm{Q},\omega)_{exp} \tag{24}$$

where $S(Q,\omega)_{sim}$ is the simulated structure factor and $\mathrm{R}(\mathrm{Q},\omega)_{exp}$ is the experimental resolution function.

As the intermediate incoherent structure factor for each hydrogen component can be separated after the simulations, the expression for the structure factor simplifies to:

$$S(Q,\omega)_{sim} = \left(A_0(Q)\delta(\omega) + \left(1 - A_0(Q) L_n(\Gamma,\omega) \right) \right) \otimes \mathrm{R}(\mathrm{Q},\omega)_{exp.} \tag{25}$$

For future work, the combination of projects 1 and 2 will enable a complete study of water binding to the different aqueous PAA solutions. These results have great potential, as it will allow a systematic analysis of concentration and type of acid, and their interaction with water in the aqueous PAA solution. This can lead to better hydration control in the GIC and RMGIC and consequently improve these dental restorative materials.

Chapter 4 Conclusions and Final Comments

In this chapter, the main findings are addressed, while the detailed results can be found in each paper.

- **Paper 1: Water Dynamics in Glass Ionomer Cements**

  The work presented in this paper highlighted the importance of understanding the dynamics of the liquids in order to better understand the properties of the GIC. This understanding was fundamental to the QENS analysis in Paper 2.

  I observed that the aqueous PAA solution has two very distinct water populations. While in Liquid Poly one population is bulk-like and the other is bound to the polymer, in Liquid Hema both populations are differently bound. This means that the liquids influence and, to a certain extent, control the hydrogen binding in the GIC.

- **Paper 2: Nanoscale Mobility of Aqueous Polyacrylic Acid in Dental Restorative Cements**

  This paper was the most elaborated and comprehensive study in my Ph.D. thesis. During this study, I familiarized myself with calorimetric analysis and used neutron spectroscopy to disentangle superimposed motions in the free and confined aqueous PAA solution.

  I was able to follow how progressively water binds to the polymer in one sample (Aqua), while in another continuous crosslinking is noticed (Poly). I also identified different amounts of bulk water in the samples after maturation. Even if bulk water binds to the polymer chain, an increase in the amount of structural water is not necessarily observed. Additionally, while progressive water binding due to ageing occurred in the Aqua, clear changes in the material density were observed in the Poly cement. This change in density was interpreted as continuous crosslinking in the material over time. The QENS analysis revealed three distinguishable hydrogen populations in the PAA aqueous solution, which were also visible in both matured GIC. By varying the observation time, i.e. instrument resolution, it was not possible to detect changes in the self-diffusive motions of the GIC between samples aged for 7 or 28 days; only a change in the intensity of the elastic signal was observed. The most noticeable difference between the GIC samples was the dynamics associated to the confined glassy water; i.e. the water eventually just binding to the polymer.

- **Paper 3: Water Mobility in Chalk: A Quasielastic Neutron Scattering Study**

  Although this study was not directly related to the main focus of this thesis, learning how to analyze QENS data was extremely relevant. This should then be considered as an educational study where I familiarized myself with the data analysis and the effects of confinement in the water dynamics.

  In this paper, I analyzed two chalk samples known to have similar pore volumes, but vastly different water uptake. With neutron spectroscopy, I distinguished differences in the water population and changes of the water geometry attributable to the influence of distinct local environment in the samples. I observed that the water mobility is more restricted in the sample that absorbs less water. Furthermore, the hydrophobicity of the surface results in a translational diffusion (D_t), which is faster than bulk water. In conclusion, I was able to show that the hydration in chalk is influenced not only by the pore surface, but also by pore confinement.

- **Paper 4**: **Dynamics of encapsulated Hepatitis B surface Antigen: A combined neutron spectroscopy and thermo-analysis study**

  This was the final data analysis during my Ph.D. period, where the knowledge I acquired from the previous studies was applied to a different system.

  In this study we verified how the dynamics of the Hepatitis B surface antigen is modified under confinement. I analyzed the QENS data and demonstrated that in the ns timescale the vaccine in salt solution is immobilized (or protected) by the inner structure of the mesoporous SBA-15.

All in all, neutron spectroscopy unveiled dynamics of different systems under confinement and was proven a good technique to supplement and deepen the information acquired using calorimetric analysis.

References

(1) Tian, K. V; Yang, B.; Yue, Y.; Bowron, D. T.; Mayers, J.; Donnan, R. S.; Dobó-Nagy, C.; Nicholson, J. W.; Fang, D.-C.; Greer, A. L.; et al. Atomic and Vibrational Origins of Mechanical Toughness in Bioactive Cement during Setting. *Nat. Commun.* **2015**, *6*, 8631.

(2) Lohbauer, U. Dental Glass Ionomer Cements as Permanent Filling Materials? – Properties, Limitations and Future Trends. *Materials.* **2009**, *3* (1), 76–96.

(3) Khan, A. S.; Khalid, H.; Sarfraz, Z.; Khan, M.; Iqbal, J.; Muhammad, N.; Fareed, M. A.; Rehman, I. U. Vibrational Spectroscopy of Selective Dental Restorative Materials. *Appl. Spectrosc. Rev.* **2016**, 1–34.

(4) Khoroushi, M.; Keshani, F. A Review of Glass-Ionomers: From Conventional Glass-Ionomer to Bioactive Glass-Ionomer. *Dent. Res. J.* **2013**, *10* (4), 411–420.

(5) Sidhu, S.; Nicholson, J. A Review of Glass-Ionomer Cements for Clinical Dentistry. *J. Funct. Biomater.* **2016**, *7* (3), 16.

(6) Calixto, R. L.; Tonetto, M. R.; Pinto, S. C. S.; Barros, E. D.; Borges, A. H.; Lima, F. V. P.; de Andrade, M. F.; Bandéca, M. C. Degree of Conversion and Hardness of Two Different Systems of the Vitrebond TM Glass Ionomer Cement Light Cured with Blue LED. *J Contemp Dent Pr.* **2013**, *14* (2), 244–249.

(7) Ngo, H. Glass-Ionomer Cements as Restorative and Preventive Materials. *Dent. Clin. North Am.* **2010**, *54*, 551–563.

(8) Roberts, H.; Berzins, D. Thermal Analysis of Contemporary Glass-Ionomer Restorative Materials. *J. Therm. Anal. Calorim.* **2013**, *115* (3), 2099–2106.

(9) Wilson, A. D.; Kent, B. E. A New Translucent Cement for Dentistry. The Glass Ionomer Cement. *Br. Dent. J.* **1972**, *132* (4), 133–135.

(10) Peutzfeldt, A.; Munksgaard, E. C.; Asmussen, E. *Glasionomercementer*; Academic Books: 2630 Taastrup, 2014.

(11) Wilson, A. D. A Hard Decade's Work: Steps in the Invention of the Glass-Ionomer Cement. *J. Dent. Res.* **1996**, *75* (10), 1723–1727.

(12) Wilson, A. D. Glass-Ionomer Cement Origins, Development and Future. *Clin. Mater.* **1991**, *7* (4), 275–282.

(13) Wilson, A. D. Resin-Modified Glass-Ionomer Cements. *Int. J. Prosthodont.* **1990**, *3* (5), 425–429.

(14) Saito, S.; Tosaki, S.; Hirota, K. *Advances in Glass-Ionomer Cements*; Davidson C.L., M. I. A., Ed.; Quintessence Publishing, 1999.

(15) McCabe, J. F. Resin-Modified Glass-Ionomers. *Biomaterials* **1998**, *19* (6), 521–527.

(16) Wan, A. C. A.; Yap, A. U. J.; Hastings, G. W. Acid-Base Complex Reactions in Resin-Modified and Conventional Glass Ionomer Cements. *J. Biomed. Mater. Res.* **1999**, *48* (5),

700–704.

(17) Berzins, D. W.; Abey, S.; Costache, M. C.; Wilkie, C. A.; Roberts, H. W. Resin-Modified Glass-Ionomer Setting Reaction Competition. *J. Dent. Res.* **2010**, *89* (1), 82–86.

(18) Villat, C.; Tran, V. X.; Pradelle-Plasse, N.; Ponthiaux, P.; Wenger, F.; Grosgogeat, B.; Colon, P. Impedance Methodology: A New Way to Characterize the Setting Reaction of Dental Cements. *Dent. Mater.* **2010**, *26* (12), 1127–1132.

(19) Roberts, H. W.; Berzins, D. W. Early Reaction Kinetics of Contemporary Glass-Ionomer Restorative Materials. *J. Adhes. Dent.* **2015**, *17* (1), 67–75.

(20) Craig, R. G. *Restorative Dental Materials | Strength Of Materials | Dentistry*, 11th ed.; Mosby: London UK: London UK, 2002.

(21) Wilson, A. D.; Paddon, J. M.; Crisp, S. The Hydration of Dental Cements. *J. Dent. Res.* **1979**, *58* (3), 1065–1071.

(22) Khurshid, Z.; Zafar, M.; Qasim, S.; Shahab, S.; Naseem, M.; AbuReqaiba, A. Advances in Nanotechnology for Restorative Dentistry. *Materials.* **2015**, *8* (2), 717–731.

(23) Barry, T. I.; Clinton, D. J.; Wilson, A. D. The Structure of a Glass-Ionomer Cement and Its Relationship to the Setting Process. *J. Dent. Res.* **1979**, *58* (3), 1072–1079.

(24) Kent, B. E.; Lewis, B. G.; Wilson, A. D. Glass Ionomer Cement Formulations: I. The Preparation of Novel Fluoroaluminosilicate Glasses High in Fluorine. *J. Dent. Res.* **1979**, *58* (6), 1607–1619.

(25) Earl, M. S. A.; Mount, G. J.; Humet, W. R. The Effect of Varnishes and Other Surface Treatments on Water Movement across the Glass Ionomer Cement Surface. II. *Aust. Dent. J.* **1989**, *34* (4), 326–329.

(26) Wilson, A. D.; Nicholson, J. W. *Acid-Base Cements: Their Biomedical and Industrial Applications*; Cambridge, UK: Cambridge University Press, 1993.

(27) Wasson, E. A.; Nicholson, J. W. New Aspects of the Setting of Glass-Ionomer Cements. *J. Dent. Res.* **1993**, *72* (2), 481–483.

(28) Benetti, A. R.; Jacobsen, J.; Lehnhoff, B.; Momsen, N. C. R.; Okhrimenko, D. V.; Telling, M. T. F.; Kardjilov, N.; Strobl, M.; Seydel, T.; Manke, I.; et al. How Mobile Are Protons in the Structure of Dental Glass Ionomer Cements? *Sci. Rep.* **2015**, *5*, 8972.

(29) Singwi, K. S.; Sjölander, A. Diffusive Motions in Water and Cold Neutron Scattering. *Phys. Rev.* **1960**, *119* (3), 863–871.

(30) Bellissent-Funel, M.-C.; Teixeira, J. Dynamics of Water Studied by Inelastic Neutron Scattering. *J. Mol. Struct.* **1991**, *250*, 213–230.

(31) Volino, F.; Dianoux, A. J. Neutron Incoherent Scattering Law for Diffusion in a Potential of Spherical Symmetry: General Formalism and Application to Diffusion inside a Sphere. *Mol. Phys.* **1980**, *41* (2), 271–279.

(32) Bordallo, H. N.; Aldridge, L. P.; Churchman, G. J.; Gates, W. P.; Telling, M. T. F.; Kiefer, K.; Fouquet, P.; Seydel, T.; Kimber, S. A. J. Quasi-Elastic Neutron Scattering Studies on

Clay Interlayer-Space Highlighting the Effect of the Cation in Confined Water Dynamics. *J. Phys. Chem. C* **2008**, *112* (36), 13982–13991.

(33) Russo, D.; Teixeira, J. Mapping Water Dynamics in Defined Local Environment: From Hindered Rotation to Vibrational Modes. *J. Non. Cryst. Solids* **2015**, *407*, 459–464.

(34) Diallo, S. O.; Vlcek, L.; Mamontov, E.; Keum, J. K.; Chen, J.; Hayes, J. S.; Chialvo, A. A. Translational Diffusion of Water inside Hydrophobic Carbon Micropores Studied by Neutron Spectroscopy and Molecular Dynamics Simulation. *Phys. Rev. E* **2015**, *91* (2), 22124.

(35) Cárdenas, G.; Muñoz, C.; Carbacho, H. Thermal Properties and TGA–FTIR Studies of Polyacrylic and Polymethacrylic Acid Doped with Metal Clusters. *Eur. Polym. J.* **2000**, *36* (6), 1091–1099.

(36) Dubinsky, S.; Grader, G. S.; Shter, G. E.; Silverstein, M. S. Thermal Degradation of Poly(acrylic Acid) Containing Copper Nitrate. *Polym. Degrad. Stab.* **2004**, *86* (1), 171–178.

(37) Guan, L.; Xu, H.; Huang, D. Investigation of the Heat Capacity of Poly (Vinyl Methyl Ether)/Water Mixtures Using the Stepscan Method. *Polym. J.* **2010**, *42*, 540–545.

(38) Mochizuki, A.; Ogawa, H.; Nishimori, Y. Water Structure in poly(2-Hydroxyethyl Methacrylate): Effect of Molecular Weight of poly(2-Hydroxyethyl Methacrylate) on Its Property Related to Water. *J. Appl. Polym. Sci.* **2012**, *125* (1), 53–60.

(39) Squires, G. L. *Introduction to the Theort of Thermal Neutron Scattering*, Third Ed.; Cambridge University Press, 1978.

(40) Chudley, C. T.; Elliott, R. J. Neutron Scattering from a Liquid on a Jump Diffusion Model. *Proc. Phys. Soc.* **1961**, *77* (2), 353–361.

(41) Poinsignon, C.; Estrade-Szwarckopf, H.; Conard, J.; Dianoux, A. J. Structure and Dynamics of Intercalated Water in Clay Minerals. *Phys. B Condens. Matter* **1989**, *156–157*, 140–144.

(42) Dianoux, A.; Volino, F.; Hervet, H. Incoherent Scattering Law for Neutron Quasi-Elastic Scattering in Liquid Crystals. *Mol. Phys.* **1975**, *30* (4), 1181–1194.

(43) Singwi, K. S.; Sjölander, A. Diffusive Motions in Water and Cold Neutron Scattering. *Phys. Rev.* **1960**, *119* (3), 863–871.

(44) Chen, S. H.; Liao, C.; Sciortino, F.; Gallo, P.; Tartaglia, P. Model for Single-Particle Dynamics in Supercooled Water. *Phys. Rev. E* **1999**, *59* (6), 6708–6714.

(45) Bordallo, H. N.; Aldridge, L. P.; Desmedt, A. Water Dynamics in Hardened Ordinary Portland Cement Paste or Concrete: From Quasielastic Neutron Scattering. *J. Phys. Chem. B* **2006**, *110* (36), 17966–17976.

(46) Copley, J. R. D. *Dynamics and Neutron Scattering, NCNR Neutron Spectroscopy and Neutron Physics Summer Schools*; 2009.

(47) Schober, H. *Neutron Applications in Earth, Energy and Environmental Sciences*; Springer Berlin Heidelberg, 2009.

(48) Yu, D.; Mole, R. A.; Kearley, G. J. Performance Test on PELICAN – a Multi-Purpose Time of Flight Cold Neutron Spectrometer. *EPJ Web Conf.* **2015**, *83*, 3019.

(49) Jurányi, F.; Janssen, S.; Mesot, J.; Holitzner, L.; Kägi, C.; Tuth, R.; Bürge, R.; Christensen, M.; Wilmer, D.; Hempelmann, R. The New Mica Monochromator for the Time-of-Flight Spectrometer FOCUS at SINQ. *Chem. Phys.* **2003**, *292* (2–3), 495–499.

(50) Frick, B.; Mamontov, E.; van Eijck, L.; Seydel, T. Recent Backscattering Instrument Developments at the ILL and SNS. *Zeitschrift für Phys. Chemie* **2010**, *224* (1–2), 33–60.

(51) Mamontov, E.; Zamponi, M.; Hammons, S.; Keener, W. S.; Hagen, M.; Herwig, K. W. BASIS: A New Backscattering Spectrometer at the SNS. *Neutron News* **2008**, *19* (3), 22–24.

(52) Pereira, L. C.; Nunes, M. C. P.; Dibb, R. G. P.; Powers, J. M.; Roulet, J.-F.; Navarro, M. F. D. L. Mechanical Properties and Bond Strength of Glass-Ionomer Cements. *J. Adhes. Dent.* **2002**, *4* (1), 73–80.

(53) Dassault Systèmes BIOVIA, Material Studio. Dassault Systèmes: San Diego 2015.

(54) Plimpton, S. Fast Parallel Algorithms for Short – Range Molecular Dynamics. *J. Comput. Phys.* **1995**, *117* (1), 1–19.

(55) Dinur, U.; Hagler, A. T. New Approaches to Empirical Force Fields. *Rev. Comput. Chem.* **1991**, *2*, 99–164.

Chapter 5 Papers

Paper 1

Eur. Phys. J. Special Topics **225**, 773–777 (2016)

DOI: 10.1140/epjst/e2015-50287-3

THE EUROPEAN PHYSICAL JOURNAL SPECIAL TOPICS

Regular Article

Water dynamics in glass ionomer cements

M.C. Berg[1,2], J. Jacobsen[1,2], N.C.R. Momsen[1], A.R. Benetti[3], M.T.F. Telling[4,5], T. Seydel[6], and H.N. Bordallo[1,2,a]

[1] The Niels Bohr Institute, University of Copenhagen, 2100 Copenhagen, Denmark
[2] European Spallation Source ESS ERIC, PO Box 176, 22100 Lund, Sweden
[3] Department of Odontology, Faculty of Health and Medical Sciences, University of Copenhagen, 2200 Copenhagen, Denmark
[4] ISIS Facility, Rutherford Appleton Laboratory, Chilton, Oxon OX11 0QX, UK
[5] Department of Materials, University of Oxford, Parks Road, Oxford, UK
[6] Institut Max von Laue – Paul Langevin, CS 20156, 38042 Grenoble, France

Received 20 October 2015 / Received in final form 2 May 2016
Published online 15 July 2016

Abstract. Glass ionomer cements (GIC) are an alternative for preventive dentistry. However, these dental cements are complex systems where important motions related to the different states of the hydrogen atoms evolve in a confined porous structure. In this paper, we studied the water dynamics of two different liquids used to prepare either conventional or resin-modified glass ionomer cement. By combining thermal analysis with neutron scattering data we were able to relate the water structure in the liquids to the materials properties.

1 Introduction

The incorporation of a resin component to conventional glass ionomer cements (CGIC) is one strategy used to strengthen such material. Resin-modified glass ionomer cements (RMGIC) have longer working time, improved aesthetics, a rapid initial setting and enhanced initial strength when compared to CGIC [1–3]. However, in RMGIC the inclusion of the resin component makes the setting reaction more complex. In this material both (i) an acid-base reaction between the glass particles and the polyacid solution and (ii) a polymerization reaction of the resin monomers (i.e. hydrophylic methacrylates) induced by photo-initiation occur. Since a percentage of the water in RMGIC is replaced by resin monomers (in variable amounts depending on the commercial product), the initial setting is due to the rapidly occurring polymer chain propagation as a result of the polymerization reaction [1]. Consequently, a significant improvement in the strength of RMGIC during the critical first hours of setting is observed when compared to CGIC [2]. It is generally accepted that during the early RMGIC setting process, the acid-base and polymerization reactions compete and inhibit each other [4–6]. Thus, proper polymerization of the resin component is vital to avoid RMGIC setting too slowly and consequently becoming weaker than a CGIC.

[a] e-mail: bordallo@nbi.ku.dk

To fully understand these limitations, there is a clear need to understand proton mobility within CGIC and RMGIC.

In this work we aimed to better understand the dynamics of the water contained in the different liquids used to prepare the GIC. Neutron scattering was deemed desirable since the neutron is not only supremely sensitive to proton mobility but also is able to penetrate deeply into the cement material without perturbing its chemical make up. In addition, the high incoherent scattering cross section of the hydrogen atom makes incoherent inelastic neutron scattering ideal for measuring the dynamics, and consequently hydrogen bond formation, of liquid mixtures. Indeed, when combined with thermal analysis, proton dynamics can be directly linked to liquid crystallisation [7].

We compared the thermal behaviour of two commercial liquids provided by Voco GmbH (Germany). One contains an aqueous solution of polyacrylic acid (hereafter referred to as Liquid Poly) and the other a polyacrylic acid aqueous solution containing different methacrylates, mainly 2-hydroxyethyl methacrylate (hereafter referred to as Liquid Hema). In the later case the methacrylates partly replace the water. The first solution is used to prepare a CGIC (Ionofil Molar AC, hereafter referred to as Poly), while the second is used to prepare a RMGIC (Ionolux AC, hereafter referred to as Hema). Both GIC powders contain irregular particles of fluoroaluminosilicate glass. In the present study, we have also related the thermal behaviour of the liquids to the formation of hydrogen bonds in both cements during the first 24 hours of setting.

2 Experimental details

2.1 Differential scanning calorimetry

The phase transitions of water in Liquid Poly and Liquid Hema were measured by means of differential scanning calorimetry (DSC) using a DSC 214 Polyma from Netzsch. The experimental conditions were: N_2-atmosphere (40 ml/min), heating (cooling) rates of 10, 5 and 2 K/min. The samples weights were approx. 20 mg. These measurements were performed between 40°C (313 K) and −180°C (93 K) in an aluminium closed crucible. An empty crucible was also measured and used for instrument correction.

After first cooling at 10 K/min, the sample was kept at the lowest temperature for 5 minutes and then heated up to 40°C. Reproducibility of the process was verified after having kept the sample at 40°C for 5 minutes and then cooling it again using the same rate. For each different temperature rate, the same procedure was followed. The data was processed using the software provided by Netzsch.

2.2 Quasi-elastic neutron scattering

For all samples proton mobility was investigated using quasi-elastic neutron scattering (QENS) by means of the elastic fixed window (EFW) method. Here we evaluate the evolution of only those neutrons scattered elastically by the sample as a function of time or temperature. Monitoring the elastic signal as a function of temperature allows us to determine the onset of proton mobility by noting points of inflexion in the elastic scattering response. In contrast, by evaluating the elastic intensity as a function of time it is possible to follow the hydration process, and thus access the rate of hydrogen bond formation [8].

In this paper the first 24 hours of setting for two freshly mixed cements, namely Poly and Hema, were evaluated. The investigated cements were prepared by mixing

GIC powders with their respective liquid according to the manufacture's recommendation (Voco GmbH, Germany) using a mechanical agitator (CapMix Capsule Mixing Device, 3 M ESPE AG, Germany) for 10 seconds. The Hema was light activated according to the manufacture's recommendation using a lamp (bluephase, Ivoclar Vivadent) emitting 950 $\mathrm{mW/cm^2}$. Preparation of the cements was carried out at room temperature. The final mass for the Poly material was 1.77 g and for the Hema 2.17 g.

The mobility of the hydrogen in both Liquid Poly and Liquid Hema was measured between 2 and 310 K with data collected upon heating. The data was normalised to the response observed at the lowest temperature. The liquids used to prepare the cements were also measured as provided by the manufacture without modification or light activation.

The time evolution of immobile protons that developed during the cements hydration process was obtained using the following equation:

$$\mathrm{IHI} = \frac{\text{elastic intensity of the hydrating cement}}{\text{total intensity of the liquid at 2 K}}. \tag{1}$$

By noting the total intensity from each liquid at the lowest temperature, we account for the incoherent signal from all hydrogen atoms that dominates the scattering signal.

All samples were wrapped in aluminium foil and mounted in a flat aluminium sample holder sealed with Indium wire. In the case of the hydration measurements, the mounted samples were placed in the instrument approximately 15 minutes after the start of the mixture and were followed for 24 hours. The measurements were performed at the Institut Laue-Langevin in Grenoble (France) using the IN10 spectrometer with an elastic energy resolution of 1 μeV at full width half maximum. IN10 allows us to observe length scales between 5 to 25 Å.

3 Results and discussion

It is well known that the calorimetric behaviour of water in the liquid-state in aqueous solutions is different from that of bulk water below 273 K. This is due to a disturbance of the hydrogen bonds, which affects the structure of water molecules. In this sense we define freezing water as the water that freezes between 190 K and 273 K, while non-freezing water may never crystallise even at nitrogen temperature; the lowest temperature detectable in DSC measurements [9].

Regarding our DSC data presented in Fig. 1, we observe an asymmetric endothermic peak and a markedly different response between the two liquids. For the Liquid Poly, Fig. 1(a), the melting temperature for the water in a heating interval of 2 K/min is $T_m = 273$ K, marked by an arrow, thus indicating the presence of bulk-like water. Moreover, we also observe a glass transition around $T_g = 250$ K, indicated by (*), implying the presence of a second water population whose mobility is partially hindered by the interactions with the polyacrylic acid. In contrast, using the same heating rate, the water melting temperature for Liquid Hema, Fig. 1(b), is lower than that of bulk water and equals to 267 K. This is due to the formation of stronger hydrogen bonds between the water and the methacrylate chains. In addition, a second crystallisation is observed in this liquid around $T_c = 210$ K on cooling at 10 K/min as indicated by (**). This can be attributed to a different population of bound water [7].

In general the strength of the interaction between water molecules in aqueous solutions can be related to the water concentration [7,10]. In this study we have not examined this effect. However, by comparing the EFW scans of the liquids, Fig. 1(c) and (d), we observe that more mobile hydrogens are seen in the Liquid Poly, as indicated by the horizontal line. Moreover, the higher onset temperature of proton

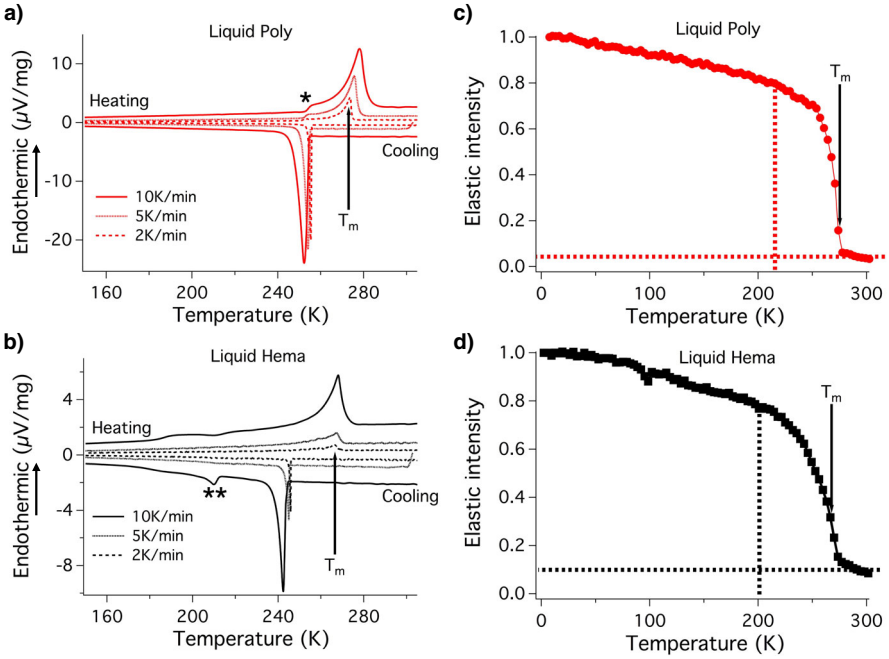

Fig. 1. Comparison of the DSC curves for different rates of cooling and heating (a, b) and EFW scans on heating (c, d) collected at IN10 at the ILL for Liquid Poly and Liquid Hema. The melting temperature, T_m, is defined by the maximum on the peak of the endothermic process (heating) in the DSC curves and indicated by an arrow in all plots. On heating, the glass transition temperature, T_g, is indicated by the (*) in the Liquid Poly (a). The second crystallisation temperature in the Liquid Hema, T_c, is indicated by (**) in the exothermic process (cooling) in (b). Differences in water populations can be linked to the temperatures at which the proton dynamics starts and to the amount of mobile proton in the EFW scans (c, d). This is illustrated by the vertical and horizontal dashed lines, respectively. The EFW data has been normalised to the scattering intensity measured at their respective lowest temperatures.

mobility, determined by the inflexion point in the elastic scattering response and indicated by the dashed vertical line, in this liquid agrees with the existence of a bulk-like water population as indicated by the DSC data.

Examining the evolution of the immobile protons, over the first 4 hours of hydration in the cements (Fig. 2), we note that the IHI is higher for the Hema and remains almost constant through the measured 24 hours. This can be explained by the fast polymerisation and related to the improved early strength of RMGIC, as previously reported [2,11].

We hereby conclude the following:

1) From our DSC data, we observe that both liquids have two very distinct water populations. However, while in Liquid Poly one population is bulk-like and the other is bound, in Liquid Hema both populations are differently bound.
2) The reduced amount of mobile water at room temperature in the Liquid Hema, which is considered to limit the progression of the acid-base reaction [4,5,12] and hinder the development of the microstructure [6] in RMGIC, is confirmed by our EFW data.
3) The distinct dynamics of the liquids used to prepare the Poly and Hema, influence and to a certain extend control, hydrogen binding to the GIC structure.

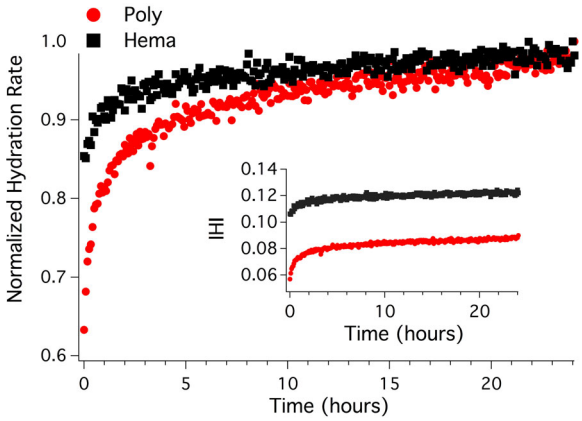

Fig. 2. Normalised time evolution of immobile protons (IHI) on the ns-time scale, determined using the equation given in the text. The data was collected using IN10 at the ILL. The inset shows the same data on a not normalised scale. The results suggest that during the first 24 h of setting the protons bind faster to the microstructure of the Hema material.

The authors acknowledge support from the Carlsbergfondets (grant number Ref.: 2013_01_0589). The authors also acknowledge the support of the Institut Laue-Langevin by providing the neutron research facilities used in this work. JJ, NCRM and HNB work at the ILL was financed by CoNeXT and Danscatt. MCB, JJ and HNB research was partially funded by the European Spallation Source. The investigated samples were donated by VOCO GmbH.

References

1. A.D. Wilson, Int. J. Prosthodont. **3**, 425 (1990)
2. S. Saito, S. Tosaki, K. Hirota, *Advances in Glass Ionomer Cements*, edited by C.L. Davidson, I.A. Mjör (Quintessence Publishing Co, Berlin, Germany, 1999), p. 15
3. J. McCabe, Biomaterials **19**, 521 (1998)
4. A.C.A. Wan, A.U.J. Yap, G.W. Hastings, J. Biomed. Mater. Res. (Appl. Biomater.) **48**, 700 (1999)
5. D.W. Berzins, S Abey, M.C. Costache, C.A. Wilkie, H.W. Roberts, J. Dent. Res. **89**, 82 (2010)
6. C. Villat, X.V. Tran, N. Pradelle-Plasse, P. Ponthiaux, F. Wenger, B. Grosgogeat, P. Colon, Dent. Mater. **26**, 1127 (2010)
7. A. Mochizuki, H. Ogawa, Y. Nishimori, J. Appl. Polymer Sci. **125**, 53 (2012)
8. A.R. Benetti, J. Jacobsen, B. Lehnhoff, N.C.R. Momsen, D.V. Okhrimenko, M.T.F. Telling, N. Kardjilov, M. Strobl, T. Seydel, I. Manke, H.N. Bordallo, Scientific Reports **5**, 8972 (2015)
9. L. Guan, H. Xu, D. Huang, Nature: Polymer. J. **42**, 540 (2010)
10. R.G.M. van der Sman, J. Phys. Chem. B **117**, 16303 (2013)
11. A. Yamazaki, Y. Hibino, M. Honda, Y. Nagasawa, Y. Hasegawa, J. Omatsu, T. Yamaga, H. Nakajima, Dent. Mater. J. **26**, 708 (2007)
12. H.M. Anstice, J.W. Nicholson, J. Mater. Sci. Mater. Med. **5**, 299 (1994)

Paper 2

Nanoscale Mobility of Aqueous Polyacrylic Acid in Dental Restorative Cements

Journal:	*ACS Applied Materials & Interfaces*
Manuscript ID	am-2017-157353
Manuscript Type:	Article
Date Submitted by the Author:	16-Oct-2017
Complete List of Authors:	Berg, Marcella; University of Copenhagen, Niels Bohr Institute Benetti, Ana ; University of Copenhagen, Faculty of Health and Medical Sciences Telling, Mark; Rutherford Appleton Lab, ISIS Seydel, Tilo ; Institut Max von Laue - Paul Langevin Yu, Dehong; ANSTO, Daemen, Luke; Oak Ridge National Laboratory, Chemical and Engineering Materials Division Bordallo, Heloisa; University of Copenhagen, Niels Bohr Institute

Nanoscale Mobility of Aqueous Polyacrylic Acid in Dental Restorative Cements

Marcella C. Berg[1,2,], Ana R. Benetti[3], Mark T. F. Telling[4,5], Tilo Seydel[6], Dehong Yu[7], Luke L. Daemen[8], Heloisa N. Bordallo[1,2]*

[1] The Niels Bohr Institute, University of Copenhagen, DK-2100, Copenhagen, Denmark

[2] European Spallation Source ESS ERIC, PO Box 176, SE-221 00 Lund, Sweden

[3] Department of Odontology, Faculty of Health and Medical Sciences, University of Copenhagen, DK-2200, Copenhagen, Denmark

[4] ISIS Facility, Rutherford Appleton Laboratory, Chilton, Oxon, UK OX11 0QX

[5] Department of Materials, University of Oxford, Parks Road, Oxford, UK

[6] Institut Max von Laue - Paul Langevin, CS 20156, F-38042 Grenoble, France

[7] Australian Nuclear Science and Technology Organisation, New Illawarra Road, Lucas Heights, NSW

[8] Oak Ridge National Laboratory, P.O. Box 2008, Oak Ridge, TN 37831

ABSTRACT: Hydrogen dynamics in a time range from hundreds of femtoseconds (fs) to nanoseconds (ns) can be directly analyzed using neutron spectroscopy, where information on the inelastic and quasi-elastic scattering, hereafter INS and QENS, can be obtained. In this study, we applied these techniques to understand how the nanoscale mobility of the aqueous solution of polyacrylic acid (PAA) used in conventional Glass Ionomer Cements (GIC) changes under confinement. Combining the spectroscopic analysis with calorimetric results we were able to separate distinct motions within the liquid and in the GIC's. The QENS analysis revealed that the self diffusion translational motion identified in the liquid is also visible in the GIC. However, as a result of the formation of the cement matrix and its setting, both translational diffusion and residence time differed from the PAA solution. When comparing the local diffusion obtained for the selected GIC, the only noticeable difference was observed for the slow dynamics associated to the polymer chain. Additionally, over short-term ageing, progressive water binding to the polymer chain occurred in one of the investigated GIC. Finally, a considerable change in the density of the GIC without progressive water binding indicates an increased polymer crosslinking. Taken together, our results suggest that accurate and deep understanding of polymer-water binding, polymer crosslinking as well as material density changes occurring during the maturation process GIC are necessary for development of advanced dental restorative materials.

INTRODUCTION

Oral health is an integrated part of the general public health, and does not only affect the quality of life, but also the social healthcare systems through related economic costs. Despite great progress globally in oral health related issues, dental caries is still one of the major problems, affecting 60-90% of schoolchildren and the vast majority of adults. Therefore, dental restoration takes one of the most significant shares in the health care cost in industrialized countries[1,2]. Consequently, developing and improving dental restorative materials is an important matter.

The dental restorative materials known as Glass ionomer cements (GIC) are acid-based and widely recognized as being biologically active [3–5]. The base for GIC is a fluoroaluminosilicate glass powder, formed by different cations, such as calcium, strontium and aluminium, and the aqueous solution contains a polyacrylic acid (PAA). PAAs are weak polyelectrolytes with many carboxyl groups that partially dissociate in water, leaving the PAA main-chain with negative charges and ionized hydrogen ions in the bulk solution. PAA is an essential industrial polymer also used as emulsifying agents, in pharmaceuticals, in cosmetics and in paints and have a particularly important role in dispersants[6]. Previous studies on liquid PAA solutions used in preparation of GIC showed two distinct water populations, one unbound and in its native bulk water state (hereafter called 'bulk water') and the other more hindered by the PAA (hereafter called 'glassy water')[7]. It is well known that these distinct populations influence the properties of the GIC[3]. During the first steps of the GIC setting process, water will act as the reaction medium where the leached cations cross-link with the PAA, thus forming the polyacrylate matrix. The conformation and flexibility of the polyelectrolyte chain will in turn govern the degree of crosslinking in the polyacrylate matrix thus influencing the cement properties. Furthermore, the water also hydrates the siliceous hydrogel and the metal polyacrylate salt, which both become an essential part of the cement structure[8]. If water is lost from the cement by desiccation upon setting, the cement-forming reaction will either stop or be retarded. On the contrary, in the first 3 to 6 minutes of the cement's hydration, initial contact with water can be damaging, and therefore the surface of the restoration is kept protected[3,9]. During maturation, bulk water can remain unbound, become bound or part of the cement structure. Loosely water associated with the hydration shell of the cation-polyacrylate[10,11] or confined in the cement pores[12] will hereafter be referred to as 'confined bulk'. Water tightly bound in hydration regions around the polymer chain will be referred to as

'confined glassy water'. Structural water are evidenced by the vibrational motions of those water molecules undulating about their equilibrium positions[11]. The loosely bound water is liable to change which can lead to cracks in the material[13,14], unless the cement is in an 80% relative humidity[11]. In addition, with ageing, the pore structure changes[12], and as such it is believed that the ratio of confined water to loosely bound water increases[10,14–16].

Previous work using Fourier Transform Infrared Spectroscopy [3,17] and neutron scattering[4,12] have indeed confirmed the presence of distinct water populations in GIC. As in other systems, these populations are expected to demonstrate distinct dynamic behaviours due to the complex GIC pore structure.[18,19] However, to date, information on how the water dynamics change under confinement and throughout GIC maturation is scarce[20–24]. For example, information is still lacking regarding how much liquid remains in its original bulk-state and how the pore structure evolution changes the dynamics of the aqueous solution, in turn influencing the cement properties. To deepen this understanding, we used neutron spectroscopy to probe the dynamics of free and confined PAA solution in two selected GIC from the same manufacturer but at different ages of maturation. One cement, herein referred to as Poly, was mixed mechanically using an aqueous PAA solution[21], and the other, where the glass powder contains vacuum dried PAA (referred to as Aqua cement), was hand-mixed with distilled water[23]. These particular GICs were selected for this study since each has a distinctive mechanical property, where based on flexural strength measurements the Aqua cement shows lower strength that is constant over the whole maturation period[12]. Furthermore, based on previous knowledge, the protons bind differently to the microstructure[12]; which to a certain extent is controlled by the aqueous PAA solution[7].

By understanding the different types of confinement that both the water and the pure PAA undergo over time, our results give unique insight into the distribution of the aqueous populations in GIC cements. To this end, neutron spectroscopy was desirable, since the neutron is not only able to penetrate deep into matter without altering composition, but also the high incoherent scattering cross section of the hydrogen atom makes the technique ideal for extracting proton self correlations (dynamics) in hydrogenous materials. Consequently, insight into the hydrogen bond network (i.e. the hydrogen bond between the base glass-silicate and the aqueous PAA) and distinct states of water can be gleaned. In particular, incoherent neutron scattering provides geometrical information on the molecular

confinement of diffusive motions. Furthermore, by combining thermal analysis and neutron spectroscopy, a better understanding of the hydrogen-bond network formation was achieved, in addition to how density changes influence this unique type of cement.

EXPERIMENTAL METHODS

Cement sample preparation: The two GICs described in the introduction were prepared following the manufacturer specification. The Poly cement (Ionofil Molar AC, Voco GmbH, Germany) in a encapsulated version was prepared by mixing the GIC powder with its respective liquid in a powder-to-liquid ratio of 3.7:1. Using a mechanical RotoMix Capsule Mixing Device (3M ESPE AG, Germany), the mixture was agitated for 10 seconds followed by 3 seconds centrifugation. The Aqua cement (Aqua Ionofil Plus, Voco GmbH, Germany) was hand-mixed using a powder-to-liquid weight ratio of 5.6:1. Preparation was carried out at room temperature.

For the neutron experiments, 1 g of material was used. After mixing, the samples were uniformly distributed in individual aluminium foil envelopes, and mounted in a flat aluminium sample holder. The sample holders were sealed securely using Indium wire and aged for either 7 or 28 days at body temperature (37 °C). For the thermal analysis, triplicates of each sample were prepared following the procedure described above. On the day of the thermal analysis measurement, the sample holders were opened; one of the aged triplicates gently ground using a pestle and mortar, with the 2 other samples resealed. This procedure was repeated before each thermogravimetric analysis and Fourier transform infrared spectroscopy (TGA-FTIR) experiment, the samples weights being approx. 40 mg.

Thermogravimetric Analysis and Fourier Transform Infrared Spectroscopy (TGA-FTIR): TGA is a method by which changes in the mass of a material is followed as a function of temperature. When coupled to the FTIR device, a technique used to obtain an infrared spectrum of sample absorption, any decomposing components in the material can be identified. For this work, TGA-FTIR was used to characterize different proton states, i.e. bulk-like vs. bound water, and thus indirectly obtain an estimate of the amount of structural hydrogen; information crucial for the analysis of the neutron data.

All samples were measured using a TG 209 F1 Libra PERSEUS from Netzsch coupled to a Fourier Transform Infrared Spectrometer from Bruker Optics. The experimental conditions were: N_2 atmosphere (20 mL/min), heating rate of 10 K/min. The measurements were performed on the ground cement samples (described above) between 20 °C (293 K) and 900 °C (1173 K) in a standard Al_2O_3 crucible. An empty crucible was also measured for instrument correction. The data was processed using the software provided by Netzsch. A FTIR spectrum of the developed gases was recorded for every 3 °C during the entire measurement. From the collected FTIR data, a selection of spectrums at temperatures of interest, based on the TGA data, was further analyzed. All 7 day-old materials were measured on the same day. Due to the reproducibility of this triplicate data, only one 28 day-old sample was measured. The powder samples were studied as provided by the manufacturer.

Neutron spectroscopy: Neutron spectroscopy is the ideal tool to study the structure and dynamics of water in confinement, since the translational frequencies will change with the local water structure. Furthermore, since the interatomic forces determine a particular phonon mode, the strength of the H-bond interaction can be obtained.

In neutron spectroscopy the scattering function, $S(Q,\omega)$, is the observable quantity of interest, where Q is the magnitude of the scattering wave vector and ω is the energy transfer. $S(Q,\omega)$ can be divided into three spectroscopic components: the elastic scattering function, $S_E(Q,\omega=0)$, which is related to the thermal fluctuations of the atoms around their equilibrium position, the quasi-elastic signal, $S_{QE}(Q,\omega\approx 0)$, that describes molecular translation and rotational motions, and the inelastic signal, $S_{IN}(Q,|\omega| >> 0)$, that probes phonon and molecular vibrations. In hierarchical porous structures such as in the cements studied here, proton nanoscale mobility occur over different timescales. Consequently, investigations using different neutron spectrometers, which probe different temporal ranges, are necessary. As a result, this study was carried out using, four neutron instruments: VISION (giving information on molecular vibrations occurring over a broad energy range from 1 to 1000 meV corresponding to the femtosecond (fs domain), PELICAN (covering the high picosecond range, ~ 600 ps, and allowing for observation of fast localized motions of the confined or chemically bound hydrogen atoms), IRIS (covering the low picosecond, ~ 200 ps, time scale thus allowing localized dynamics to be followed) and IN16B (covering slower dynamics in the nanosecond regime; i.e ~ 5 ns). Each instrument is described in detail below.

The vibrational spectrometer VISION, located at Spallation Neutron Source, Oak Ridge, USA follows those neutrons that scatter inelastically from a sample with an exchange of energy, $S_{IN}(Q, \omega > 0)$, that is equal to vibrational states. The scattered neutrons lose energy by exciting the vibrational modes of the scatterer, consequently the spectrum is obtained in the neutron energy loss side (Stokes side). As the intensity of an Inelastic Neutron Scattering (INS) band is proportional to the Debye–Waller factor, whose magnitude is in part determined by the thermal motion of the molecule, this factor can be reduced by measuring INS spectra at 10 K. Furthermore, the INS spectrum is directly proportional to the phonon density of states and scattering lengths of the associated atoms. Because selection rules are not involved, INS measures all the modes simultaneously. Thurs, by comparing the INS spectrum obtained for each sample at different maturation periods, it is possible to probe changes in the vibrational response as a function of cement age. Such information gives insight into the molecular properties and development of the hydrogen bond network.

In addition to the INS data, confined and chemically bound hydrogen dynamics in the dental cements studied in this work were probed via a comprehensive investigation of the QENS signal, $S_{QE}(Q, \omega \approx 0)$. To obtain such information, QENS measurements were performed over a broad temporal range by combining data obtained using PELICAN, IRIS and IN16B.

The time-of-flight cold neutron spectrometer, PELICAN, located at Australian Nuclear Science and Technology Organisation (ANSTO) in Australia, provides an elastic energy resolution, ΔE, corresponding to an upper experimental observation time of ~ 600 ps and covers an angular scattering range of 22° < 2θ < 119°. In this study an incident wavelength of λ = 6.0 Å was chosen, corresponding to ΔE = 63 μeV at full width at half maximum (FWHM), in order to probe the fast dynamics mostly due to the loosely bound water either in the PAA or confined in the cement structure.

The backscattering spectrometer IRIS, located at the ISIS Facility in the UK, provides an elastic energy resolution of 17.5 μeV at FWHM, corresponding to an upper experimental observation time of ~200 ps, achieved by neutrons scattered with λ = 6.7 Å. This resolution is constant over the entire Q-range of 0.501 to 1.960 $Å^{-1}$ (angular scattering range of 25° < 2θ < 160°). IRIS probes the intermediate dynamics of the loosely and tightly bound water.

Finally, the high-energy-resolution analyser (ΔE = 0.75 μeV at FWHM, λ = 6.3 Å) provided by the backscattering spectrometer IN16B, located at ILL in France Grenoble, allows an upper experimental observation time of ~ 5 ns. This time window corresponds mostly to the slower polymer-related motion. The instrument resolution is constant over the entire Q-range of 0.190 to 1.895 $Å^{-1}$ which corresponds to an angular scattering range of 11° < 2θ < 142°. IN16B was used here with its standard Si(111) monochromator and analyzer crystal setup[25].

For all experiments, the angle between the plane of the sample and the incident neutron beam was 135°. Consequently, the last detectors were self-shielded by the edge of the sample holder and thus discarded from analysis. The data was reduced using the software packages LAMP[26] (PELICAN and IN16B) and MANTID[27] (IRIS) and analysed using DAVE[28].

Insight into the diffusive behaviour of confined liquid in Aqua and Poly cements: Based on the analysis of the QENS response, the nanoscale diffusion of the confined water molecules was analyzed by fitting the quasielastic (QE) signal using a sum of Lorentzian functions, $L_n(\Gamma,\omega)$, as follows:

$$S(Q,\omega) = DWF\left[(A_0(Q)\delta(\omega) + \left(1\text{-}A_0(Q)\ \sum_{i=1}^{n} L_n(\Gamma,\omega)\right) \otimes R(Q,\omega)\right] + B(Q) \qquad (1)$$

where DWF represents the Debye Waller factor. $A_0(Q)$, defined as the Elastic Incoherent Structure Factor (EISF), describes the time averaged spatial distribution of all scattering centers. The term $\sum_{i=1}^{n} L_n(\Gamma,\omega)$ indicates the sum of Lorentzians representing the broadened energy distribution that results from neutron-nucleus collisions, corresponding to the population statistics of distinct relaxation processes. $R(Q,\omega)$ denotes the resolution function of the instrument. $B(Q)$ represents a background term, including those dynamics that are too fast for to be seen by the temporal range probed by the instrument Finally $\delta(\omega)$, is a delta function describing those particles seen as immobile .

Additional information can be extracted by looking at the ratio between the elastic intensity and the total intensity from both the elastic (E) and quasielastic (QE) signal, referred to as the EISF[29].

$$A_0(Q) = EISF = \frac{E}{QE+E} \qquad (2)$$

The EISF expresses the probability that a particle can be found in the same volume of space after a time interval, t, (corresponding to the instrument resolution) has passed. It can therefore be used to determine the geometry of the motion of a molecule or molecular specie in a molecule. Since the type of confinement influences the local geometry of the molecule, the evolution of the EISF can shed light on the specific type of local restrictions on the molecule[29–31].

The behavior of the extracted half width at half maximum (Γ, HWMH), of the QE signal, was modeled as a function of Q using the expression for the random-jump-diffusion[32]:

$$\Gamma(\mathrm{Q}) = \frac{DQ^2}{1+DQ^2\tau_0}, \quad (3)$$

where τ_0 corresponds to the residence time and D is the translational diffusion constant given in terms of the mean jump length $< l >_{AV}$ as:

$$D = \frac{<l>_{AV}}{6\tau_0} \quad (4)$$

RESULTS AND DISCUSSION

Decomposition temperatures of the different proton states in GIC powders and cements through Thermal Gravimetric Analysis and Infrared Spectroscopy (TGA-FTIR)

By examining the TGA curves from the cements and respective powders, we observe a mass loss at around 100 ºC in the cements that is absent in the powders, see Fig.1. Based on the equivalent FTIR data (Fig. 2a), where the spectrum at 110 ºC corresponds to the inflection point from the derivative of the TGA curves (see inset Fig. 1), we can conclude that this mass loss is due to water evaporation; peaks characteristic of O-H stretching being observed at 1300-2200 cm^{-1} and 3400-3900 cm^{-1}. This finding agrees with previous results[33,34]. In addition, as the Aqua cement ages, and the amount of unbound water decreases, we can confirm the retarded maturation and development of porosity in the Aqua material compared to the Poly[10,12]. Furthermore, with ageing, the inflection point of the evaporation process, indicated by an arrow in Fig. 1, shifts to a higher temperature in the 28 day-old Aqua cement, when the mass losses for both materials becomes similar.

Now we turn to the analysis of the powders. On further heating two decomposition steps are observed. The first mass drop in the TGA, Fig. 1, emerges at around 225 ºC, which is related to the initial decarboxylation decomposition of the PAA[15,33,34]. This is further inferred by observation of the C=O stretch, the typical and major ketone absorption peak at 1700 cm^{-1} and the C-H vibration at 1180 cm^{-1}, as well as residual water and Si(Al)O-H stretching (3200-3600 cm^{-1} and 3850 cm^{-1}), indicated by (*) in Fig. 2 (b,c)[35]. The second mass drop, detected at about 425 ºC, can be related to further degradation of the polymer[36]. This is confirmed by the FTIR data, where C-H stretching (2960 cm^{-1}) is observed. The same absorption peaks are observed, but with a factor 10 smaller intensity in the Poly Powder, thus confirming the incorporation of lyophilized PAA in the powder.

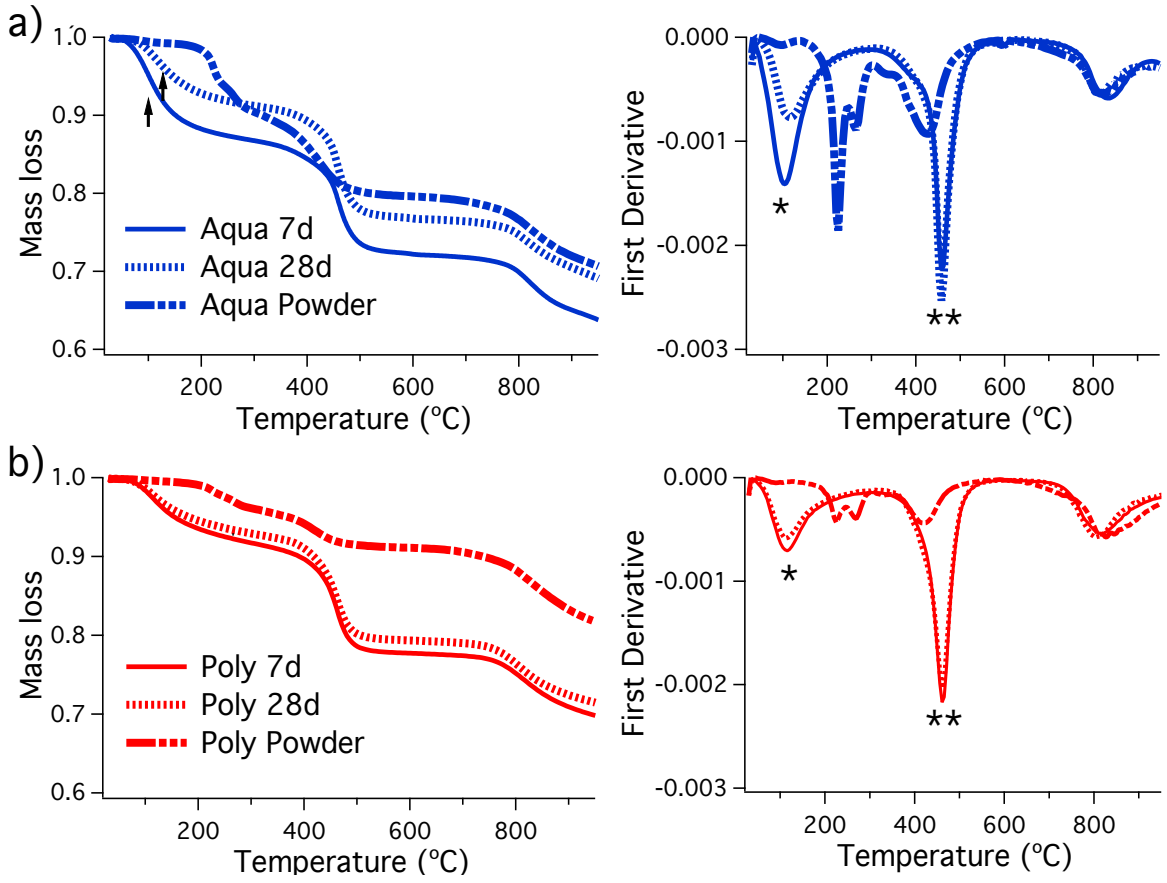

Figure 1: The left side shows the TGA curves for the Aqua (a) and Poly (b) cements aged for 7 and 28 days and their respective powders. The right side of the figure shows the first derivative of the TGA curves revealing the largest mass losses. The arrows in the left side in (a) indicate the shift of the evaporation process in the Aqua cement. The (*) in the right side indicate the inflection point for the evaporation of the loosely bound and unbound water. In contrast, (**) indicates the tightly bound water. Considering the ageing process of the Aqua cement (a) we observe a decrease in the

amount of the loosely bound and unbound water and a slight increase in the amount of the tightly bound water. In contrast for the Poly cement, only a slight decrease in the amount of loosely bound and unbound water is detected.

Focusing again on the cements, a second mass loss, comparable across all samples is observed at around 450ºC (see Table S1 in the supplementary information). Moreover, from the FTIR results we observe that the same vibrational modes described above for the powders were also detected in the cements. However, the decomposition of the PAA occurs at higher temperatures, indicating much stronger chemical bonds. Indeed, it is well known that complexed PAA salts, i.e aluminum polyacrylate and strontium polyacrylate, has increased stability and decomposes between 425 and 520 ºC[15]. Interestingly, in the Aqua Cement we detect an increase in the amount of tightly bound water evaporating from the sample, highlighted by the (**) in Fig. 1. This observation suggests a more pronounced change in the hydrogen bond network over time, not necessarily caused by an increase in the amount of structural water. For further insight in the local structure of the GIC, a detailed analysis of the QENS spectra was performed.

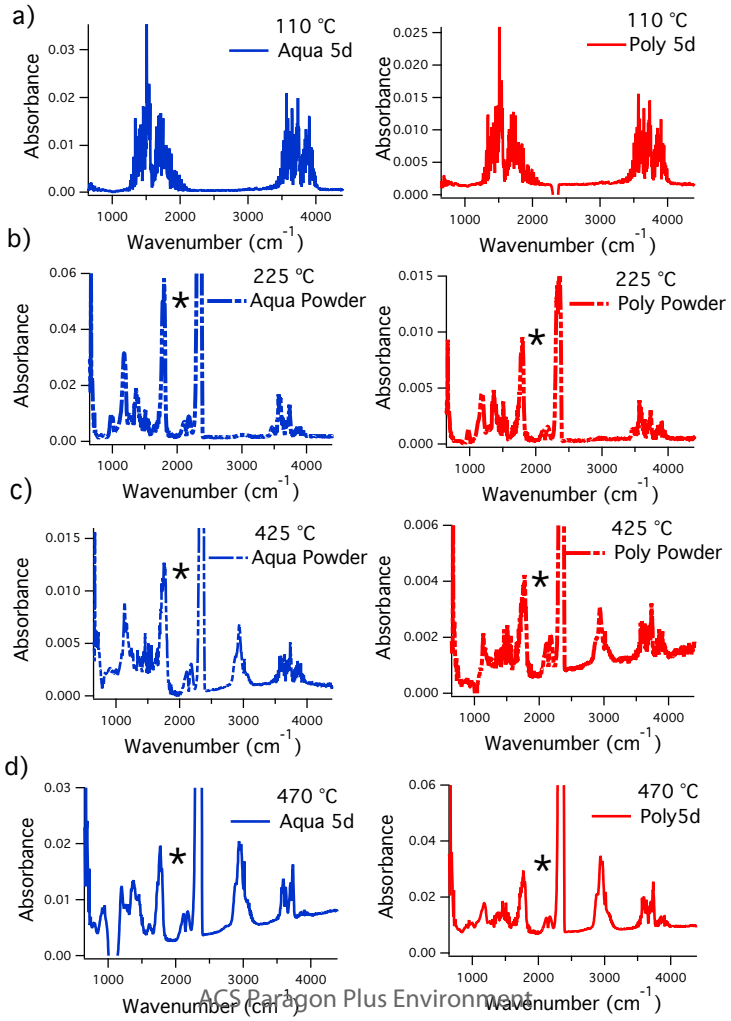

Figure 2: FTIR spectra for the Aqua (left side in blue) and Poly (right side in red) cements aged for 7 days and their respective powders. The various temperatures correspond to the decomposition stages as observed in the TGA under controlled heating. Note that the strongest absorption peak, resulting from carbon dioxide stretching at 2500 cm^{-1}, is mostly due to the decomposition of the carboxylic acids in the GIC.[37] Spectra for the 28 day-old samples show similar behaviour.

Finally, the mass loss around 825 ºC in all samples comes from the decomposition of the unreacted glass silicate, as confirmed by the observation of Si-O-Si stretching vibrations at around 1000 cm^{-1} as shown in the SI and indicated by (**).

Dynamical behavior of bulk and glassy water in liquid PAA as analyzed by neutron spectroscopy

In order to fully understand how the dynamics of the bulk water and the aqueous PAA solution is modified when confined in the Aqua and Poly cements, respectively, we first considered the dynamics of the bulk liquids. The results are shown in Figure 3 and listed in Table 1.

Even though bulk water and its dynamics under confinement has been widely studied using neutron spectroscopy[4,7,12,18,19,30,32,38–41], QENS spectra of water at body temperature were measured using the IRIS spectrometer to facilitate the analysis of our data. The data was fitted using Equation (1) to one single Lorentzian, and the extracted HWHM (Γ_{water}) was modelled as a function of Q^2 to the random jump-diffusion model given in Equation (3). Our analysis give a $D_{\text{water at 310K}} = 2.9 \cdot 10^{-9}\ m^2/s$ and $\tau_0 = 0.35$ ps.

In contrast, there is incomplete information about the dynamics of aqueous PAA solutions[42,43]. In the particular case of the PAA studied here, it is known that gel-like polymeric networks are formed[34], and that, from a combination of neutron spectroscopy and calorimetric analysis[7], two water populations were distinguished; one that resembles bulk water and the other suggesting glassy behavior originating from regions of hydration around the polymer chain. Therefore the QENS signal of PAA collected at PELICAN at body temperature was fitted to Equation 1 using two Lorentzians; one representing the dominating faster bulk water motion (hereafter referred to by its HWHM, Γ_{bulk}) and

the second representing a population with a more hindered diffusion representative of glassy water behavior (hereafter referred to by its HWHM, Γ_{glassy}). All parameters were unconstrained during the fitting procedure. The resulting HWHM was also analysed using Equation 3. From this analysis we observe that Γ_{bulk} ($D_{bulk} = 2.9 \cdot 10^{-9}\ m^2/s$ and $\tau_0 = 0.37$ ps) and Γ_{water} are the same. We interpret this as mean that the faster bulk water motion and its residence time (reflected on the value of τ_0) are not modified in the aqueous PAA solution. However, the diffusion coefficient for Γ_{glassy} ($D_{glassy} = 1.7 \cdot 10^{-9}\ m^2/s$ and $\tau_0 = 9.9$ ps) is 30 times slower than Γ_{bulk}. Further confirmation of the coexistence of bulk and constrained regions of polymer hydration in the PAA network is realized by looking at the EISF. Here we clearly see that the water states probed by PELICAN, Fig. 3(a), fit very well with the modified analytical EISF model for confined water; namely diffusion of a point particle inside a sphere[44]. This model is given by Equation 5 below:

$$A_0(Q) = p + (1-p)\left(\frac{\frac{3\sin Qd}{Qd^2} - \frac{3\cos Qd}{Qd}}{Qd}\right)^2 \quad (5)$$

where d is the radius of the idealised spherical confinement, and p accounts for the immobile fraction of the protons

To better map the more hindered water population that gives rise to $\Gamma_{glassy,}$ as well as to verify the existence of possible slower dynamics in the PAA[45], QENS measurements were performed using the backscattering spectrometers IRIS and IN16B. By analysing the IRIS signal using the approach described above, and using a fixed value of Γ_{bulk}, the two water populations detected during the PELICAN measurements were observed. However, on IRIS, with its narrower energy resolution, the slower Γ_{glassy} motion was seen to be the dominating spectral component; Γ_{bulk} contributing to a slightly higher offset in the 'background'. From the evolution of the EISF, Fig. 3 (b), also fitted to Equation 5, we observe a lower immobile fraction of the protons, p (see Table 1). This corroborates the idea that distinct water states have different mobility. Furthermore, by imposing the linewidth of Γ_{glassy} while fitting the IN16B data to Equation 1, a new, slower dynamic process, not discernible in the calorimetric analysis, was detected. Considering the diffusion value for this motion ($0.6 \cdot 10^{-10}\ m^2/s$, which is ~ 10 times slower than D_{glassy}, we attribute it to the PAA itself[45], hereafter named by its HWHM as Γ_{PAA}. Moreover, unlike IRIS and PELICAN, the

evolution of the EISF for Γ_{PAA} cannot be fitted using the confined water model, Fig. 3(c), indicating changes in the structuring of the hydrogen network[46]. This point will be further discussed later.

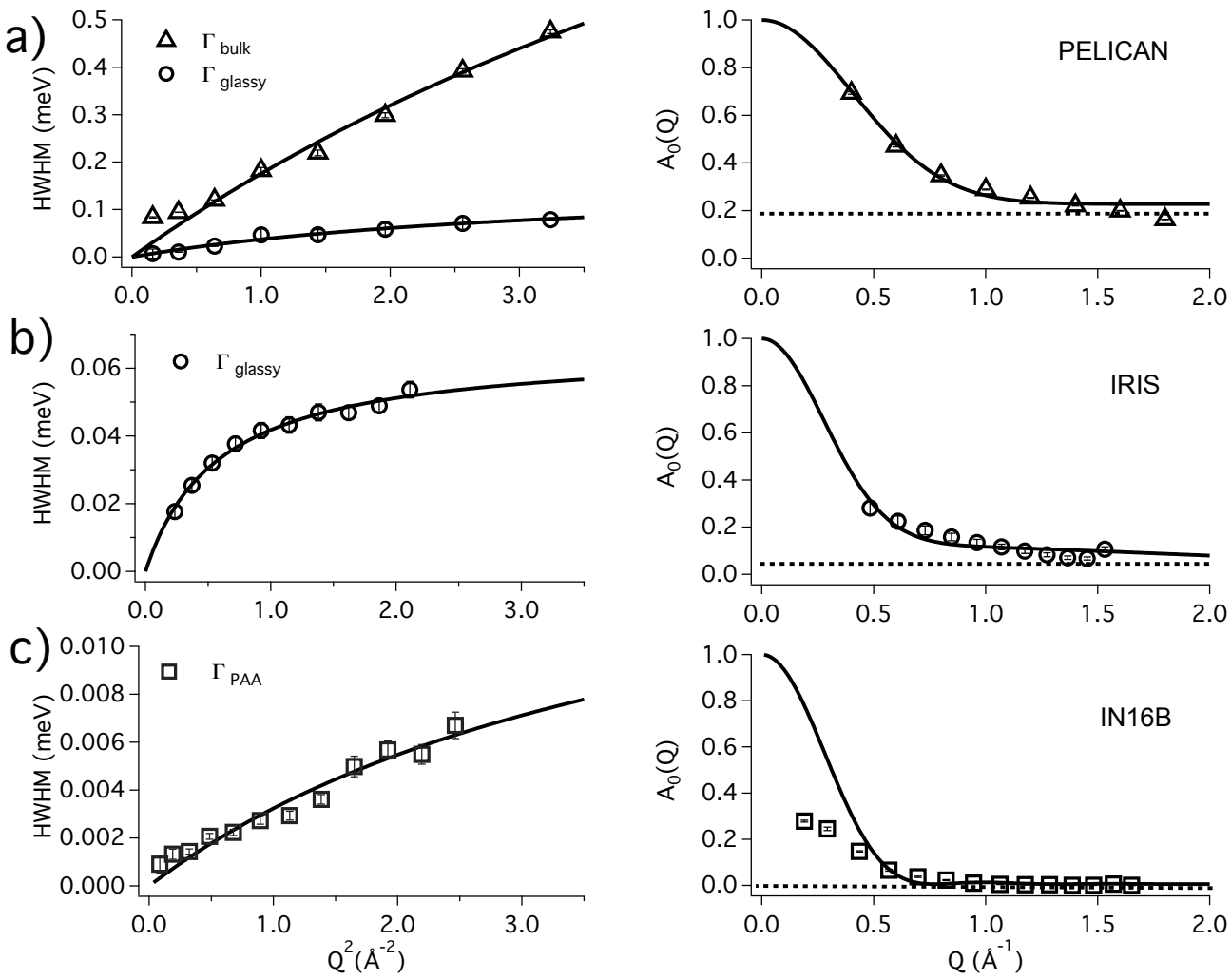

Figure 3: Left side: Evolution of the HWHM for Γ_{bulk}, Γ_{glassy} and Γ_{PAA} as a function of Q^2 obtained for the PAA sample and modelled using theory developed to describe random jump diffusion. Right side: The EISF plotted as a function of Q and obtained from the analysis of the quasielastic spectra. The solid lines were obtained by fitting the data to Equation 5, while the horizontal dotted line are representative of the amount of immobile protons (p) in the PAA as

seen using spectrometers with differing energy resolutions. The results were extracted from the data collected at 310 K using (a) PELICAN, (b) IRIS and (c) IN16B. Note that the simple diffusion of a point particle inside a sphere[44] does not fit the IN16B data well.

Table 1: Parameters D_t and τ_0 obtained from fitting, as a function of Q^2 , the HWHM's describing the different water populations observed in PAA; namely Γ_{bulk}, Γ_{glassy} and Γ_{PAA}. The data was modelled using an analytical function developed to describe random jump diffusion. The parameters d and p were obtained, for each spectrometer, by fitting the Q dependence of the EISF to the diffusion of a point particle inside a sphere[44] model. The parameters were extracted from data collected at 310K. For comparison, the values obtained for bulk water measured at 310K using the IRIS spectrometer, and also modelled using the random jump diffusion form, are given.

Spectrometer	Population	D_t ($10^{-9}m^2/s$)	τ_0 (ps)	p (%)	d (Å)
PELICAN	Γ_{bulk}	2.96±0.4	0.37±0.02	0.22±0.02	3.6±0.2
IRIS	Γ_{glassy}	1.72±0.1	9.9±0.3	0.11±0.01	5.3±0.3
IN16B	Γ_{PAA}	0.06±0.009	30±10	Not possible to fit with a simple model	Not possible to fit with a simple model
IRIS (bulk water)	Γ_{water}	2.96 ±0.04	0.35±0.02	-	-

Modification to the dynamical behavior of water in aqueous PAA when confined in the GIC as observed by neutron spectroscopy

From the TGA analysis we know that a fraction of the bulk water, Γ_{bulk}, remains in both cements even after 28 days of aging. Therefore, to analyse the QENS signal observed in the cements when using PELICAN and IRIS, two Lorentzians were used but with the HWHM describing the bulk water, Γ_{bulk}, fixed. All other parameters were unconstrained. The results obtained for the Poly and Aqua samples using PELICAN and IRIS are shown in Figures 4 and 5 and listed in Table 2.

In the timescale covered by PELICAN, and for all cement samples (Figure 4, Table 2) independent of cement sample and age, the dominating signal comes from a water state for which the diffusion coefficient was found to be in the order of ~ 2 times higher than Γ_{glassy}, an order of ~ 2 times slower than Γ_{bulk} and with a residence time ~ 40 times higher than Γ_{glassy}. Based on this observation, plus the fact that a fraction of the liquid used in preparing the GIC either

remains in its bulk state, is confined in the small cement pores[12] or is assigned to cationic water[47,48], we conclude that the slower motion (hereafter referred to after its HWHM, $\boldsymbol{\Gamma_{bulk\text{-}confined}}$), is ascribed to confinement. In contrast, the broader component describes unreacted liquid, $\boldsymbol{\Gamma_{bulk}}$. Surprisingly, even though the strength and porosity of the cement samples differ[12], in the ps timescale the dynamical behavior of the water in aqueous PAA when confined in the GIC, $\boldsymbol{\Gamma_{bulk\text{-}confined}}$, does not. Indeed, independent of the cement's age, the diffusion coefficient is approximately the same for all cements; $D_{\,\mathrm{bulk-confined}} = 1.2 \cdot 10^{-10}\ \mathrm{m^2/s}$ and $\tau_{0-\mathrm{bulk-confined}} = 0.5$ ps. However, the amount of hydrogen in the form of unbound water does vary, as depicted by the EISF. Once again, the evolution of the EISF as a function of Q is well described using the modified analytical form for confined proton moblity[29], with the immobile fractions, p (p_{AA}=0.22, p_{Poly7}=0.82, p_{Aqua7}=0.78, p_{Poly28}=0.86 and p_{Aqua28}=0.82), being consistent with TGA measurements, see Tables S1 and S3. This finding confirms the highest water content to be in the 7 days old Aqua material while the lowest is seen to be in the 28 days old Poly sample. Comparison of the extracted d values, which represents the radius of the idealised spherical confinement, shows d_{PAA}= 3.6 Å ± 0.2 Å, d_{Poly7}=3.4 Å ± 0.1Å and d_{aqua7}=3.3 Å ± 0.1 Å; the average radius for the confined water molecule not differing within error. This result implies that the type of confinement probed on the ps timescale is comparable. If we, however, compare the d values extract for the 28 day-old samples (d_{Poly28}=3.0 Å ± 0.1 and d_{Aqua28}=3.3Å ± 0.1Å) with the 7 day-old samples, we observe a slight decrease in the radius of confinement for the Poly cement, see Fig 4. This change is not observed in the Aqua cement and indicates a change of local geometry in the Poly material between 7 and 28 days. Previous work on these specific cements showed a change in mechanical strength over the same time period for the Poly cement only.

Table 2: Parameters D_t and τ_0 obtained from fitting, as a function of Q^2, the evolution of the HWHM describing the different water populations in the GIC samples as a function of ageing; namely Γ_{bulk}, $\Gamma_{bulk\text{-}confined}$ and $\Gamma_{glassy\text{-}confined}$. The data was modelled using the analytical function developed to describe random jump diffusion. The parameters d and p were as obtained, for each of the selected spectrometer, by fitting from the fit of the Q dependence of the EISF as a function of Q using to the diffusion of a point particle inside a sphere[44] model. The parameters were extracted from the

data collected using the spectrometers PELICAN, IRIS and IN16B at 310K. Bulk water is known to exist in these samples and therefore its contribution was considered during the fitting procedure.

Sample	Spectrometer	Populations	D_t ($10^{-9}m^2/s$)	τ_0 (ps)	p (%)	d (Å)
Poly	PELICAN	Γ_{bulk}	2.96 (fixed)	0.37 (fixed)	-	-
		$\Gamma_{bulk\text{-}confined}$	1.12±0.12	1.56±0.4	0.82±0.001 at 7 d	3.53±0.057 at 7 d
					0.86±0.003 at 28 d	3.02±0.1 at 28 d
	IRIS	$\Gamma_{glassy\text{-}confined}$	0.97±0.1	15.9±1.1	0.73±0.008 at 7 d	3.37±0.18 at 7 d
					0.75±0.006 at 28 d	3.39±0.16 at 28 d
Aqua	PELICAN	Γ_{bulk}	2.96 (fixed)	0.37 (fixed)	-	-
		$\Gamma_{bulk\text{-}confined}$	1.09±0.17	2.12±0.1	0.78±0.001 at 7 d	3.3±0.03 at 7 d
					0.83±0.002 at 28 d	3.3±0.07 at 28 d
	IRIS	$\Gamma_{glassy\text{-}confined}$	0.12±0.013	64.8±6.8	0.72±0.006 at 7 d	3.16±0.16 at 7 d
					0.79±0.006 at 28 d	3.58±0.18 at 28 d

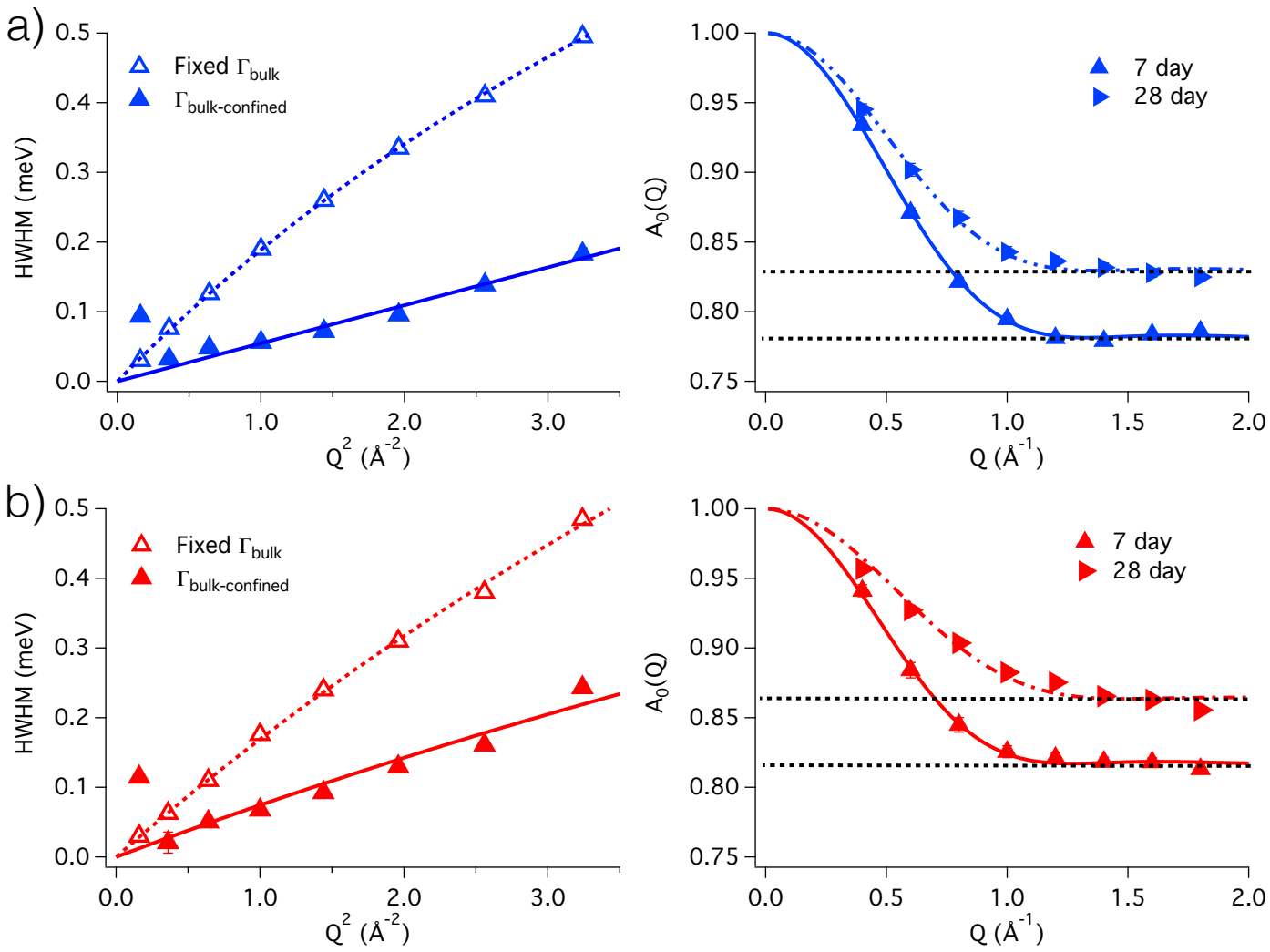

Figure 4: Left side: Evolution of the HWHM for Γ_{bulk} and $\Gamma_{bulk\text{-}confined}$, as a function of Q^2 , or GIC samples Aqua (top, in blue) and Poly (bottom, in red), The data, from which the line widths were extracted, was collected using PELICAN. The linewidth responses were analysed using a random jump diffusion model. Note: The HWHM does not change as a function of ageing. Right side: The EISF, as a function of Q, obtained from the analysis of the quasielastic spectra for GIC samples aged at 7 and 28 days. The solid and dashed lines were obtained using the model described by Equation 5. The horizontal dotted line is a guide to the eye to allow the fraction of immobile protons (p) in the cements to be ascertained as a function of ageing.

To further understand how the polymeric-water network is changing during the reaction with the silicate glass, as observed using the intermediate timescale covered by IRIS (~200 ps), we followed the same procedure described above. The results are summarized in Fig. 5 and Table S3. By comparing the diffusion coefficient values obtained for

the Poly cement at different ages ($D_{glassy-confined-poly} = 0.99 \cdot 10^{-9}$ m^2/s) to the value for glassy water in the PAA solution ($D_{glassy} = 0.7 \cdot 10^{-9}$ m^2/s), we observe that they are of the same order. We can therefore, conclude that the water molecules that occupy coordination sites around the polymers in the PAA solution do not change their dynamic response when confined. Furthermore, the dramatic increase in the residence time, $\tau_{0\_glassy-confined-Poly} = 27$ ps compared to $\tau_{0\_glassy} = 3.9$ ps, clearly indicates a strong deviation from the ideal water structure. On the other hand, for the Aqua cement at different stages of maturation, a diffusion coefficient ($D_{glassy-confined-Aqua} = 0.12 \cdot 10^{-9}$ m^2/s with $\tau_{0-glassy-confined-Aqua} = 65$ ps) was obtained. This D value is ~ 10 times slower than D_{glassy} and ~ 6 times slower $D_{glassy-confined-Poly}$, with a much longer residence time, τ_0. We therefore conclude that the polymeric-water network in glassy water is more hindered in the Aqua sample. Previous observation[12] showed that the hydrogen protons bind faster to the microstructure of the Aqua cement on the intermediate timescale of ~200 ps, which was earlier connected to different proton (population) mobility in the Aqua Cement.

Additionally, the diffusion of a point particle inside a sphere[44] model cannot fully describe the evolution of the EISF over the full Q-range for the cement samples. The effective EISF deviates at around Q= 0.8 Å^{-1} and decreases again at Q=1.4 Å^{-1}, indicating a restricted rotational diffusion[18], see (*) and (**) in Fig. 5 . Furthermore we note that changes in the immobility fraction p of the EISF are more evident for the Aqua cement upon ageing, which is in full agreement with the TGA measurements and the QENS spectra from PELICAN. On the IRIS timescale there is a slight change in the radius of the confinement, reflected by the EISF, for the differently aged Aqua cements. In contrast, for the Poly cement this happens on the PELICAN timescale.

Knowing that for PAA that water gets trapped in the polymer, we interpret our IRIS results as probing exactly this phenomenon, showing more confinement on the Aqua cement.

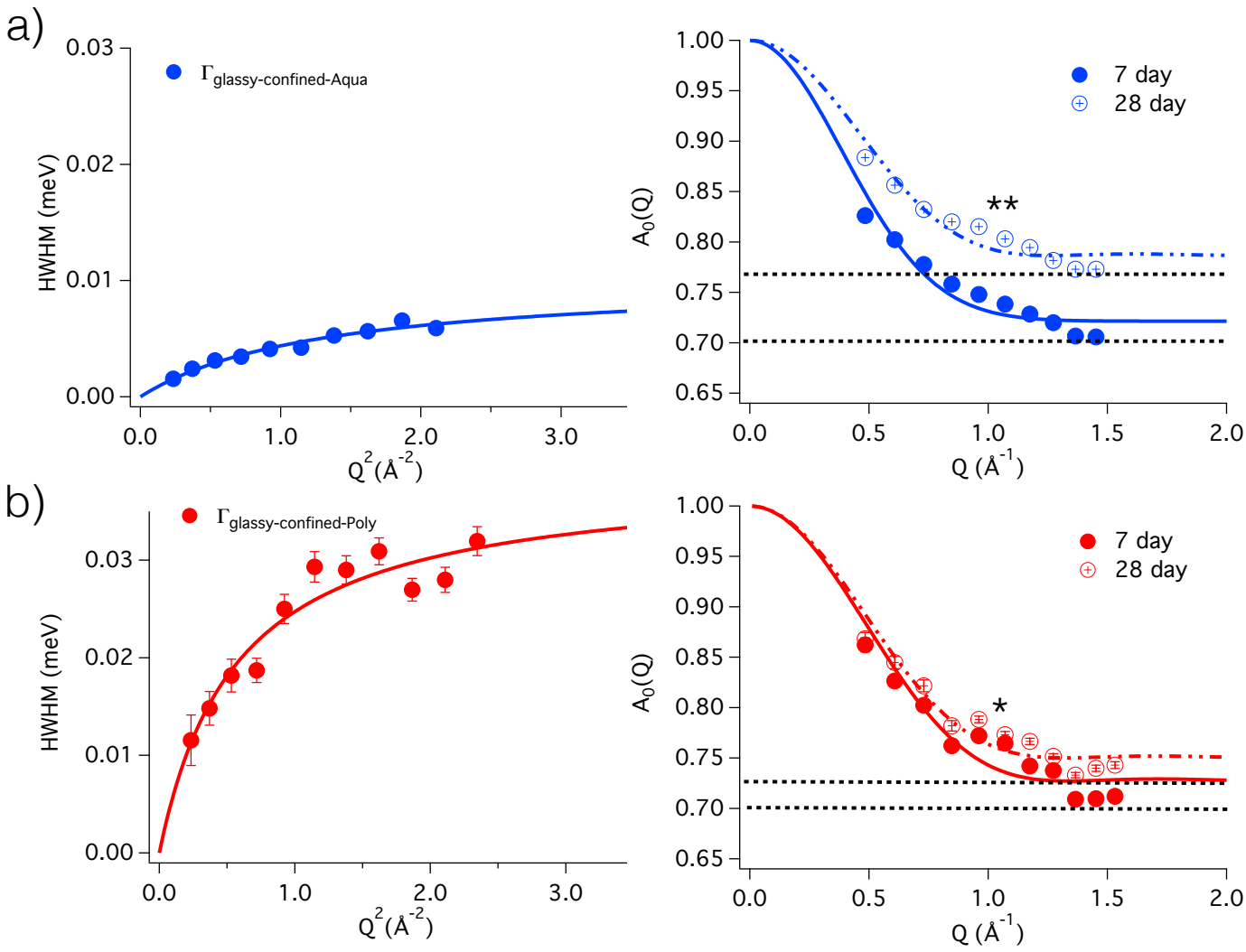

Figure 5: Left side: Evolution of the HWHM for $\Gamma_{glassy\text{-}confined}$ as a function of Q^2 obtained for the GIC samples, Aqua (top, in blue) and Poly (bottom, in red), modelled using a random jump diffusion model. Note: The HWHM does not change as a function of ageing. Right side: The EISF as a function of Q obtained from the analysis of the quasielastic spectra for GIC samples aged at 7 and 28 days. The solid and dashed lines were obtained using Equation 5. The horizontal dotted lines are a guide to the eye to enable the percentages of immobile protons (p) in the cements to be ascertained and as a function of ageing. Here (*) and (**) show where the data deviates from the modified confined water model for, Poly cement and Aqua cement, respectively. The data was collected using IRIS.

Modification to the dynamical behavior of the polymer in PAA when confined in the GIC as analyzed by neutron spectroscopy

When analysing dynamics on the ns timescale (IN16B) the motions from Γ_{bulk}, $\Gamma_{bulk\text{-}confined}$ and $\Gamma_{glassy\text{-}confined}$ contribute to a 'background' intensity and therefore only one Lorentzian was needed to model the data. The variation in the HWHM as a function of Q cannot be satisfactorily describe using the random jump diffusion model (Equation 5) but it is in good agreement with the Chudley-Elliott (Equation 6) model[49], specifically in the high Q limit:

$$\Gamma(Q) = \frac{1}{\tau_0}\left(1 - \frac{\sin(Ql\sin\theta)}{Ql\sin\theta}\right) \quad (6)$$

where τ_0 is the residence time and l the jump length.

Although, for small Q values the evolution of HWHM as function of Q tends to the random jump model, Equation 3, the Chudley-Elliott model gives the best fit when $Q > 0.5$ Å^{-1}. Independent of the modelling, the extracted HWHM is very similar between both cements types, with the mobile population diffusing at a rate similar to as Γ_{PAA}, see Table 1. As a result, we can conclude that the PAA motion is hindered by a geometrical confinement from changes in the chemical bonding, i.e polysalt formation in the cement. This population is hereafter named $\Gamma_{PAA\text{-}confined}$ and is illustrated in Fig. 6 and Table S4. Such changes and confinement can be interpreted as follows; taking the formation of the aluminum poly salts as an example, by mixing PAA, aluminum silicate glass and water, some CH-COO$^-$ groups from the PAA will form CH-COO$^-$-Al^{+3} and others will remain free: these can interchange, thus creating a possible hydrogen diffusion in a diffusive landscape[46]. These different hydrogen networks will then have distinct hydrogen bond lifetimes, originating the periodic bumps at $Q^2 = 0.7$ Å^{-2} and 2.2 Å^{-2} seen at the HWHM evolution in the GIC's.

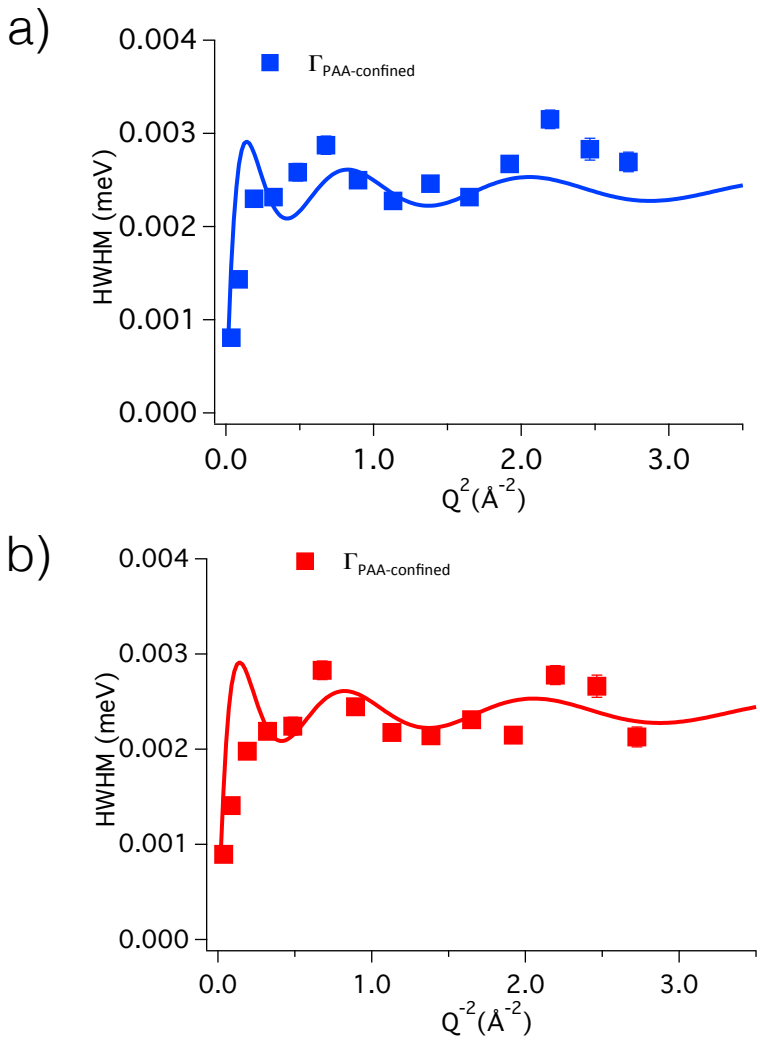

Figure 6: Evolution of the HWHM for $\Gamma_{PAA\text{-}confined}$ as a function of Q^2 as described by the Chudley-Elliott model. The results were extracted from data collected using IN16B for 7 days old Aqua (a, in blue) and 7 days old Poly (b, in red).

Table 3: Parameters l and τ_0 obtained from the data collected at 310K using IN16B. The evolution of the HWHM as a function of Q^2 describing $\Gamma_{PAA\text{-}confined}$ in Poly and Aqua cements aged for 7 days was modelled using the Chudley-Elliott model.

Sample	Spectrometer	Population	**l(Å)**	**τ_0 (ps)**
Poly	IN16B	$\Gamma_{PAA\text{-}confined}$	12 ±0.6	275±9
Aqua	IN16B	$\Gamma_{PAA\text{-}confined}$	12 ±0.6	275±9

Modification of the hydrogen-bond interaction and phonon density in the PAA when confined in the GIC analyzed by neutron spectroscopy at 10K:

Similar for all cement samples the librational modes at 10 meV assigned to confined water (ice like) is observed in the samples. Modes 20 and 40 meV can be assigned to the water in the polymer network. The distortion from the bulk water (ice) modes in the spectrum is more evident in the 28 day-old samples, as the ratio of bulk-water to glassy-water decreases. The first peak that can be fully assigned to the silicate matrix is visible at 130-190 meV and matches well the signal detected by the FTIR (~1000-1500 cm^{-1} or ~125-188 meV) illustrated in Fig. S1, which corresponds to the Si-O-Si stretching vibration from the powder. The small vibration at 210 meV most likely corresponds to the carboxylic acid C=O stretching also detected in the FTIR (~1700 cm^{-1} or ~212 meV). Furthermore, at 370 meV (~2900 cm^{-1}) we observe a C-H stretching coming from the PAA in all samples.

First we notice that the signal to noise ratio is the same in all samples. By comparing the intensity obtained from VISION spectrometer from samples aged during 7 and 28 days, we can see that the largest change in signal occurs in the Poly cement (see Fig 7). The intensity of the signal is directly proportional to the phonon density, which we can interpret as the variation in density over time.

In putting all findings together, we first consider the intensities from the QENS measurements, and notice that signal from the 28 day-old Aqua to be higher than the 7 day-old, thus confirming the TGA findings, which show that the amount of unbound water decreases while the amount of bond water increases. This is however not the case for the Poly cement, that in contrast reveals a bigger change in density over time, based on the intensities from the VISION measurements. This suggests that in the Aqua cement the degree of crosslinking is lower than in the Poly cement, and instead more H-bonds are being formed. In the Poly on the other hand, the crosslinking continues even after 28 days with limited H-bond formation.

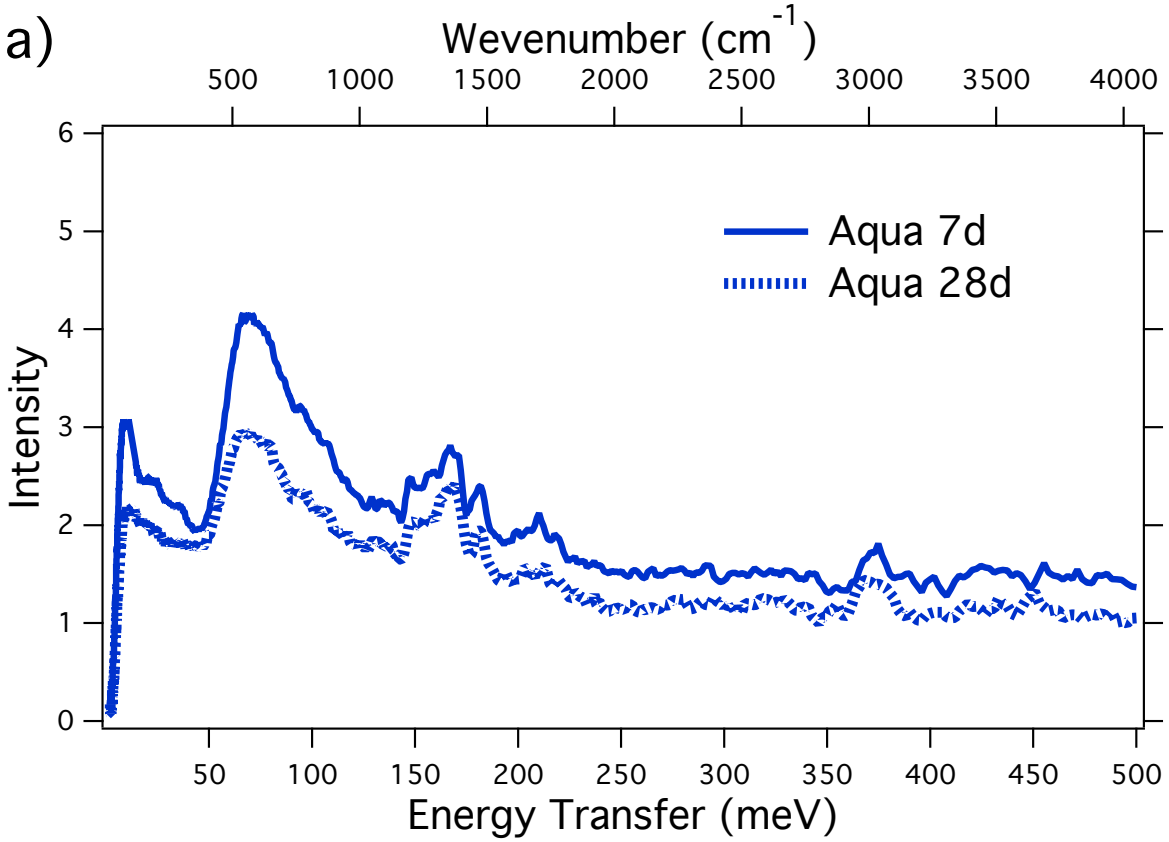
a)
Wevenumber (cm-1)
500 1000 1500 2000 2500 3000 3500 4000
Aqua 7d
Aqua 28d
Intensity
0 1 2 3 4 5 6
50 100 150 200 250 300 350 400 450 500
Energy Transfer (meV)

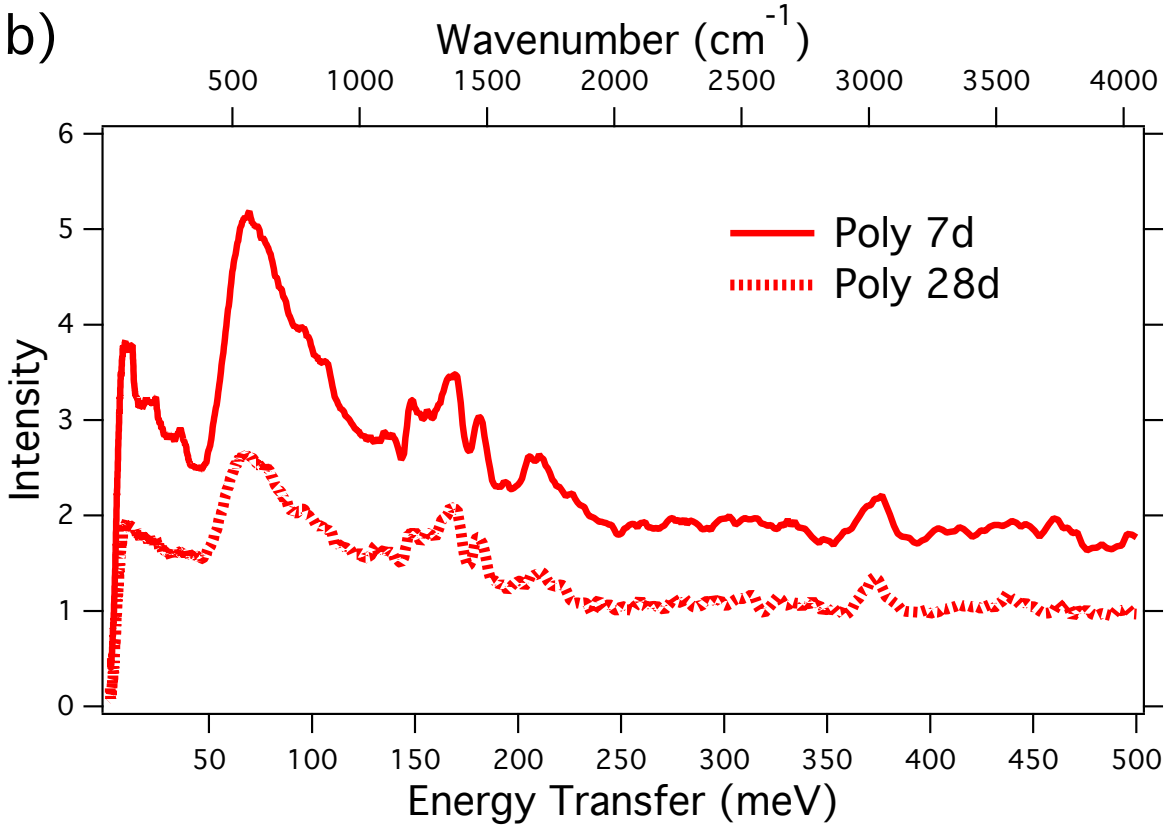
b)
Wavenumber (cm-1)
500 1000 1500 2000 2500 3000 3500 4000
Poly 7d
Poly 28d
Intensity
0 1 2 3 4 5 6
50 100 150 200 250 300 350 400 450 500
Energy Transfer (meV)

Figure 7: Vibrational transition energies obtained using the vibrational spectrometer, VISION, and collected at 10 K. (a) Aqua cement samples (blue) aged for 7 and 28 days and (b) Poly cement samples (red) aged for 7 and 28 days. The intensity of the signal is directly proportional to the phonon density. The peaks are assigned to the librational and vibrational modes of the samples. Bulk water is given in SI for comparison.

CONCLUSION

To date relatively few studies have been carried out on the dynamics of GIC, this one being the first that maps the full hydrogen dynamics in the aqueous PAA solution used in conventional GIC to its behaviour when confined in the cement matrix. In this study, distinct hierarchically superimposed molecular motions within the liquid and in the cements could be separated by combining neutron spectroscopy and calorimetric analysis. Consequently a better understanding of the hydrogen-bond network formation and density changes of this unique type of GIC was achieved.

A key component that influences sample properties is water. Water is necessary for initial setting but also for the maturation, since it hydrates the cement matrix and further allows it to react. While it is known that water binds to the structure during the first steps of the setting[8], there are still some ambiguities regarding water binding during maturation. In this study, we have added to this understanding as follows. From the thermogravimetric method different amounts of bulk water in the samples after maturation were identified. This analysis showed that for these samples, bulk water binds to the polymer chain, while an increase in the amount of structural water is not necessarily observed. However, progressive water binding due to ageing occurred in only one of the GIC, namely the weaker Aqua sample. As the mechanical strength of the Aqua cement does not change with aging in the maturation timeframe studied here[12], we can hypothesize that the progressive water binding does not influence the strength of the material. Clear changes in the material density were only observed in the Poly cement as detected by the INS data. Thus we interpret that the continuous crosslinking on the Poly cement is the main cause for its increase in strength during maturation.

QENS analysis revealed three distinguishable hydrogen populations in the PAA aqueous solution, which were also visible in both GICs. By varying the observation time, it was not possible to detect changes in the self-diffusing motions between samples aged 7 or 28 days; only a change in the intensity of the elastic signal was observed. The residence time in the cement itself differed from that of the PAA solution due to changes in the local environment: the most noticeable difference between the GIC samples being in the dynamics associated to the confined glassy water; the water eventually just binding to the polymer. The QENS analysis revealed that the hydrogen binding varied between the two GIC, thus the shape and structure of the polyelectrolyte chain and the PAA incorporation method, will in turn influence the degree of crosslinking and hydrogen bonding in the PAA matrix and consequently influencing the cement properties. The dynamics of the hydrogen on the PAA itself showed that for both GIC localised diffusivity dominates parts of the spatial range.

To conclude, these results indicate that the advantages of this material can be improved not only by modifying the glass-silicate, particle size and chemical formula, so that its disintegration and binding to tissue is improved. But also that the understanding of polymer-water binding and polymer crosslinking is important in material development as it can share light on material strength and longevity.

AUTHOR INFORMATION

Corresponding Author

* Marcella C. Berg: marcellaberg@nbi.ku.dk to whom correspondence should be addressed.

Author Contributions

MCB, ARB and HNB conceived the project. MCB and ARB prepared the samples and MCB characterized the samples using the TGA/FTIR. MCB, ARB and HNB designed the neutron scattering experiments, and details were discussed a priori with MTFT, DY and TS. MCB, ARB, MTFT, TS, DY, LSD and HNB carried out the neutron experiments. MCB analyzed all data with input from MTFT, TS, LSD, DY, ARB and HNB. MCB, ARB and HNB wrote the paper with input from the co-authors. The manuscript was approved by all coauthors in its final version

Funding Sources

ACKNOWLEDGMENT

The work was funded by the European Spallation Neutron Source, the Niels Bohr Institute and the Danish Agency for Science, Technology and Innovation through DANSCATT. HNB acknowledges support from the CoNext project. MCB and ARB acknowledge the financial supported offered by the ILL to cover their travel expenses.

Supporting Information. Tables with mass losses obtained from the thermal analysis experiments as well as all the coefficients resulting from the quasielastic neutron scattering (QENS) data analysis are supplied as Supporting Information. Supplementary TGA/FTIR figures as well as fits of the QENS spectra are also provided.

REFERENCES

(1) WHO | What Is the Burden of Oral Disease? *WHO* **2010**.

(2) Patel, R. The State of Oral Health in Europe Report Commissioned by the Platform for Better Oral Health in Europe. **2012**.

(3) Sidhu, S.; Nicholson, J. A Review of Glass-Ionomer Cements for Clinical Dentistry. *J. Funct. Biomater.* **2016**, *7* (3), 16.

(4) Tian, K. V; Yang, B.; Yue, Y.; Bowron, D. T.; Mayers, J.; Donnan, R. S.; Dobó-Nagy, C.; Nicholson, J. W.; Fang, D.-C.; Greer, A. L.; et al. Atomic and Vibrational Origins of Mechanical Toughness in Bioactive Cement during Setting. *Nat. Commun.* **2015**, *6*, 8631.

(5) Ngo, H. Glass-Ionomer Cements as Restorative and Preventive Materials. *Dent. Clin. NA* **2010**, *54*, 551–563.

(6) Swift, T.; Swanson, L.; Geoghegan, M.; Rimmer, S. The pH-Responsive Behaviour of Poly(acrylic Acid) in Aqueous Solution Is Dependent on Molar Mass.

(7) Berg, M. C.; Jacobsen, J.; Momsen, N. C. R.; Benetti, A. R.; Telling, M. T. F.; Seydel, T.; Bordallo, H. N. Water Dynamics in Glass Ionomer Cements. *Eur. Phys. J. Spec. Top.* **2016**, *225* (4), 773–777.

(8) Barry, T. I.; Clinton, D. J.; Wilson, A. D. The Structure of a Glass-Io Nomer Cement and Its Relationship to the Setting Process. *J. Dent. Res.* **1979**, *58* (3), 1072–1079.

(9) Earl, M. S. A.; Mount, G. J.; Humet, W. R. The Effect of Varnishes and Other Surface Treatments on Water Movement across the Glass Ionomer Cement Surface. II. *Aust. Dent. J.* **1989**, *34* (4), 326–329.

(10) Lohbauer, U.; Ulrich. Dental Glass Ionomer Cements as Permanent Filling Materials? – Properties, Limitations and Future Trends. *Materials (Basel).* **2009**, *3* (1), 76–96.

(11) Wilson, A. D.; Nicholson, J. W. Water and Acid-Base Cements, 30–55.

(12) Benetti, A. R.; Jacobsen, J.; Lehnhoff, B.; Momsen, N. C. R.; Okhrimenko, D. V.; Telling, M. T. F.; Kardjilov, N.; Strobl, M.; Seydel, T.; Manke, I.; et al. How Mobile Are Protons in the Structure of Dental Glass Ionomer Cements? *Sci. Rep.* **2015**, *5*, 8972.

(13) Wasson, E. A.; Nicholson, J. W. New Aspects of the Setting of Glass-Ionomer Cements. *J. Dent. Res.* **1993**, *72* (2), 481–483.

(14) Nicholson, J. W.; Wilson, A. D. The Effect of Storage in Aqueous Solutions on Glass-Ionomer and Zinc Polycarboxylate Dental Cements. *J. Mater. Sci. Mater. Med.* **2000**, *11* (6), 357–360.

(15) Roberts, H.; Berzins, D. Thermal Analysis of Contemporary Glass-Ionomer Restorative Materials. *J. Therm. Anal. Calorim.* **2013**, *115* (3), 2099–2106.

(16) Characterization of Glass-Ionomer Cements 5. The Effect of the Tartaric Acid Concentration in the Liquid Component. *J. Dent.* **1979**, *7* (4), 304–312.

(17) Tadjiev, D. R.; Hand, R. J. Surface Hydration and Nanoindentation of Silicate Glasses. *J. Non. Cryst. Solids* **2010**, *356* (2), 102–108.

(18) Bordallo, H. N.; Aldridge, L. P.; Desmedt, A. Water Dynamics in Hardened Ordinary Portland Cement Paste or Concrete: From Quasielastic Neutron Scattering. *J. Phys. Chem. B* **2006**, *110* (36), 17966–17976.

(19) Le, P.; Fratini, E.; Ito, K.; Wang, Z.; Mamontov, E.; Baglioni, P.; Chen, S. H. Dynamical Behaviors of Structural, Constrained and Free Water in Calcium- and Magnesium-Silicate-Hydrate Gels. *J. Colloid Interface Sci.* **2016**, *469*, 157–163.

(20) Kent, B. E.; Lewis, B. G.; Wilson, A. D. Glass Ionomer Cement Formulations: I. The Preparation of Novel Fluoroaluminosilicate Glasses High in Fluorine. *J. Dent. Res.* **1979**, *58* (6), 1607–1619.

(21) Wilson, A. D.; Kent, B. E. A New Translucent Cement for Dentistry. The Glass Ionomer Cement. *Br. Dent. J.* **1972**, *132* (4), 133–135.

(22) A D Wilson. Resin-Modified Glass-Ionomer Cements. *Int. J. Prosthodont.* **1990**, *Volume 3* (Issue 5), p425-429.

(23) McLean, J. W.; Wilson, A. D.; Prosser, H. J.; Mondell, J. Development and Use of Water-Hardening Glass-Ionomer Luting Cements. *J. Prosthet. Dent.* **1984**, *52* (2), 175–181.

(24) Wilson, A. D. A Hard Decade's Work: Steps in the Invention of the Glass-Ionomer Cement. *J. Dent. Res.* **1996**, *75* (10), 1723–1727.

(25) B. Frick et al. .224, 33 (2010). *Z.Phys.Chem* **2010**, *224* (33).

(26) LAMP, the Large Array Manipulation Program. http://www.ill.eu/data_treat/ lamp/the-lamp-book/.

(27) Arnold, O. et al. Mantid - Data Analysis and Visualization Package for Neutron Scattering and μSR Experiments. *Nucl. Instr. Meth. Phys. Res A* **2014**, *764*, 156–166.

(28) Azuah, R. T. et al. DAVE: A Comprehensive Software Suite for the Reduction, Visualization, and Analysis of Low Energy Neutron Spectroscopic Data. *J Res Natl Inst Stand Technol.* **2009**, *114*, 341.

(29) Dianoux, A.; Volino, F.; Hervet, H. Incoherent Scattering Law for Neutron Quasi-Elastic Scattering in Liquid Crystals. *Mol. Phys.* **1975**, *8976* (August 2014), 37–41.

(30) Jacobsen, J.; Rodrigues, M. S.; Telling, M. T. F.; Beraldo, A. L.; Santos, S. F.; Aldridge, L. P.; Bordallo, H. N.; Dobbs, R.; Neville, A. M.; Isaia, G. C.; et al. Nano-Scale Hydrogen-Bond Network Improves the Durability of Greener Cements. *Sci. Rep.* **2013**, *3*, 69–76.

(31) Zhang, C.; Arrighi, V.; Gagliardi, S.; McEwen, I. J.; Tanchawanich, J.; Telling, M. T. F.; Zanotti, J.-M. Quasielastic Neutron Scattering Measurements of Fast Process and Methyl Group Dynamics in Glassy Poly(vinyl Acetate). *Chem. Phys.* **2006**, *328* (1–3), 53–63.

(32) Singwi, K. S.; Sjölander, A. Diffusive Motions in Water and Cold Neutron Scattering. *Phys. Rev.* **1960**, *119* (3), 863–871.

(33) Berzins, D. W.; Abey, S.; Costache, M. C.; Wilkie, C. A.; Roberts, H. W. Resin-Modified Glass-Ionomer Setting Reaction Competition. *J. Dent. Res.* **2010**, *89* (1), 82–86.

(34) Roberts, H. W.; Berzins, D. W. Early Reaction Kinetics of Contemporary Glass-Ionomer Restorative Materials. *J. Adhes. Dent.* **2015**, *17* (1), 67–75.

(35) Khan, A. S.; Khalid, H.; Sarfraz, Z.; Khan, M.; Iqbal, J.; Muhammad, N.; Fareed, M. A.; Rehman, I. U. Vibrational Spectroscopy of Selective Dental Restorative Materials. *Appl. Spectrosc. Rev.* **2016**, 1–34.

(36) Cárdenas, G.; Muñoz, C.; Carbacho, H. Thermal Properties and TGA–FTIR Studies of Polyacrylic and Polymethacrylic Acid Doped with Metal Clusters. *Eur. Polym. J.* **2000**, *36* (6), 1091–1099.

(37) Max, J.-J.; Chapados, C. Infrared Spectroscopy of Aqueous Carboxylic Acids: Comparison between Different Acids and Their Salts.

(38) Krishnamurthy, S.; Bansil, R.; Wiafe-Akenten, J. Low-Frequency Raman Spectrum of Supercooled Water. *J. Chem. Phys.* **1983**, *79* (12), 5863.

(39) Cho, M.; Fleming, G. R.; Saito, S.; Ohmine, I.; Stratt, R. M. Instantaneous Normal Mode Analysis of Liquid Water Instantaneous Normal Mode Analysis of Orientational Motions in Liquid Water: Local Structural Effects Instantaneous Normal Mode Analysis of Liquid Water. *J. Chem. Phys. J. Chem. Phys. J. Chem. Phys. J. Chem. Phys. Na J. Chem. Phys* **1994**, *100* (105), 10825–19281.

(40) Bellissent-Funel, M.-C.; Teixeira, J. Dynamics of Water Studied by Inelastic Neutron Scattering. *J. Mol. Struct. Elsevier Sci. Publ. B.V* **1991**, *250*, 213–230.

(41) Berg, M. C.; Dalby, K. N.; Tsapatsaris, N.; Okhrimenko, D. V.; Sørensen, H. O.; Jha, D.; Embs, J. P.; Stipp, S. L. S.; Bordallo, H. N. Water Mobility in Chalk: A Quasielastic Neutron Scattering Study. *J. Phys. Chem. C* **2017**, *121* (26), 14088–14095.

(42) Li, J.; Zhao, K. Effect of Side-Chain on Conformation of Poly(acrylic Acid) and Its Dielectric Behaviors in Aqueous Solution: Hydrophobic and Hydrogen-Bonding Interactions and Mechanism of Relaxations.

(43) Yamazaki, S.; Noda, I.; Tsutsumi, A. 13C NMR Relaxation of Poly(acrylic Acid) in Aqueous Solution. Effects of Charge Density on Local Chain Dynamics. *Polym. J.* **2000**, *32* (1), 87–89.

(44) Volino, F.; Dianoux, A. J. Neutron Incoherent Scattering Law for Diffusion in a Potential of Spherical Symmetry: General Formalism and Application to Diffusion inside a Sphere. *Mol. Phys.* **1980**, *41* (2), 271–279.

(45) Sierra-Martin, B.; Retama, J. R.; Laurenti, M.; Fernández Barbero, A.; López Cabarcos, E. Structure and Polymer Dynamics within PNIPAM-Based Microgel Particles. *Adv. Colloid Interface Sci.* **2014**, *205*, 113–123.

(46) Roosen-Runge, F.; Bicout, D. J.; Barrat, J.-L. Analytical Correlation Functions for Motion through Diffusivity Landscapes. *J. Chem. Phys. J. Chem. Phys. J. Chem. Phys. Chaos J. Chem. Phys.* **2041**, *144* (144), 124105–143129.

(47) Gates, W. P.; Bordallo, H. N.; Aldridge, L. P.; Seydel, T.; Jacobsen, H.; Marry, V.; Churchman, G. J. Neutron Time-of-Flight Quantification of Water Desorption Isotherms of Montmorillonite. *J. Phys. Chem. C* **2012**, *116* (9), 5558–5570.

(48) González Sánchez, F.; Jurányi, F.; Gimmi, T.; Loon, L. Van; Unruh, T.; Diamond, L. W.; Maier-Leibnitz, F. H. Translational Diffusion of Water and Its Dependence on Temperature in Charged and Uncharged Clays: A Neutron Scattering Study. *J. Chem. Phys.* **2008**, *129*.

(49) Chudley, C. T.; Elliott, R. J. Neutron Scattering from a Liquid on a Jump Diffusion Model. *Proc. Phys. Soc.* **1961**, *77* (2), 353–361.

Nanoscale Mobility of Aqueous Polyacrylic Acid in Dental Restorative Cements

Marcella C. Berg[1,2,], Ana R. Benetti[3], Mark T. F. Telling[4,5], Tilo Seydel[6], Dehong Yu[7], Luke L. Daemen[8], Heloisa N. Bordallo[1,2]*

[1] The Niels Bohr Institute, University of Copenhagen, DK-2100, Copenhagen, Denmark

[2] European Spallation Source ESS ERIC, PO Box 176, SE-221 00 Lund, Sweden

[3] Department of Odontology, Faculty of Health and Medical Sciences, University of Copenhagen, DK-2200, Copenhagen, Denmark

[4] ISIS Facility, Rutherford Appleton Laboratory, Chilton, Oxon, UK OX11 0QX

[5] Department of Materials, University of Oxford, Parks Road, Oxford, UK

[6] Institut Max von Laue - Paul Langevin, CS 20156, F-38042 Grenoble, France

[7] Australian Nuclear Science and Technology Organisation, New Illawarra Road, Lucas Heights, NSW

[8] Oak Ridge National Laboratory, P.O. Box 2008, Oak Ridge, TN 37831

KEYWORDS: Glass Ionomer Cements, Porous Structures, Dynamics, Confined Liquids.

Supplementary information

In the supplementary information the Bulk water measurements for comparison with GIC and PAA solution are given. Furthermore GIC after 28 days are shown and GIC modelled to random jump diffusion witch only showed reasonable fit at low Q.

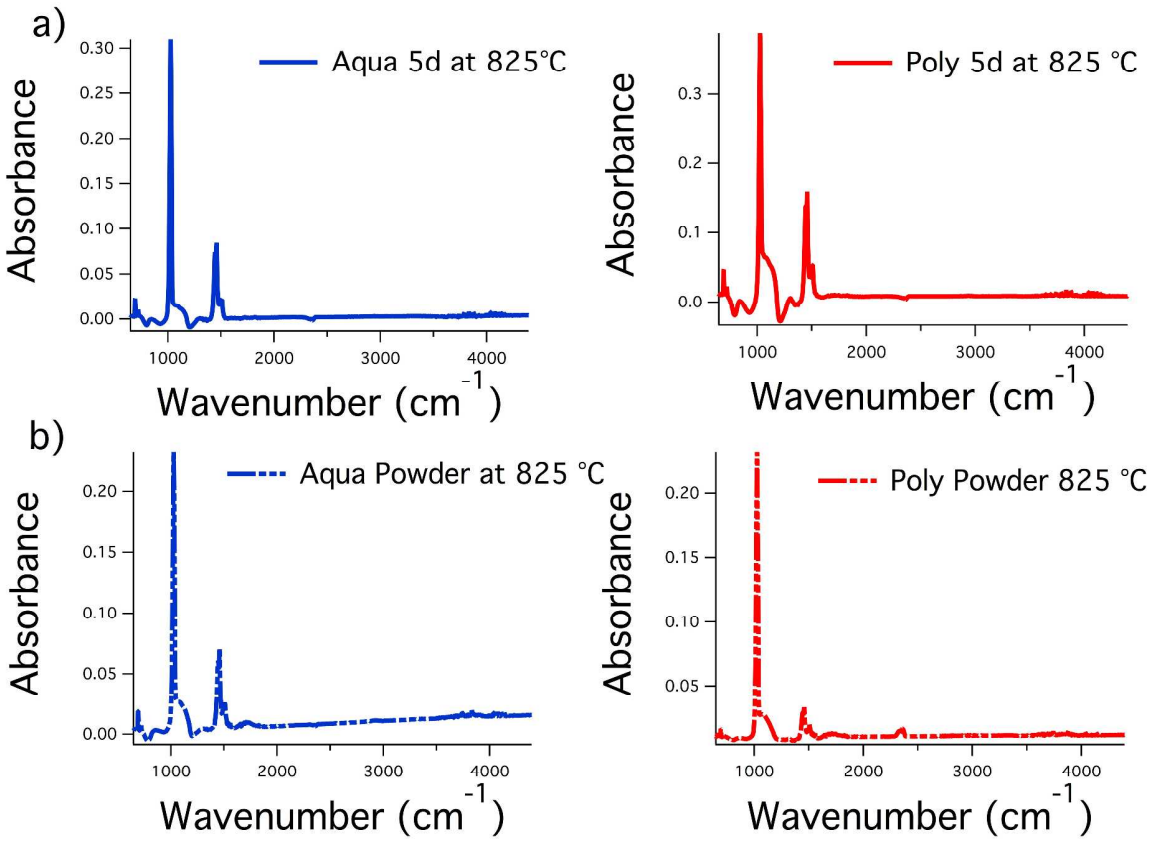

Figure S1: FTIR spectra Aqua (left side in blue) and Poly (right side in red) cements aged for 5 days and their respective powders at the last decomposition stage as observed in the TGA under controlled heating.

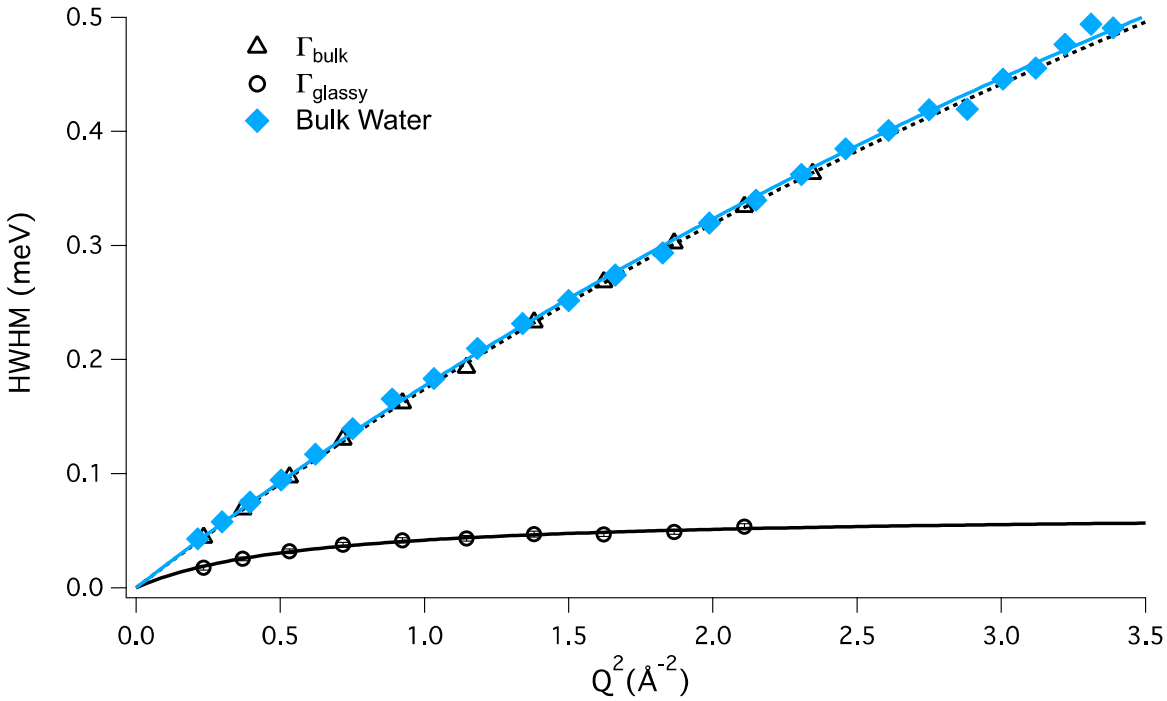

Figure S2: $\Gamma_{water,}$ $\Gamma_{Bulk,\ and}$ Γ_{glassy} v□ Q^2 modelled to the random jump diffusion extracted from the data collected using IRIS. The pure Bulk water is given for comparison with Γ_{Bulk} found in the aqueous PAA solution.

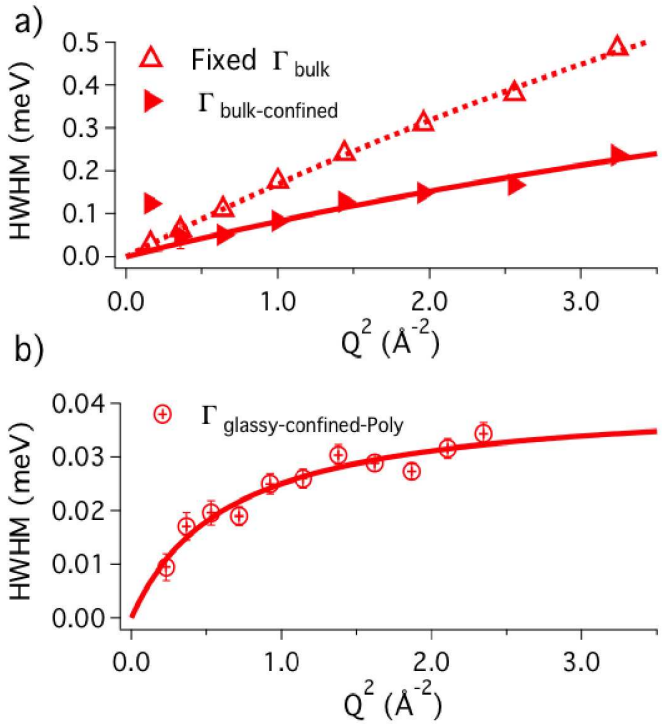

Figure S3: Evolution of the HWHM for Γ_{bulk}, $\Gamma_{bulk\text{-}confined}$ and $\Gamma_{glassy\text{-}confined}$ as a function of Q^2 modelled to the random jump diffusion, for the 28 day old GIC samples Poly. The HWHM does not change as a function of ageing. As an example the Evolution of the HWHM for the Poly cement is given. The parameter Γ_{bulk} was fixed doing the fitting. The Data is obtained from a) PELICAN and b) IRIS.

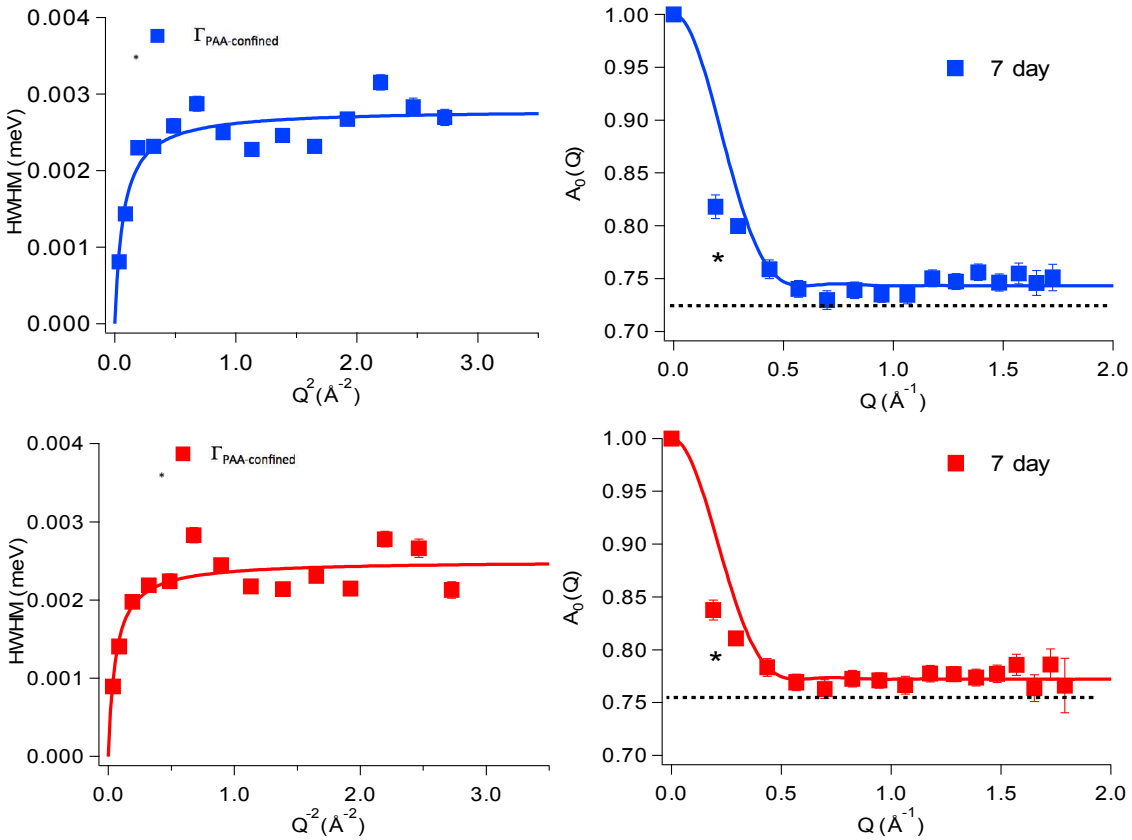

Figure S4: Left side: Evolution of the HWHM for $\Gamma_{PAA\text{-}confined}$ as a function of Q^2 obtained for the GIC samples, Aqua (top, in blue) and Poly (bottom, in red), using IN16B modelled to the random jump diffusion. Right side: EISF as a function of Q obtained from the analysis of the quasielastic spectra for GIC samples aged at 7 days. The solid lines were obtained using the model described by Equation 5, while the horizontal dotted line is a guide to the eye to facilitate the comparison between the amounts of mobile protons (p) in the cements. Evolution of the HWHM and EISF does not change as a function of ageing. The fit for the evolution of the HWHM is reasonable for $Q>0.5\ Q^{-2}$, but deviate at higher Q.

Tale S1: Partial and cumulative percentages of mass loss obtained using thermo gravimetric analysis (TGA) for the Aqua and Poly cements as function of maturation together with their respective powders for different decomposition temperatures. The partial value of the mass loss is taken at end of the decomposition process corresponding to the inflection point temperature, defined by the minimum of the first derivative. The cumulative mass loss for all samples is collected at 900 ºC.

Sample	**110 ºC**	**225 ºC**	**425 ºC**	**470 ºC**	**825 ºC**	**900 ºC**
Aqua 5	13%	-	-	15%	10%	38%
Aqua 28	9%	-	-	15%	8%	32%
Aqua Powder	-	9%	12%	-	9%	30%
Poly 5	8%	-	-	13%	11%	32%
Poly 28	7%	-	-	13%	11%	31%
Poly Powder	-	4%	5%	-	10%	19%

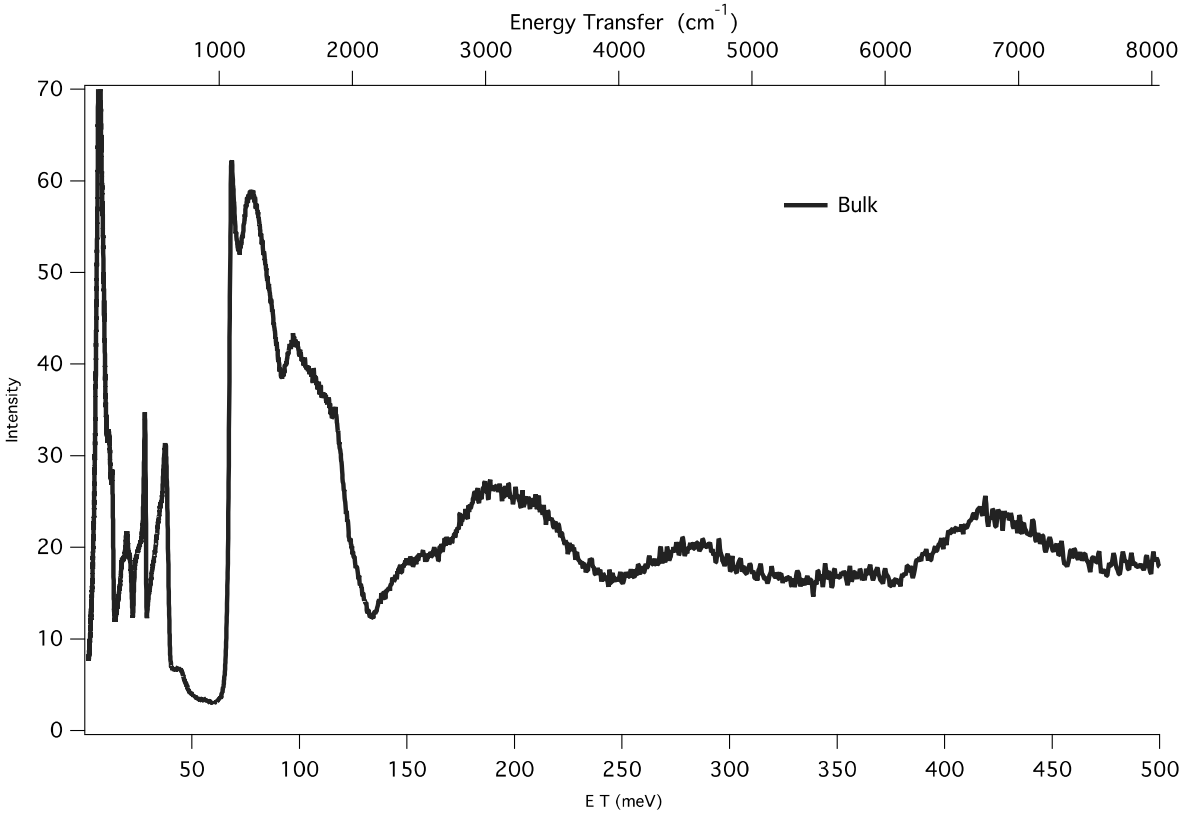

Figure S5: Vibrational transition energies obtained using the vibrational spectrometer, VISION, and collected at 10 K. for Bulk water. The peaks are assigned to the librational and vibrational modes of the samples. Bulk water is given in SI for comparison with the GIC.

Paper 3

THE JOURNAL OF PHYSICAL CHEMISTRY C

Article

pubs.acs.org/JPCC

Water Mobility in Chalk: A Quasielastic Neutron Scattering Study

M. C. Berg,[†,‡] K. N. Dalby,[§,⊥] N. Tsapatsaris,[†,‡,⊥] D. V. Okhrimenko,[§] H. O. Sørensen,[§] D. Jha,[§] J. P. Embs,[∥] S. L. S. Stipp,[§] and H. N. Bordallo*[,†,‡]

[†]Niels Bohr Institute, University of Copenhagen, Universitetsparken 5, 2100 Copenhagen Ø, Denmark

[‡]European Spallation Source ESS AB, P.O. Box 176, SE-221 00 Lund, Sweden

[§]Nano-Science Center, Department of Chemistry, University of Copenhagen, Universitetsparken 5, 2100 Copenhagen Ø, Denmark

[∥]Laboratory for Neutron Scattering and Imaging, Paul Scherrer Institute, CH-5232 Villigen, Switzerland

Supporting Information

ABSTRACT: Water mobility through porous rock has a role to play in many systems, such as contaminant remediation, CO_2 storage, and oil recovery. We used inelastic and quasielastic neutron scattering to describe water dynamics in two different chalk samples that have similar pore volume (ranging from tens of micrometers to a few nanometers) but different water uptake properties. We observed distinct water populations, where the analysis of the quasielastic data shows that after the hydration process most of the water behaves as bulk water. However, the lack of quasielastic signal, together with the observation of a translational mode at 10 meV, imply that in chalk samples that take up less water confinement occurs mostly in the pore volume that is accessible with nitrogen adsorption measurements.

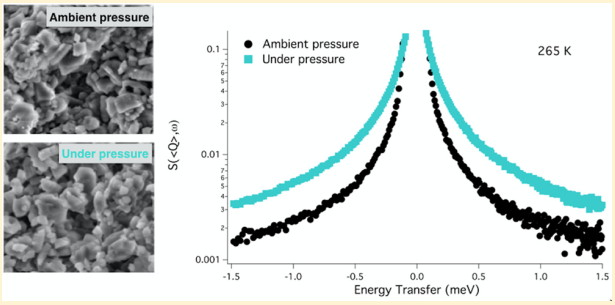

INTRODUCTION

Fluid movement through porous rocks influences many processes relevant for society. For example, water is used to displace contaminated fluids during remediation of drinking water aquifers.[1] Similar hydraulic displacement techniques are used to increase oil recovery beyond what is produced as a result of lithostatic pressure alone. In both cases, water interacts with the pore surfaces in the rock, and despite detailed research on this subject, the processes by which water moves in pores is not fully understood.[2] To better deconvolute the various properties that control water mobility at the pore scale, high-resolution studies at a variety of length and time scales are valuable.

Chalk is an important reservoir rock for both groundwater and hydrocarbons. It is composed predominantly of the fossilized remains of planktonic marine algae that used calcite ($CaCO_3$) to build micrometer-scale platelets called coccoliths. These microfossils result in complex pore geometries in the rock.[3] In some chalk formations, nanoparticles of authigenic clay are observed on the calcite mineral surfaces.[4−6] To date, research has focused on characterizing calcite surface composition,[7−9] determining calcite surface reactivity,[10−12] visualizing pore connectivity in chalk at various length scales using X-ray tomography and scanning electron microscopy (SEM),[13,14] and combining the chemical and physical properties of chalk to create reactive transport models.[15,16] Because of chalk's complexity, the microstructure characterization alone has not yet led to an ability to describe and quantify how water behaves within its nanometer-scale pores. Therefore, in this work, we used neutron spectroscopy to describe the self-diffusivity of the water confined within chalk pore networks.

Water−pore surface interactions control, and are controlled by, the wettability of the rock,[2,17−21] i.e., its preference for water or hydrophobic species. Pore dimension, distribution, and connectivity, as well as the presence of charged ions and organic material, greatly modify water mobility.[6,22−24] Indeed, it has now become widely accepted that water is transported differently, depending on whether it is tightly confined, chemically bound, or in its bulk state.[25−29] However, because of the complex structure of chalk and the very small dimension of the pores and pore throats, it has been difficult to observe these effects experimentally, raising questions about how fluid actually does move. In the particular case of pure calcite surfaces, MD simulations have been used to show that the local environment influences water structure as a result of molecular interactions between the water molecules and the ions at pore surfaces.[30,31] Although a correlation between the separation of water molecules from the calcite surface and water self-diffusivity has been derived from atom trajectories[32] and advanced techniques, including NMR, have improved understanding of the properties of water, it is generally difficult to experimentally quantify the differences between how water behaves on a mineral surface and inside small pores.[21,33,34]

Received: March 1, 2017
Revised: June 2, 2017
Published: June 8, 2017

DOI: 10.1021/acs.jpcc.7b01998
J. Phys. Chem. C 2017, 121, 14088−14095

Table 1. Chalk Properties for the Two Sample Sets A (Ambient) and P (Pressure) Used for the Neutron Scattering Experiments[a]

sample	H_2O uptake (g H_2O per g of chalk) × 10^{-2}	Kr BET surface area, m^2/g	N_2 adsorption	
			BET surface area, m^2/g	Total pore volume, 10^{-2} cm^3/g
Aalborg A	2.8	2.9	-	-
Chalk 2−2 A	16	1.8	-	-
Aalborg P	2.4	3.3	-	-
Chalk 2−2 P	23	1.6	-	-
Aalborg	-	-	3.7	2.3
Chalk 2−2	-	-	2.0	2.1

[a]The accuracy of N_2 surface area determination is 2−5%, while for Kr measurements, with a sensitivity ∼300 times higher than for N_2, detection error is <2% (according to the manufacturer, Quantachrome GmbH). The gas adsorption technique cannot detect pores larger than 400 nm.

We used neutron spectroscopy to obtain experimental evidence for the molecular-scale behavior of water and to test the validity of MD predictions. Neutrons, like X-rays, penetrate matter, and the exceptionally large scattering cross section of H atoms gives unique insight into the movement of hydrogen, in this case in water, providing information about its behavior in confinement, within the pores.[35−38] By using quasielastic neutron scattering (QENS), we obtained information about proton self-diffusion, while inelastic neutron scattering (INS) allowed observation of collective density fluctuations.[39,40]

MATERIALS AND METHODS

Materials. Two chalk samples were used in this study. The first, Aalborg chalk, which we simply call Aalborg, was collected from an active quarry in Jutland, Denmark (Aalborg Portland Cement). The second sample, called Chalk 2−2, was taken from a core that had been drilled from a chalk formation in the Danish North Sea Basin. Geologic evidence indicates that neither sample had ever been exposed to oil. The samples had been stored dry, at ambient temperature and pressure. Prior to the hydration experiments, the samples were gently crushed. They were mounted on flat aluminum sample holders for analysis in the cold time-of-flight spectrometer FOCUS, located at the Paul Scherrer Institut (PSI, Villigen, Switzerland).

Hydration Experiments. The samples used for the neutron experiments were hydrated using two methods. The first samples were wet at ambient conditions (Set A), while the second set were put under pressure (Set P). The initial mass of all samples was 1.4 ± 0.1 g.

Set A was first dried at 450 K in small, aluminum, open beakers while flushing with nitrogen, until no observable decrease in mass was detected (±0.0005 g). Next, the samples were placed in a sealed container that had a separate, 50 mL reservoir, holding ultrapure deionized water (Milli-Q). The container was flushed with nitrogen, and the samples were allowed to equilibrate in the vapor produced by evaporating the water in the reservoir at 293 K for 24 h. Set P was placed in a pressure vessel that contained water vapor as the pressure medium. The pressure that developed during the hydration procedure corresponds approximately to 4.1 bar and a maximum temperature of 423 K; the samples were left to equilibrate for 24 h.

To calculate the hydration state of Sets A and P, reference mass measurements of the individual sample holders were made using a laboratory mass balance (±0.0005 g). The weight of the sample+sample holder assembly was then measured on the same scale before and after each hydration step. After subtracting the weight of the sample holder, the sample mass change in % was calculated from the ratio of the hydrated sample to the dried sample mass. The hydration state of the samples is presented in Table 1. To avoid water loss during transport, all samples were kept in the sealed containers with a hydrating atmosphere of ultrapure water.

Gas Adsorption for BET Surface Area and Porosity Determination. Before the hydration experiments, the surface area was determined from ∼3.0 g subsamples using nitrogen gas, while another smaller subsample (∼0.35 g) was taken from the hydrated Sets A and P (that were used for the neutron scattering experiments) and analyzed using krypton gas. To ensure full dehydration prior to data collection, all samples were degassed by heating to 423 K in vacuum (<10^{-6} bar) for 2 h. Measurements were made at liquid nitrogen temperature, using a Quantachrome Autosorb-1 Sorption Analyzer. The specific surface area was determined from the Kr and N_2 adsorption isotherms in the relative pressure range $0.1 < P/P_0 < 0.3$, using the BET equation.[41] The saturated equilibrium vapor pressure, P_0, for krypton was assumed to be 0.35 bar at liquid nitrogen temperature. This corresponds to the vapor pressure of the supercooled liquid state of krypton. For all samples, the BET plots were linear (i.e., the regression coefficient was higher than 0.999) in the relative pressure range examined, confirming the applicability of the BET equation.

Total pore volume was determined at relative pressure, P/P_0, close to unity, using N_2 adsorption isotherms and the relationship between the volume of adsorbed nitrogen and the volume of liquid nitrogen in the pores, given by eq 1

$$V_{liq} = \frac{P_a \cdot V_{ads} \cdot V_m}{RT} \quad (1)$$

where V_{ads} represents the volume of adsorbed nitrogen; V_{liq} represents the volume of liquid nitrogen contained in the pores; P_a and T represent ambient pressure and temperature; and V_m is the molar volume of the liquid nitrogen (34.7 cm^3/mol).

The pore size distribution analysis was made using the t-plots[42,43] method for micropores (<2 nm), and we used BJH analysis[44] from the desorption branch of the nitrogen isotherm to determine pore distribution for the range from 3 to 200 nm.

Scanning Electron Microscopy (SEM). A Quanta 3D FEG SEM was used to observe chalk morphology and particle size. Images were taken in low vacuum (0.6 mbar) to avoid coating the samples so that we could image the same samples before and after the hydration experiments. We used 10 kV and 46 pA and a low vacuum secondary electron detector, and we took images of the same samples before and after the hydration experiments.

Inelastic and Quasielastic Neutron Scattering Experiments. The dynamic behavior of the chalk samples was studied by means of inelastic and quasielastic neutron scattering (INS

DOI: 10.1021/acs.jpcc.7b01998
J. Phys. Chem. C 2017, 121, 14088−14095

and QENS), using the cold time-of-flight spectrometer FOCUS. All four samples were measured using an incident neutron wavelength of 5 Å, resulting in an elastic energy resolution of ~110 μeV. At this setting, the accessible momentum transfer range was from 0.4 to 2 Å^{-1}, and the energy transfer range was +1.7 to −30 meV, covering relaxation phenomena from 80 ps to 130 fs. The samples were loaded between thin aluminum sheets and sealed in a flat aluminum sample holder. An empty cell was measured for background subtraction and a vanadium reference for detector calibration. Using an orientation angle of 135° with respect to the incident neutron beam direction allows access to the low angular range of the spectrum but shades the detectors at higher angles. Spectra were collected at six temperatures, ranging between 100 and 300 K. The data were analyzed using the procedures described elsewhere,[39] with the DAVE and LAMP software.

The measured scattering function, $S(Q, \omega)$, where Q represents the magnitude of the scattering wave vector and ω represents the energy transfer, expresses the contributions for the various types of motion of the water molecules, depending on the temperature and the energy resolution (time) range. $S(Q, \omega)$ could be decomposed into three components: elastic, $S_E(Q, \omega = 0)$, quasielastic, $S_{QE}(Q, \omega \approx 0)$, and inelastic, where the sample or system gains energy, $S_{INS}(Q, \omega > 0)$.

The short time dynamics of the hydrogen atoms mainly determines the inelastic part of the spectrum, $S_{INS}(Q, \omega > 0)$, while a broader view of confined or interfacial water dynamics can be obtained by the quasielastic part of the spectrum, $S_{QE}(Q, \omega \approx 0)$. It is the quasielastic results that give valuable insight into the pore−water interactions, which is the focus of our study.

RESULTS AND DISCUSSION

SEM. To more accurately interpret the neutron results, it is important that the complex microstructure of the chalk remained unchanged during the hydration experiments. The SEM results, Figure 1, show that there were fragments and subrounded particles that are remnants of coccoliths and some angular calcite grains that likely precipitated during diagenesis,[2] but no observable changes, at this scale, were produced by the different hydration procedures.

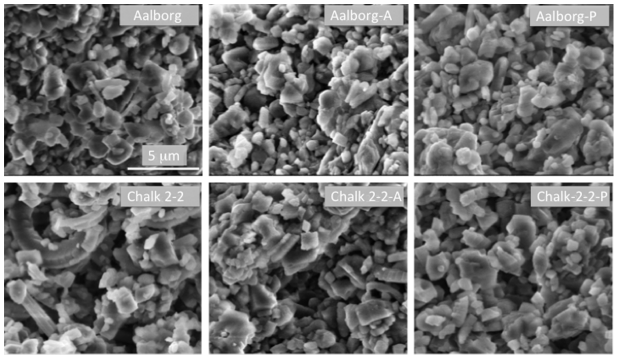

Figure 1. Scanning electron microscopy images of the chalk samples used in this study: fresh (left), Set A (middle), and Set P (right). No visible change in particle size or shape could be observed following the two hydration procedures. The scale bar is 5 μm, the same for all images. Measurements were made under low vacuum to avoid the need for a conductive coating.

Hydration and BET. For all samples, the BET plots were linear in the relative pressure range examined, confirming the validity of applying the BET equation. The total pore volume was estimated at nitrogen relative pressure, $P/P_0 = 0.995$, from the total amount of adsorbed N_2, assuming cylindrical pore geometry. The pore size distribution obtained from N_2 adsorption measurements by t-plots and BJH analysis is similar for both Aalborg and Chalk 2−2. These results are given in the Supporting Information, Figure S1 and Figure S2.

Mass change with hydration, BET surface area (using N_2 and Kr), and total pore volume are summarized in Table 1. The Aalborg chalk has a significantly higher surface area than Chalk 2−2 from analyses with Kr and N_2. However, despite the total pore volume (~2.2 × 10^{-2} cm^3/g) being similar, Chalk 2−2 takes up ~10 times more water than Aalborg. From this data, we can conclude that for the Aalborg samples the water absorbed during hydration fits well within the determined pore volume by N_2 adsorption. However, this is not the case for Chalk 2−2. Considering that nitrogen pore determination experiments only access pores <400 nm, the higher water content measured in Chalk 2−2 can be attributed either to the presence of larger pores or to a hydrophilic surface. To better understand why chalk samples with similar pore volumes take up very different amounts of water, we turned to inelastic neutron scattering.

Short Time Dynamics. In Figure 2 and Figure 3, we show the generalized vibrational density of states (GDOS) for the Aalborg and Chalk 2−2 samples as a function of temperature and sample preparation (A and P). The GDOS was obtained using the incoherent one-phonon approximation[45]

$$G(Q, \omega) = \frac{m_{H_2O}}{k_B T}\left(\frac{\hbar\omega}{Q}\right)^2 e^{-\hbar\omega/k_B T} S_H(Q, \omega) \quad (2)$$

where m denotes the mass of the scattering units (here the water molecule); k_B represents the Boltzmann constant; T is the temperature; $\hbar\omega$ gives the neutron energy transfer; and $S_H(Q, \omega)$ represents the experimental incoherent scattering function (here, dominated by the motion of the H atom). To improve the statistics, $G(Q, \omega)$ was obtained after averaging over all of the Q-values considered in the experiment, but this smooths the coherence effects of the scattering. This is called the incoherent approximation.

Normal modes of bulk water include two distinct groups of vibrations.[46] The first is in the high frequency domain ($50 < \omega < 125$ meV) and involves rotation as well as restricted rotational degrees of freedom. We do not show these in Figure 2 and Figure 3 because this energy range is out of the $(Q - \omega)$ space covered by FOCUS. The second group of vibrations is found in the lower frequency domain ($0 < \omega < 44$ meV) and is assigned to the translational degrees of freedom. These are the vibrations that we discuss further.

The signal/noise ratios observed in the low frequency domain of Aalborg and Chalk 2−2 (Figure 2 and Figure 3), which correspond directly to the amount of water in the systems, confirm that Chalk 2−2 has a higher water content than Aalborg, in full agreement with the mass change after hydration (Table 1). At 300 K (Figure 2a), the A samples have different peak positions, at ~6 meV (Chalk 2−2 A) and ~10 meV (Aalborg A). These indicate that the water environment is different for the two samples. Here we note that based on measurements from neutron and Raman scattering in bulk water the peak observed at ~6 meV is assigned to O−O−O

DOI: 10.1021/acs.jpcc.7b01998
J. Phys. Chem. C 2017, 121, 14088−14095

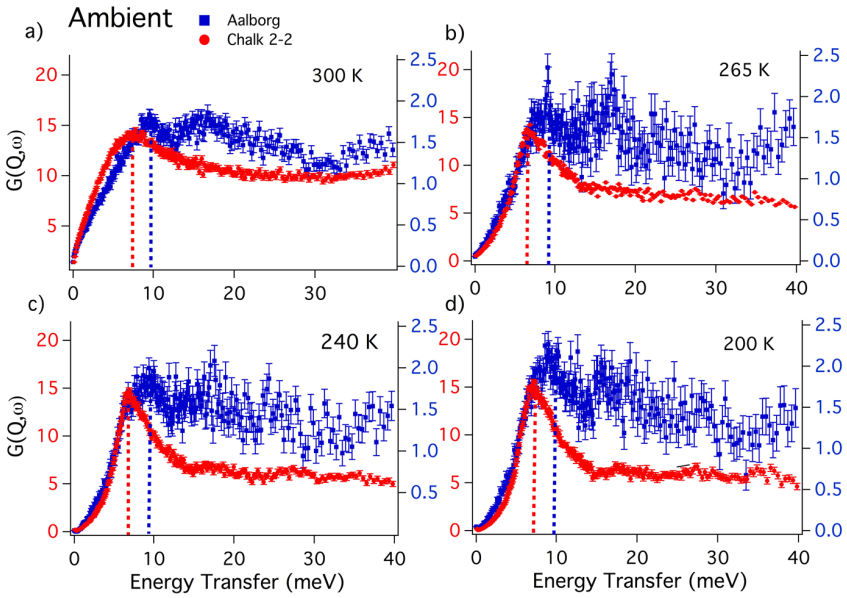

Figure 2. Temperature evolution of the generalized vibrational density of states (GDOS) for Aalborg (2.8×10^{-2} g of H_2O per g of chalk) and Chalk 2−2 (16×10^{-2} g of H_2O per g of chalk), hydrated under ambient conditions (Set A), obtained from experimental incoherent inelastic scattering, collected from the FOCUS instrument: 1 meV ≈ 8 cm^{-1}. The lower water uptake in the Aalborg sample is directly reflected by its lower scattering intensity and consequently larger error bars.

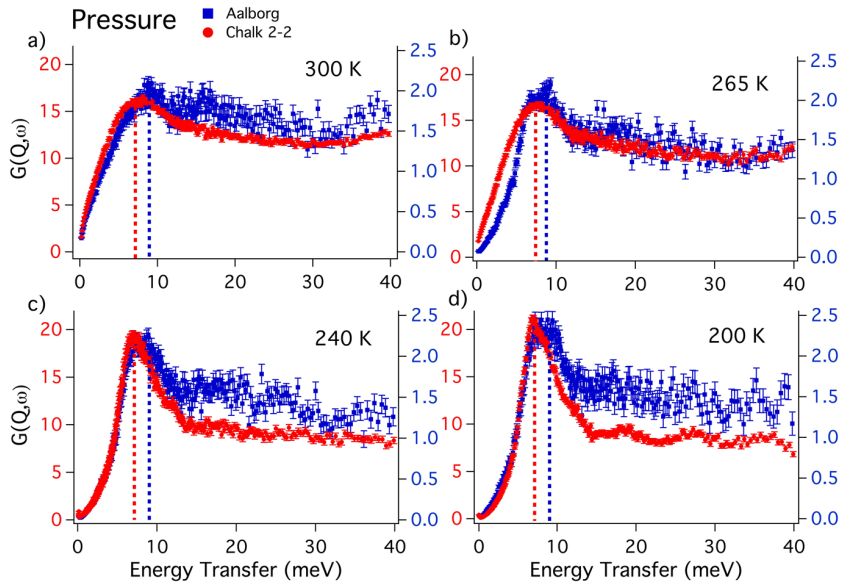

Figure 3. Temperature evolution of the generalized vibrational density of states (GDOS) for Aalborg (2.4×10^{-2} g of H_2O per g of chalk) and Chalk 2−2 (23×10^{-2} g of H_2O per g of chalk) hydrated under pressure (Set P in each case), obtained from experimental incoherent inelastic scattering, collected from the FOCUS instrument: 1 meV ≈ 8 cm^{-1}.

bending,[47,48] while it is well-known that confined water molecules are characterized by a vibrational mode centered at about 10 meV.[49,50] This is consistent with the N_2 adsorption results; i.e., the water absorbed by the Aalborg A sample is confined in pores smaller than 400 nm. The second peak at 15 meV is assigned to external modes in calcite, as a result of molecular vibrations in the unit cell.[51]

To further probe how the water is confined within the chalk and to determine how it behaves on particle surfaces, the samples were progressively cooled (Figure 2b, Figure 2c, and Figure 2d). For Chalk 2−2 A, as the water molecules became more structured between 300 and 265 K, the peak at 6 meV narrowed. However, in Aalborg A, because of confinement, cooling did not influence the hydrogen network to the same degree.

Comparison of the spectra obtained at 300 K (Figure 2a and Figure 3a), for the samples prepared by hydration under pressure, shows that the spectral distribution for Chalk 2−2 P is more similar to that observed for Aalborg P, with the peak assigned to O−O−O bending shifted slightly to higher frequencies. Considering that the applied pressure was not sufficient to modify the pore structure, based on this data set,

DOI: 10.1021/acs.jpcc.7b01998
J. Phys. Chem. C 2017, 121, 14088−14095

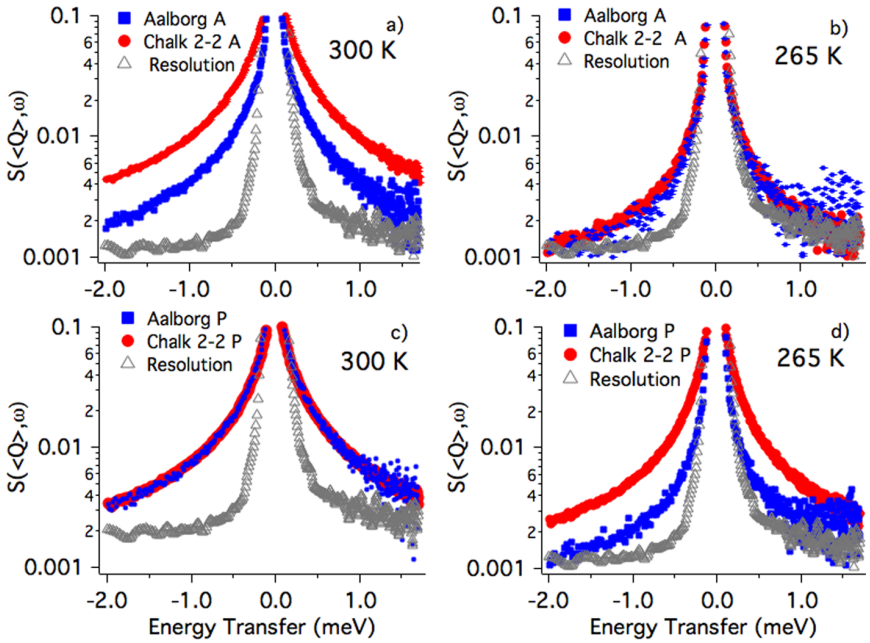

Figure 4. QENS experimental spectra for Aalborg and Chalk 2−2, Sets A and P at 300 and 265 K summed over all the detectors. The signal is normalized to the amount of water in the samples; i.e., for Set A (a, b) Aalborg contains 2.8×10^{-2} g of H_2O per g of chalk and Chalk 2−2 16×10^{-2} g of H_2O per g of chalk, whereas for Set P (c, d) Aalborg contains 2.4×10^{-2} g of H_2O per g of chalk and Chalk 2−2 23×10^{-2} g of H_2O per g of chalk. The data for Sets A and P were rescaled so the *y*-axes represent 10% of the normalized signal at zero energy transfer. For a better visualization of the QE signal, the *y*-scale is logarithmic, and for comparison, the resolution function is also shown.

we suggest that hydrating the samples under pressure changes the environment around the H bond network. This indicates that applied pressure in Chalk 2−2 facilitates the inclusion of water in the pores. Moreover, at 265 K, the spectral distribution below 6 meV is different, with Chalk 2−2 P still maintaining its room-temperature bulk water behavior. This is further discussed in the next section.

Picosecond Dynamics. The sum of the QE spectra obtained at 265 and 300 K for Sets A and P over all *Q*-range is shown in Figure 4. At 265 K, as depicted in Figure 4b and Figure 4d, a clear QE response is observed in Chalk 2−2 P. For samples prepared at ambient conditions (Set A), this component cannot be modeled.

To further understand how the H bonds behave in these samples, we analyzed the diffusion of the water molecules by examining the QENS response in the spectra as a function of *Q*. In order to obtain a quantitative analysis of these results, all data were fitted using a single Lorentzian function

$$S(Q, \omega) = \mathrm{DWF}[(A_0(Q)\delta(\omega) + (1 - A_0(Q)L(\Gamma, \omega)) \otimes R(Q, \omega)] + B(Q) \quad (3)$$

where DWF represents the Debye−Waller factor; $A_0(Q)$ represents the time-averaged spatial distribution of all scatterers; and $L(\Gamma, \omega)$ indicates the Lorentzian representing the broadened energy distribution that results from neutron−nucleus collisions, corresponding to the population statistics of one relaxation process. $R(Q, \omega)$ denotes the resolution function of the instrument; $B(Q)$ represents a flat background term that includes spectral intensity arising from fast motions outside the instrument resolution; and $\delta(\omega)$ is a delta function that represents the particles that are seen as immobile in the time window probed by the technique. The behavior of the extracted half width at half-maximum (Γ, HWHM) is shown in Figure 5.

Considering a random diffusion process, the variation of Γ vs *Q* can be approximated by the Singwi and Sjölander model[52]

$$\Gamma_T(Q) = \frac{D_t Q^2}{1 + D_t Q^2 \tau_0} \text{ and } D_t = \frac{L^2}{6\tau_0} \quad (4)$$

where D_t represents the self-diffusion coefficient, τ_0, represents the average residence time between jumps describing the time that water molecules take to diffuse from an initial position to another, giving insight into the hydrogen bond lifetime. *L* is the mean jump distance. The fitted parameters that characterize the translational motion of the water molecules are presented in Table 2.

At 300 K and within the accuracy of our data, both the average translational diffusion coefficient, D_t, and the average residence time between jumps, τ_0, in all chalk samples differ from those of bulk water.[53] Considering that hydrophobically confined water has a lower number of hydrogen bonds per molecule and they form a network similar to that of the vapor phase,[54] the higher D_t can be interpreted to result from the interaction between the water molecules and the hydrophobic surfaces of the chalk samples. This is also consistent with the lower intermolecular water−water interaction that is reflected by the decrease of τ_0.[38] Furthermore, the changes in the spectral distribution, both GDOS and QENS, as well as the 44% increase in water uptake (Table 1) for Chalk 2−2 prepared under pressure, is consistent with molecular dynamics simulations showing that water flux into hydrophobic surfaces increases with increasing pressure.[55]

On cooling, as the water molecules undergo a phase transition from a vapor like (low density) phase to a more ordered network (high density), confinement size effects might undermine the hydrophobicity of the surface.[56] Consequently, at 265 K, the diffusion coefficient of Chalk 2−2 P approaches

DOI: 10.1021/acs.jpcc.7b01998
J. Phys. Chem. C 2017, 121, 14088−14095

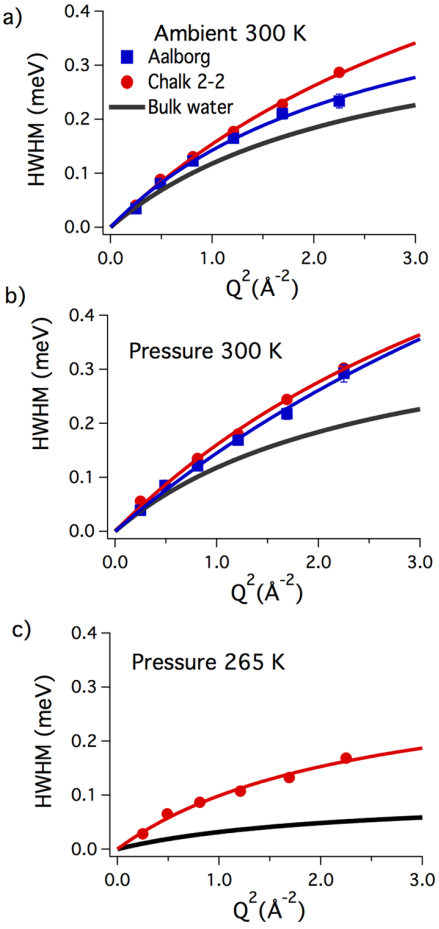

Figure 5. Evolution of the half width at half-maximum (HWHM) of the quasielastic broadening measured from FOCUS as a function of momentum transfer, Q, using eq 3 for Aalborg and Chalk 2−2, Sets A and P at 300 K and for Chalk 2−2, Set P at 265 K. The line is the fit to the experimental data, according to the phenomenological model of eq 4. For comparison the results for bulk water taken from ref 47 were reproduced (black line).

Table 2. Diffusion Parameters Resulting from Fitting the Water QENS Data[a]

sample	L (Å)	τ_0 (ps)	D_t (10^{-9} m^2/s)
Bulk water at 300 K	1.53	1.57 ± 0.12	2.49 ± 0.07
Bulk water at 263 K	1.65	6.47	0.7
Aalborg A at 300 K	1.4	1.2 ± 0.2	2.9 ± 0.2
Aalborg A at 265 K	could not be modeled[b]		
Chalk 2−2 A at 300 K	1.2	0.8 ± 0.1	2.8 ± 0.1
Chalk 2−2 A at 265 K	could not be modeled[b]		
Aalborg P at 300 K	1.2	0.9 ± 0.1	2.8 ± 0.1
Aalborg P at 265 K	could not be modeled[b]		
Chalk 2−2 P at 300 K	1.1	0.7 ± 0.1	2.9 ± 0.2
Chalk 2−2 P at 265 K	1.6	2.0 ± 0.3	2.1 ± 0.2

[a]The values were obtained using the jump diffusion model with the fitting model of eqs 3 and 4. The results from bulk water at 300 K were taken from ref 53 and at 263 K from ref 47. [b]Although a quasielastic signal is still visible at 265 K, its intensity is very small, and the resulting variation of the HWHM as a function of scattering vector-Q could not be unambiguously modeled.

that of bulk water, while the GDOS confirms a more bulk like behavior. Conversely, in Aalborg, independently of the sample preparation method, the lack of a quasielastic signal as well as the observation of a peak at 10 meV in the spectral distribution (Figure 2, Figure 3, and Figure 4) and the BET results (Table 1) imply that size effects play a more important role in the behavior of the dynamics of the absorbed water. This is consistent with Aalborg water being trapped in pores <400 nm diameter. Indeed, from previous work, we know that many factors can influence hydration and water mobility in chalk, including the presence of pore blocking clays and adventitious carbon,[21,32,33,54,57,58] as well as the size and connectivity of pores.[59−61] However, considering that clay and adventitious carbon in Chalk 2−2 and Aalborg are roughly similar[4,6] and assuming that the pore surfaces have similar wetting (hydrophobic) properties, we interpret that it must be the pore network connectivity and pore size distribution that control fluid uptake and water movement in these samples, explaining the differences in the BET results.

CONCLUSIONS

The driving force for water filling pores in the two chalk samples, Aalborg from an outcrop in northwestern Denmark and Chalk 2−2 from a drill core from the Danish North Sea Basin, remains poorly understood. With neutron spectroscopy, we distinguished their water population (peak position from GDOS as well as diffusion coefficient from QENS) and changes of local water geometry attributable to the influence of its local environment (τ_0). Despite their similar pore volumes (from N_2 adsorption isotherms), the samples displayed vastly different water uptake abilities. The higher water uptake of Chalk 2−2, regardless of preparation method, was clearly reflected in the intensity of the GDOS data. The peak observed at 10 meV, assigned to confined water molecules in Aalborg, further confirms that water mobility is more restricted in the sample that absorbs less water. In addition, the QENS data show that, independent of preparation method, Aalborg and Chalk 2−2 have a similar translational diffusion (D_t), which is faster than bulk water at 300 K. This behavior, different from pure confinement (i.e., slowing down of the water molecule diffusion), is largely triggered by the hydrophobicity of the surface. On the other hand, on cooling, as the water molecules become more ordered, confinement size effects start controlling water diffusion. To conclude, we have shown that in chalk hydration water is influenced by the pore surface and/or by pore confinement. This confirms previous modeling results for calcium−water interactions as well as hydrophobic−water interactions in general.

ASSOCIATED CONTENT

Supporting Information

The Supporting Information is available free of charge on the ACS Publications website at DOI: 10.1021/acs.jpcc.7b01998.

Details for the gas adsorption for BET surface area and porosity determination (PDF)

AUTHOR INFORMATION

Corresponding Author

*E-mail: bordallo@nbi.ku.dk. Phone: +45 213 08 829.

ORCID

D. V. Okhrimenko: 0000-0001-7279-1292

J. P. Embs: 0000-0002-2816-2875

DOI: 10.1021/acs.jpcc.7b01998
J. Phys. Chem. C 2017, 121, 14088−14095

H. N. Bordallo: 0000-0003-0750-0553

Author Contributions

[⊥]K.N.D. and N.T. contributed equally. N.T. and H.N.B. conceived the project with input from K.N.D., H.O.S., and S.L.S.S.. K.N.D., N.T., D.V.O., H.O.S., and D.J. prepared and characterized the samples. N.T. designed the neutron scattering experiment, which was carried out by K.N.D., N.T., D.J., and J.P.E.. D.V.O. and M.C.B. analyzed the BET and neutron scattering data, respectively. M.C.B., K.N.D., and H.N.B. wrote the paper with input from D.V.O., H.O.S., and S.L.S.S.. The manuscript was approved by all coauthors in its final version.

Notes

The authors declare no competing financial interest.

■ ACKNOWLEDGMENTS

The experiments were performed at the Swiss spallation neutron source SINQ, Paul Scherrer Institute, Villigen, Switzerland. The work was funded by the European Commission (EC) seventh Framework Program for research, technological development and demonstration under NMI3-II Grant Number 283883, and the Danish Agency for Science, Technology and Innovation through DANSCATT. H.N.B. acknowledges support from the CoNext project. D.J. was supported by an EC, Marie Curie PhD Fellowship from the Initial Training Network called MINSC. Salary for K.N.D., D.V.O., and H.O.S. was provided by the Nano-Chalk Venture, funded by the Danish Advanced Technology Foundation and Maersk Oil and Gas A/S, with a small portion from the P^3 Project, funded by Innovation Fund Denmark and Maersk Oil and Gas A/S. The authors thank Maersk Oil and Gas A/S for Chalk 2-2 and Aalborg Portland A/S for access to their quarry.

■ REFERENCES

(1) Gerhard, J. I.; Kueper, B. H.; Hecox, G. R. The Influence of Waterflood Design on the Recovery of Mobile DNAPLs. *Groundwater* **1998**, *36*, 283−292.

(2) Hassenkam, T.; Skovbjerg, L. L.; Stipp, S. L. S. Probing the Intrinsically Oil-Wet Surfaces of Pores in North Sea Chalk at Subpore Resolution. *Proc. Natl. Acad. Sci. U. S. A.* **2009**, *106*, 6071−6076.

(3) Müter, D.; Sørensen, H. O.; Bock, H.; Stipp, S. L. S. Particle Diffusion in Complex Nanoscale Pore Networks. *J. Phys. Chem. C* **2015**, *119*, 10329−10335.

(4) Skovbjerg, L. L.; Hassenkam, T.; Makovicky, E.; Hem, C. P.; Yang, M.; Bovet, N.; Stipp, S. L. S. Nano Sized Clay Detected on Chalk Particle Surfaces. *Geochim. Cosmochim. Acta* **2012**, *99*, 57−70.

(5) Skovbjerg, L. L.; Okhrimenko, D. V.; Khoo, J.; Dalby, K. N.; Hassenkam, T.; Makovicky, E.; Stipp, S. L. S. Preferential Adsorption of Hydrocarbons to Nanometer-Sized Clay on Chalk Particle Surfaces. *Energy Fuels* **2013**, *27*, 3642−3652.

(6) Okhrimenko, D. V.; Dalby, K. N.; Skovbjerg, L. L.; Bovet, N.; Christensen, J. H.; Stipp, S. L. S. The Surface Reactivity of Chalk (Biogenic Calcite) with Hydrophilic and Hydrophobic Functional Groups. *Geochim. Cosmochim. Acta* **2014**, *128*, 212−224.

(7) Möller, P. Determination of the Composition of Surface Layers of Calcite in Solutions Containing Mg^{2+}. *J. Inorg. Nucl. Chem.* **1973**, *35*, 395−401.

(8) Stipp, S. L.; Hochella, M. F. Structure and Bonding Environments at the Calcite Surface as Observed with X-Ray Photoelectron Spectroscopy (XPS) and Low Energy Electron Diffraction (LEED). *Geochim. Cosmochim. Acta* **1991**, *55*, 1723−1736.

(9) Watson, E. B. A Conceptual Model for near-Surface Kinetic Controls on the Trace-Element and Stable Isotope Composition of Abiogenic Calcite Crystals. *Geochim. Cosmochim. Acta* **2004**, *68*, 1473−1488.

(10) Stipp, S. L. S.; Eggleston, C. M.; Nielsen, B. S. Calcite Surface Structure Observed at Microtopographic and Molecular Scales with Atomic Force Microscopy (AFM). *Geochim. Cosmochim. Acta* **1994**, *58*, 3023−3033.

(11) Henriksen, K.; Stipp, S. L. S.; Young, J. R.; Marsh, M. E. Biological Control on Calcite Crystallization: AFM Investigation of Coccolith Polysaccharide Function. *Am. Mineral.* **2004**, *89*, 1709−1716.

(12) Bisschop, J.; Dysthe, D. K.; Putnis, C. V.; Jamtveit, B. In Situ AFM Study of the Dissolution and Recrystallization Behaviour of Polished and Stressed Calcite Surfaces. *Geochim. Cosmochim. Acta* **2006**, *70*, 1728−1738.

(13) Tomutsa, L.; Radmilovic, V. Focused Ion Beam Assisted Three-Dimensional Rock Imaging at Submicron Scale. *Society of Core Analysts*; 2003, Report Number: LBNL-52648.

(14) Müter, D.; Sørensen, H. O.; Jha, D.; Harti, R.; Dalby, K. N.; Suhonen, H.; Feidenhans'l, R.; Engstrøm, F.; Stipp, S. L. S. Resolution Dependence of Petrophysical Parameters Derived from X-Ray Tomography of Chalk. *Appl. Phys. Lett.* **2014**, *105*, 43108.

(15) Mangeret, A.; De Windt, L.; Crançon, P. Reactive Transport Modelling of Groundwater Chemistry in a Chalk Aquifer at the Watershed Scale. *J. Contam. Hydrol.* **2012**, *138*, 60−74.

(16) Yang, Y., Bruns, S., Stipp, S. L. S., Sørensen, H. O. Reactive Infiltration Instability Amplifies the Difference Between Geometric and Reactive Surface Areas in Natural Porous Materials. http://arxiv.org/abs/1704.01060 (accessed June 2, 2017).

(17) Stipp, S. L. S. Toward a Conceptual Model of the Calcite Surface: Hydration, Hydrolysis, and Surface Potential. *Geochim. Cosmochim. Acta* **1999**, *63*, 3121−3131.

(18) Hirasaki, G.; Zhang, D. L. Surface Chemistry of Oil Recovery from Fractured, Oil-Wet, Carbonate Formations. *SPE J.* **2004**, *9*, 151−162.

(19) Zhang, P.; Austad, T. Wettablility and Oil Recovery from Carbonates: Effects of Temperature and Potential Determining Ions. *Colloids Surf., A* **2006**, *279*, 179−187.

(20) Bohr, J.; Wogelius, R. A.; Morris, P. M.; Stipp, S. L. S. Thickness and Structure of the Water Film Deposited from Vapour on Calcite Surfaces. *Geochim. Cosmochim. Acta* **2010**, *74*, 5985−5999.

(21) Cooke, D. J.; Gray, R. J.; Sand, K. K.; Stipp, S. L. S.; Elliott, J. A. Interaction of Ethanol and Water with the {10$\bar{1}$4} Surface of Calcite. *Langmuir* **2010**, *26*, 14520−14529.

(22) Kim, J.-S.; Choi, J. S.; Lee, M. J.; Park, B. H.; Bukhvalov, D.; Son, Y.-W.; Yoon, D.; Cheong, H.; Yun, J.-N.; Jung, Y.; et al. Between Scylla and Charybdis: Hydrophobic Graphene-Guided Water Diffusion on Hydrophilic Substrates. *Sci. Rep.* **2013**, *3*, 96104.

(23) Pham, T. T.; Lemaire, T.; Capiez-Lernout, E.; Lewerenz, M.; To, Q.-D.; Christie, J. K.; Di Tommaso, D.; de Leeuw, N. H.; Naili, S. Properties of Water Confined in Hydroxyapatite Nanopores as Derived from Molecular Dynamics Simulations. *Theor. Chem. Acc.* **2015**, *134*, 59.

(24) Matthiesen, J.; Hassenkam, T.; Bovet, N.; Dalby, K. N.; Stipp, S. L. S. Adsorbed Organic Material and its Control on Wettability. *Energy Fuels* **2017**, *31*, 55−64.

(25) Maddox, S. A.; Gomez, P.; Mccall, K. R.; Eckert, J. Water Mobility in Calico Hills Tuff Measured by Quasielastic Neutron Scattering. *Geophys. Res. Lett.* **2002**, *29*, 1259.

(26) Bordallo, H. N.; Aldridge, L. P.; Churchman, G. J.; Gates, W. P.; Telling, M. T. F.; Kiefer, K.; Fouquet, P.; Seydel, T.; Kimber, S. A. J. Quasi-Elastic Neutron Scattering Studies on Clay Interlayer-Space Highlighting the Effect of the Cation in Confined Water Dynamics. *J. Phys. Chem. C* **2008**, *112*, 13982−13991.

(27) Jacobsen, J.; Rodrigues, M. S.; Telling, M. T. F.; Beraldo, A. L.; Santos, S. F.; Aldridge, L. P.; Bordallo, H. N.; Dobbs, R.; Neville, A. M.; Isaia, G. C.; et al. Nano-Scale Hydrogen-Bond Network Improves the Durability of Greener Cements. *Sci. Rep.* **2013**, *3*, 69−76.

(28) Sattig, M.; Vogel, M. Dynamic Crossovers and Stepwise Solidification of Confined Water: A ^{2}H NMR Study. *J. Phys. Chem. Lett.* **2014**, *5*, 174−178.

DOI: 10.1021/acs.jpcc.7b01998
J. Phys. Chem. C 2017, 121, 14088−14095

(29) Chiavazzo, E.; Fasano, M.; Asinari, P.; Decuzzi, P. Scaling Behaviour for the Water Transport in Nanoconfined Geometries. *Nat. Commun.* **2014**, *5*, 3565.
(30) Wolthers, M.; Di Tommaso, D.; Du, Z.; de Leeuw, N. H.; Hiemstra, T.; Riemsdijk, W. H.; Morse, J. W.; Andersson, A. J.; Mackenzie, F. T.; Boyle, E. A.; et al. Calcite Surface Structure and Reactivity: Molecular Dynamics Simulations and Macroscopic Surface Modelling of the Calcite−Water Interface. *Phys. Chem. Chem. Phys.* **2012**, *14*, 15145−15157.
(31) Andersson, M. P.; Hem, C. P.; Schultz, L. N.; Nielsen, J. W.; Pedersen, C. S.; Sand, K. K.; Okhrimenko, D. V.; Johnsson, A.; Stipp, S. L. S. Infrared Spectroscopy and Density Functional Theory Investigation of Calcite, Chalk, and Coccoliths—Do we Observe the Mineral Surface? *J. Phys. Chem. A* **2014**, *118*, 10720−10729.
(32) Perry, T. D.; Cygan, R. T.; Mitchell, R. Molecular Models of a Hydrated Calcite Mineral Surface. *Geochim. Cosmochim. Acta* **2007**, *71*, 5876−5887.
(33) Korb, J.-P.; Nicot, B.; Louis-Joseph, A.; Bubici, S.; Ferrante, G. Dynamics and Wettability of Oil and Water in Oil Shales. *J. Phys. Chem. C* **2014**, *118*, 23212−23218.
(34) Latour, L. L.; Kleinberg, R. L.; Mitra, P. P.; Sotak, C. H. Pore-Size Distributions and Tortuosity in Heterogeneous Porous Media. *J. Magn. Reson., Ser. A* **1995**, *112*, 83−91.
(35) Gates, W. P.; Bordallo, H. N.; Aldridge, L. P.; Seydel, T.; Jacobsen, H.; Marry, V.; Churchman, G. J. Neutron Time-of-Flight Quantification of Water Desorption Isotherms of Montmorillonite. *J. Phys. Chem. C* **2012**, *116*, 5558−5570.
(36) Cole, D. R.; Ok, S.; Striolo, A.; Phan, A. Hydrocarbon Behavior at Nanoscale Interfaces. *Rev. Mineral. Geochem.* **2013**, *75*, 495−545.
(37) Benetti, A. R.; Jacobsen, J.; Lehnhoff, B.; Momsen, N. C. R.; Okhrimenko, D. V.; Telling, M. T. F.; Kardjilov, N.; Strobl, M.; Seydel, T.; Manke, I.; et al. How Mobile Are Protons in the Structure of Dental Glass Ionomer Cements? *Sci. Rep.* **2015**, *5*, 8972.
(38) Mamontov, E.; Burnham, C. J.; Chen, S.-H.; Moravsky, A. P.; Loong, C.-K.; de Souza, N. R.; Kolesnikov, A. I. Dynamics of Water Confined in Single- and Double- Wall Carbon Nonotubes. *J. Chem. Phys.* **2006**, *124*, 194703.
(39) Fischer, J.; Tsapatsaris, N.; de Paula, E.; Bordallo, H. N. Looking at Hydrogen Motions in Confinement. *Eur. Phys. J.: Spec. Top.* **2014**, *223*, 1831−1847.
(40) Russo, D.; Teixeira, J. Mapping Water Dynamics in Defined Local Environment: From Hindered Rotation to Vibrational Modes. *J. Non-Cryst. Solids* **2015**, *407*, 459−464.
(41) Brunauer, S.; Emmett, P. H.; Teller, E. Adsorption of Gases in Multimolecular Layers. *J. Am. Chem. Soc.* **1938**, *60*, 309−319.
(42) Lippens, B.; De Boer, J. H. Studies on Pore Systems in Catalysts V. The T Method. *J. Catal.* **1965**, *4*, 319−323.
(43) De Boer, J. H.; Lippens, B. C.; Linsen, B. G.; Broekhoff, J. C. P.; Van Den Heuvel, A.; Osinga, T. J. The T-Curve of Multimolecular N_2-Adsorption. *J. Colloid Interface Sci.* **1966**, *21*, 405−414.
(44) Barrett, E. P.; Joyner, L. G.; Halenda, P. P. The Determination of Pore Volume and Area Distributions in Porous Substances. I. Computations from Nitrogen Isotherms. *J. Am. Chem. Soc.* **1951**, *73*, 373−380.
(45) Lovesey, S. W. *Theory of Neutron Scattering from Condensed Matter*; Clarendon Press: Oxford, U.K., 1984.
(46) Cho, M.; Fleming, G. R.; Saito, S.; Ohmine, I.; Stratt, R. M. Instantaneous Normal Mode Analysis of Liquid Water. *J. Chem. Phys.* **1994**, *100*, 6672.
(47) Teixeira, J.; Bellissent-Funel, M.-C.; Chen, S. H.; Dianoux, A. J. Experimental Determination of the Nature of Diffusive Motions of Water Molecules at Low Temperatures. *Phys. Rev. A: At., Mol., Opt. Phys.* **1985**, *31*, 1913−1917.
(48) Krishnamurthy, S.; Bansil, R.; Wiafe-Akenten, J. Low-Frequency Raman Spectrum of Supercooled Water. *J. Chem. Phys.* **1983**, *79*, 5863.
(49) Chen, S. H.; Liao, C.; Sciortino, F.; Gallo, P.; Tartaglia, P. Model for Single-Particle Dynamics in Supercooled Water. *Phys. Rev. E: Stat. Phys., Plasmas, Fluids, Relat. Interdiscip. Top.* **1999**, *59*, 6708−6714.
(50) Bordallo, H. N.; Aldridge, L. P.; Desmedt, A. Water Dynamics in Hardened Ordinary Portland Cement Paste or Concrete: From Quasielastic Neutron Scattering. *J. Phys. Chem. B* **2006**, *110*, 17966−17976.
(51) Dove, M. T.; Hagen, M. E.; Harris, M. J.; Powell, B. M.; Steigenberger, U.; Winkler, B. Anomalous Inelastic Neutron Scattering from Calcite. *J. Phys.: Condens. Matter* **1992**, *4*, 2761−2774.
(52) Singwi, K. S.; Sjölander, A. Diffusive Motions in Water and Cold Neutron Scattering. *Phys. Rev.* **1960**, *119*, 863−871.
(53) Bordallo, H. N.; Herwig, K. W.; Luther, B. M.; Levinger, N. E. Quasi-Elastic Neutron Scattering Study of Dimethyl-Sulfoxide−Water Mixtures: Probing Molecular Mobility in a Nonideal Solution. *J. Chem. Phys.* **2004**, *121*, 12457−12464.
(54) Bauer, B. A.; Ou, S.; Patel, S.; Siva, K. Dynamics and Energetics of Hydrophobically Confined Water. *Phys. Rev. E* **2012**, *85*, 051506.
(55) Cao, G.; Qiao, Y.; Zhou, Q.; Chen, X. Water Infiltration Behaviours in Carbon Nanotubes under Quasi-Static and Dynamic Loading Conditions. *Mol. Simul.* **2008**, *34*, 1267−1274.
(56) Vaitheeswaran, S.; Yin, H.; Rasaiah, J. C.; Hummer, G. Water Clusters in Nonpolar Cavities. *Proc. Natl. Acad. Sci. U. S. A.* **2004**, *101*, 17002−17005.
(57) Johnston, C. T.; Sposito, G.; Erickson, A. C. Vibrational Probe Studies of Water Interactions with Montmorillonite. *Clays Clay Miner.* **1992**, *40*, 722−730.
(58) Xu, W.; Johnston, C. T.; Parker, P.; Agnew, S. F. Infrared Study of Water Sorption on Na-, Li-, Ca-, and Mg-Exchanged (SWy-1 and SAz-1) Montmorillonite. *Clays Clay Miner.* **2000**, *48*, 120−131.
(59) Faÿ-Gomord, O.; Soete, J.; Katika, K.; Galaup, S.; Caline, B.; Descamps, F.; Lasseur, E.; Fabricius, I. L.; Saïag, J.; Swennen, R.; Vandycke, S. New Insight into the Microtexture of Chalks from NMR Analysis. *Mar. Pet. Geol.* **2016**, *75*, 252−271.
(60) Bai, D.; Chen, G.; Zhang, X.; Sum, A. K.; Wang, W. How Properties of Solid Surfaces Modulate the Nucleation of Gas Hydrate. *Sci. Rep.* **2015**, *5*, 12747.
(61) Bultreys, T.; De Boever, W.; Cnudde, V. Imaging and Image-Based Fluid Transport Modeling at the Pore Scale in Geological Materials: A Practical Introduction to the Current State-of-the-Art. *Earth-Sci. Rev.* **2016**, *155*, 93−128.

DOI: 10.1021/acs.jpcc.7b01998
J. Phys. Chem. C 2017, 121, 14088−14095

Paper 4

EPJ manuscript No.
(will be inserted by the editor)

Dynamics of encapsulated Hepatitis B surface Antigen

A combined neutron spectroscopy and thermo-analysis study

Martin K. Rasmussen[1,a], José E. M. Pereira[1], Marcella C. Berg[1,2], Gail N. Iles[3,4], Nicolas R. de Souza[4], Niina H. Jalarvo[5,6], Viviane F. Botosso[7], Osvaldo A. Sant'Anna[8], Marcia C. A. Fantini[9], and Heloisa N. Bordallo[1,2]

[1] Niels Bohr Institute, University of Copenhagen, Copenhagen, Denmark
[2] European Spallation Source (ESS), Lund, Sweden
[3] Department of Physics, Royal Melbourne Institute of Technology, Melbourne, Australia
[4] Australian Nuclear Science and Technology Organisation, Lucas Heights, Australia
[5] Neutron Scattering Division, Oak Ridge National Laboratory, Oak Ridge, TN, USA
[6] Jülich Centre for Neutron Science (JCNS-1), Forschungszentrum Jülich, Jülich, Germany
[7] Virology Laboratory, Butantan Institute, São Paulo, Brazil
[8] Immunochemistry Laboratory, Butantan Institute, São Paulo, Brazil
[9] Institute of Physics, São Paulo University, São Paulo, Brazil

Abstract. As a result of its well-arranged pore architecture mesoporous SBA-15 offers new possibilities for incorporating biological agents. Considering its applicability in oral vaccination, which shows attractive features when compared with parenteral vaccines, SBA-15 is seen as a very promising adjuvant to carry, protect, and deliver entrapped antigens. Recent studies have shown several remarkable features in the immunisation of hepatitis B, a viral disease transmitted mainly through blood or serum transfer. However, the surface antigen of the hepatitis B virus, HBsAg, is too large to fit inside the SBA-15 matrix with mean pore diameter around 10 nm, thus raising the question of how SBA-15 can protect the antigen. In this work, thermal analysis combined with neutron spectroscopy allowed us to shed light on the interactions between HBsAg and SBA-15 as well as on the role these interactions play in the efficiency of this promising oral vaccination method. This information was obtained by verifying how the dynamics of the antigen is modified under confinement in SBA-15 thus also establishing an experimental method for verification of molecular dynamics simulation.

1 Introduction

Vaccination is a powerful and cost-effective form of preventing infectious diseases. However, most vaccines are delivered by injection, which makes mass immunisation

[a] e-mail: martinkr10000@gmail.com

* This research is under the scope of the International Patents WO07/030901, IN 248654, ZA 2008/02277, KR 1089400, MX 297263, HK 1124791, JP 5091863, CN 101287491B, CA 2621373, US 8642258 B2, EP 1942934 B1 and BR PI 0503817-0.

costly and less safe, particularly in resource-poor developing countries. Oral delivery of vaccines has many benefits, and is becoming a preferred means for effective vaccination of many diseases. Unfortunately, often the vaccine-active proteins are unable to produce an immune response when encountering the digestive tract. However there are clear evidences that oral immunisation is a feasible alternative for preventing infections transmitted through non-mucosal routes[1]. Under these lines and as a result of its structural stability and low toxicity, mesoporous silica SBA-15 has been shown to be a promising adjuvant for the oral delivery of hepatitis B[2], a viral disease which attacks the liver and infects about 2 billion people[3].

The pore structure of SBA-15 is bi-modal, having hexagonal ordered 10 nm mesopores, together with disordered macropores larger than 50 nm. This bimodal porosity is therefore expected to protect the vaccine from the gastric acid of the stomach before initiating their release in the intestine. However, the release behaviour will depend on both the physical properties of the carried vaccine (antigen) and the morphology of the carrier SBA-15 (adjuvant). In this work loaded SBA-15 was characterised by using thermogravimetric Fourier Transform Infrared spectroscopy and inelastic neutron scattering to obtain a better understanding of the dynamics of the Hepatitis B surface antigen (HBsAg) encapsulated in SBA-15. Neutron scattering is a well suited method for probing the dynamics of HBsAg inside SBA-15 due to neutrons ability to penetrate and their large interaction with the hydrogen atoms[4].

2 Experimental details

2.1 Sample preparation

SBA-15 with encapsulated HBsAg was prepared by adding 250 mg commercially produced SBA-15 , synthesized as described in[5], to a solution consisting 110 mL 0.45 mg/mL HBsAg solution supplied with phosphate buffered solution (PBS, 10 mM Na_2HPO_4) to obtain a final volume of 500 mL and then dried at 35 °C following the most optimal encapsulation method reported in[6]. Thus obtaining a powder with HBsAg to SBA-15 mass ratio of 1:5. This sample is hereafter labelled SBA-15+HBsAg. A sample containing 500 mL of PBS solution was also prepared to be used as a reference. This sample is labelled SBA-15+PBS.

2.2 Thermogravimetric analysis and Fourier-transform infrared spectroscopy

To determine and characterise the decomposing substances upon heating of the samples, the mass loss and the chemical composition of the released gases from SBA-15+PBS and SBA-15+HBsAg were measured by thermogravimetric analysis (TGA) and Fourier-transform infrared spectroscopy (FTIR) using a Perseus TG 209 F1 Libra (Netzsch, Germany) with an attached ALPHA FTIR spectrometer (Bruker Optics Inc., Germany). About 10 mg of each sample were placed in an aluminum oxide crucible and the temperature was varied from 30 °C to 1050 °C with at heating rate of 10 °C/min under nitrogen gas flow. A new FTIR spectrum of the evolved gases was recorded for every 3 degrees of data collection. An empty crucible were measured as background correction.

2.3 Neutron spectroscopy

Incoherent inelastic neutron scattering (IINS) along with molecular dynamics (MD) simulations offers real possibilities of investigating the dynamics associated with

a molecule biological function(s). Using the large incoherent scattering cross section intrinsic to naturally abundant hydrogen atoms, information on the elastic (E), quasielastic (QENS), and inelastic (IINS) neutron scattering response of a molecule can be obtained. This experimental information when combined to MD simulations offers unique information on the dynamics of biological molecules in confinement, thus deepening our understanding of the relationship between a molecules dynamics and its function.

In this work, quasi elastic neutron scattering (QENS) combined to the elastic fixed window (EFW) method were performed on both samples in order to disentangle the dynamics of the protein confined within the different pore sizes of SBA-15. This approach was used because the degree of confinement will shift the onset of the local protein dynamics to different time-scales and/or temperatures[7]. The EFW method gives information on the evolution of the elastic scattering intensity as a function of temperature, thus allowing us to find the onset of proton mobility by points of inflexion[8]. On the other hand, by analysing the variation of the line width obtained from the analysis of the QENS signal changes in the diffusion coefficient mainly related to the water in the PBS can be readily obtained[9]. This information is crucial in elucidating how the dynamical properties of the salt and antigen are modified when confined in the carrier.

EFW scans were performed during heating from 20 K to 300 K using the EMU high-resolution backscattering spectrometer at the Australian Centre for Neutron Scattering[10]. EMU is a Si (111) crystal backscattering spectrometer characterised by an energy resolution in the order of 1.2 μeV (FWHM) and a wavelength of $\lambda = 6.27$ Å. To probe the confined water dynamics, we performed another set of QENS experiments on the same samples at 310 K, corresponding to body temperature using the backscattering spectrometer BASIS with wavelength centered at $\lambda = 6.4$ Å and an elastic energy resolution of 3.5 μeV (FWHM)[11]. This corresponds to a time scale in the nanosecond (ns) range. For both experiments the sample was placed in annular cylindrical sample holders.

3 Results and discussion

Comparing the TGA curves presented in Fig. 1(a), no observable mass loss was detected for pure SBA-15, indicating that the percentage of polymeric template left in the structure after washing was negligible[12,13]. On the other hand, we observe a mass loss of $\sim$ 8 % for SBA-15+HBsAg starting at 250 °C, which is not present for the SBA-15+PBS sample. The peaks observed in the FTIR signal obtained from the gases released at 300 °C can be assigned to stretching of C-H, C-O and C=O bonds, Fig. 1.(b). Thus, considering that encapsulated HBsAg is a protein consisting of more than 389 amino acids, we can attribute this mass loss to initial stages of protein degradation[14]. The mass remain constant between 500 °C and 800 °C, while on further heating a second mass loss, corresponding to $\sim$ 25 % and $\sim$ 20 % for SBA-15+HBsAg and SBA-15+PBS, respectively, starts at 800 °C. We attribute these to degradation of the strongly hydrogen binding to the surface silanol groups formed during the incorporation of PBS salt[13]. Furthermore, from the FTIR spectrums obtained at 880 °C, Fig. 1.(a), we also observe a weak C-O signal for SBA-15+HBsAg, indicating further degradation of strongly bound antigen.
The combined TGA and FTIR results seem to indicate that the surface antigen HBsAg is confined in two different environments. The majority, which degrades at 300 °C, is present in the larger macropores of SBA-15 and a smaller amount is most likely attached to the entrance of mesopores that starts degrading at 800 °C.

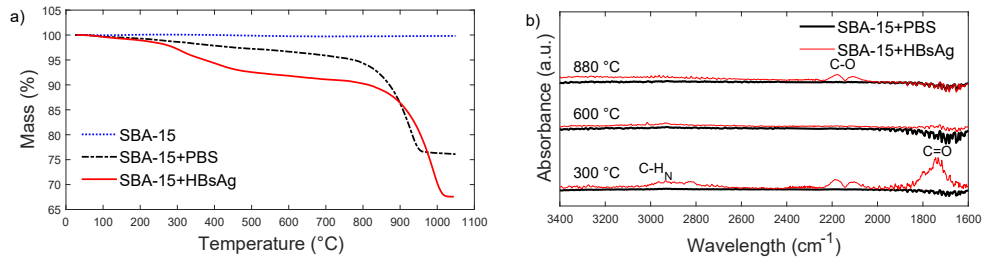

Fig. 1. Comparison of TGA curves (a) and FTIR spectrums at temperatures of interest (b) for SBA-15+PBS containing only PBS salt and SBA-15+HBsAg with encapsulated antigen. Organic material is observed to be released at both 300 °C and 880 °C from SBA-15+HBsAg indicating two different configurations of HBsAg encapsulation. No mass loss was detected for pure SBA-15.

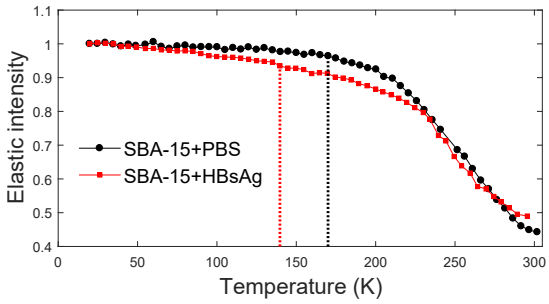

Fig. 2. EFW scans during heating obtained using the backscattering spectrometer EMU for SBA-15+PBS and SBA-15+HBsAg. The inflexion points, indicating the activation of diffusive motions, are marked by dashed lines.

Now we turn to the analysis of the neutron spectroscopy results. By comparing the EFW scans of the two samples in Fig. 2, we observe a faster decrease of the elastic scattering response for SBA-15+HBsAg. Furthermore, the lower temperature of the inflexion point (120 K, marked with a red dashed line), when compared to that for SBA-15+PBS (160 K, marked with a black dashed line) indicates that the presence of the antigen facilitates the activation of hydrogen dynamics as a result of changes in the hydrogen bond network caused by the HBsAg[15]. The second inflection point, around 240 K can be assigned to bulk water confined in pores of tenths of nm[16]. The slightly higher value of immobile hydrogen observed for SBA-15+HBsAg indicates stronger confinement for this sample in the observable time window of EMU.
By focusing on the analysis of the quasi-elastic (QE) region of the inelastic incoherent neutron scattering spectrum obtained on BASIS, we accessed unique information on the dynamical process occurring on the two samples. To this end, we have used the simplest analytical model to describe the hydrogen mobility assuming decoupled translational and rotational motions. Details for the data analysis approach can be found in[17]. Under these lines, all samples were fitted to a delta function, one Lorentzian and a background. For all samples the background was restricted based on the signal recorded at 20 K signal, however the slope of the background was free to vary.
By plotting the half-width at half-maximum (HWHM) as a function of Q^2, Fig. 3, one may check that Fick's law applies if a straight line is obtained. The slope gives directly the self- diffusion coefficient. In the present case, while a linear variation of

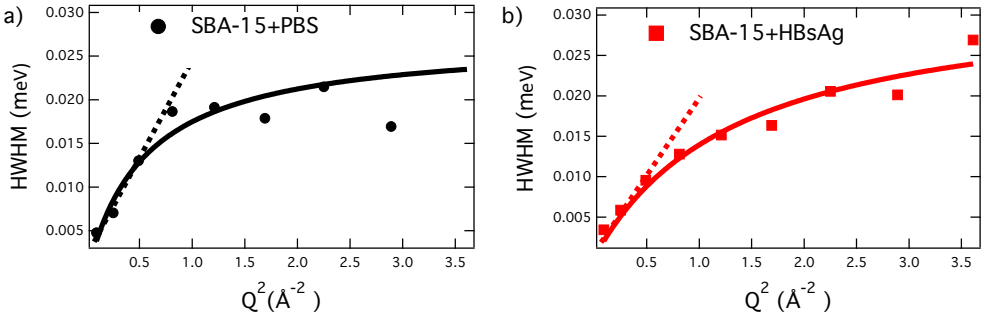

Fig. 3. Evolution of the half-width at half maximum of the quasi-elastic line calculated as a function of Q^2 modelled using the Singwi-Sjölander model from the data obtained using the backscattering spectrometer BASIS for SBA-15+PBS and SBA-15+HBsAg. Dotted lines depict the straight line dependence expected for Fick's diffusion. The errorbars are within the size of the markers.

Table 1. Diffusion coefficient (D_t) and residence time (τ_0) obtained using the Singwi-Sjölander model for the confined water in SBA-15+PBS and SBA-15+HBsAg using an observation time of ns.

Sample	D_t ($10^{-9}m^2/s$)	τ_0 (ps)
SBA-15+PBS	0.8 ± 0.3	24 ± 3
SBA-15+HBsAg	0.37 ± 0.06	20 ± 2

the broadening is found at small Q values, the width deviates from a straight line at larger Q values. This indicates that the continuous diffusion model is no more valid at small distances and that the details of the elementary diffusive steps have to be taken into account. Therefore, the interpretation of the QENS spectra at larger Q values requires a model which contains as parameters the characteristic lengths and times of the mobility steps. Considering the progressive convergence to an asymptotic value, the data were analysed using the Singwi-Sjöander model[18]. The results are given on Table 1. It is well known that under confinement water mobility will shift to longer relaxation times with respect to the bulk water processes (D_t=2.3 $10^{-9}m^2/s$). Thus our results indicate that while the diffusion of the water in the PBS solution is slowed down by a factor close to 3, when the antigen is introduced the diffusion coefficient is slower by a factor 6. The latter indicates that in the ns time scale indeed PBS+HBsAg are immobilised (or protected) by the inner structure of the SBA-15.

4 Conclusion

Molecular dynamics simulations would be a powerful tool to understand and predict the release mechanics of HBsAg from SBA-15 both under relevant biological environments and for various loading degrees of vaccine in the porous silica. Such simulation methods would also be very useful for predicting the behaviour of antigens used in other types of vaccines, with different physical properties including the antigens small enough to enter the 10 nm mesopores. In order to develop such models, however, a variant of state of the art experimental methods are required to verify the simulated dynamics. In this work we have presented results obtained using thermal analysis and incoherent inelastic neutron scattering that reveal properties of the antigen HBsAg encapsulated in the mesoporous silica SBA-15. Through analysis of the neutron data

we were able to probe the dynamics of the hydrogen atoms from the confined HBsAg. In the future we expect that comparison between experimental IINS data and molecular dynamics simulation can be used improving vaccine-active proteins encapsulation in SBA-15.

MRK, JEMP, MCB and HNB neutron research has benefited from the support given by Danscatt funded by Danish Agency for Science, Technology and Innovation. JEMP research is supported through the Brazilian Science Without Borders (Process number 207740/2014-3) program. HNB acknowledges support from the CoNext project. MCAF and OASA are researchers of CNPq, Brazil. This research used resources from the Australian Centre for Neutron Scattering, Australian Nuclear Science and Technology Organisation and from the Spallation Neutron Source, a DOE Office of Science User Facility operated by the Oak Ridge National Laboratory. The thermal analysis apparatus was financed through Carlsbergfond grants ref: 2013-01-0589 and CF14-0230. We would like to thank Dr. Elisabeth C.N.Tenrio and Denise Cristina Andre de Oliveira from the Hepatitis Laboratory of Butantan Institute for preparing the antigen used in this study.

References

1. L. Wang and Ross L Coppel, Expert Rev Vaccines **7**, (2008) 729-738.
2. K. Scaramuzzi, G. D. Tanaka, F. Mariano Neto, P.R.A.F. Garcia, J.J.M. Gabrili, D.C.A. Oliveira, D.V. Tambourgi, J.S. Mussalem, D. Paixo-Cavalcante, M.T. DAzeredo Orlando, V.F. Botosso, C.L.P. Oliveira, M.C.A. Fantini, O.A. Sant'Anna. Nanomedicine: Nanotechnology, Biology and Medicine, **12**, (2016) 2241-2250.
3. World Health Organization. http://www.who.int/mediacentre/factsheets/fs204/en/.
4. J.H. Lakey. J R Soc Interface. **6**, (2009) S567S573.
5. J.R. Matos, L.P. Mercuri, M. Kruk and M. Jaroniec, Chem. Mater. **13** (2001) 1726-31
6. F. Mariano-Neto, J.R. Matos, L.C. Carvalho, K. Scaramuzzi, O.A. Sant'Anna, C.P. Oliveira and M.C.A. Fantini. Journal of Physics D: Applied Physics **47**, (2014) 425402.
7. J. D. Nickles, S. Perticaroli, H. ONeill, Q. Zhang, G. Ehlers and A.P. Sokolov. Biophys. J. **103**, (2012) 1566-1575.
8. M.C. Berg, J. Jacobsen, N.C.R. Momsen, A.R. Benetti, M.T.F. Telling, T. Seydel and H.N. Bordallo. Eur. Phys. J. Special Topics **225**, (2016) 775779.
9. J. Jacobsen, M.S. Rodrigues, M.T.F. Telling, A.L.Beraldo, S.F. Santos, L.P. Aldridge and H.N. Bordallo. Sci. Rep. **3**, (2013) 2667.
10. N.R. de Souza, A. Klapproth and G.N. Iles. Neutron News **27**, (2016) 20-21.
11. E. Mamontov and K.W. Herwig. Rev. Sci. Instrum. **82** (2011) 85109.
12. L.V. Carvalho, R.C. Ruiz, K. Scaramuzzi, E.B. Marengo, J.R. Matos, D.V. Tambourgi, M.C.A. Fantini, O.A. Sant'Anna. Vaccine **28** (2010) 78297836.
13. M. Kruk, M. Jaroniec,C.H.Ko and R. Ryoo. Chemistry of Materials **12**, (2000) 1961-1968.
14. V. Schmidt, C. Giacomelli and V. Soldi. Polymer Degradation and Stability **87**, (2005) 25e31
15. J.D. Nickels, Chemical Physics 424 (2013) 7-11.
16. T. Takamuku, M. Yamagami, H. Wakita, Y. Masuda and T. Yamaguchi, J. Phys. Chem. B **101**, (1997) 57305739.
17. R.E. Lechner, J. Fitter, T. Gutberlet and J. Katsaras. Springer-Verlag Berlin Heidelberg, Germany, (2006) 355-392.
18. K. S. Singwi and A. Sjölander , Phys. Rev. **119**, (1960) 863871.